CHALMERS

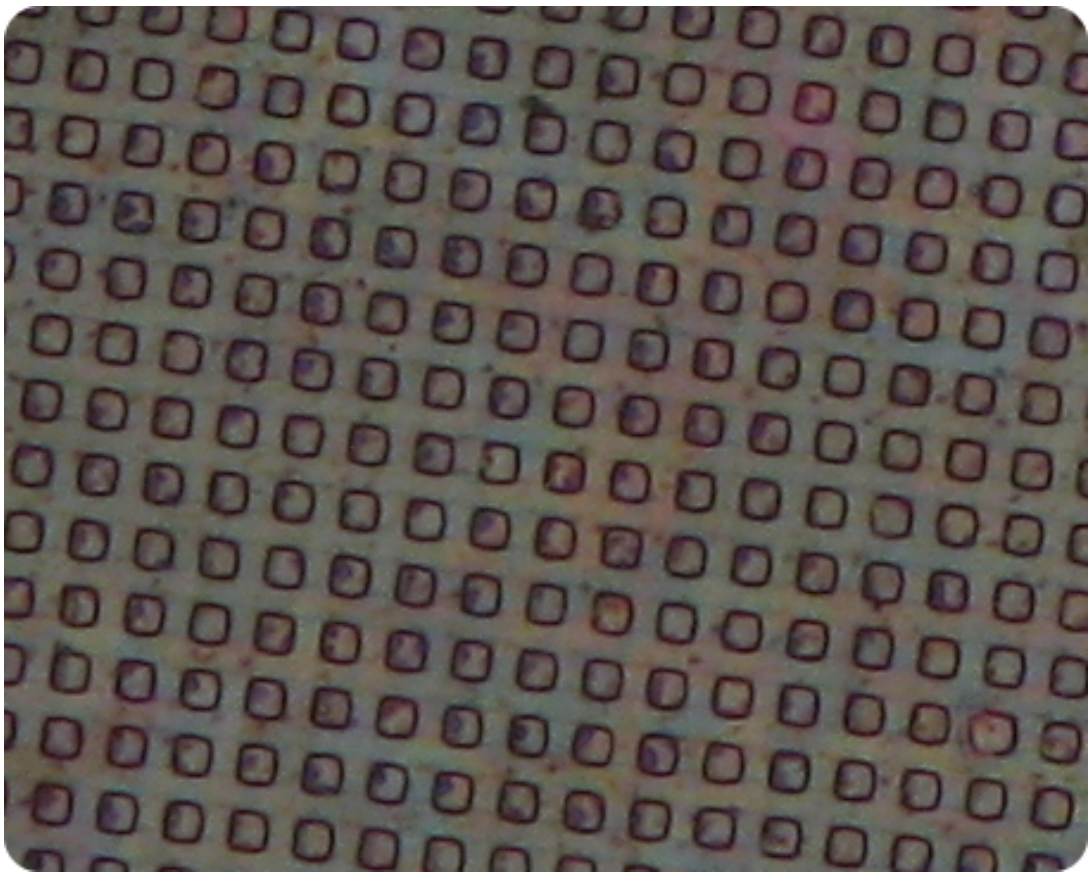

Nanostructured interfaces in thin hybrid and flexible solar cells

Master's Thesis within the Master's programme Sustainable Energy Systems

Nicolas Boulanger

Department of Energy and Environment
Department of Applied Physics
CHALMERS UNIVERSITY OF TECHNOLOGY
Göteborg, Sweden 2011

MASTER'S THESIS

Nanostructured interfaces in thin hybrid and flexible solar cells

Master's Thesis within the *Master's programme Sustainable Energy Systems*

NICOLAS BOULANGER

SUPERVISORS
DAVID BARBERO (Principal supervisor)
MATTIAS ENG

EXAMINER
MICHAEL ZÄCH

Department of Energy and Environment
Department of Applied Physics
CHALMERS UNIVERSITY OF TECHNOLOGY

Göteborg, Sweden 2011

Nanostructured interfaces in thin hybrid and flexible solar cells

Master's Thesis within the *Master's programme Sustainable Energy Systems*
Nicolas Boulanger

Department of Energy and Environment
Department of Applied Physics
Chalmers University of Technology
SE-412 96 Göteborg
Sweden
Telephone: + 46 (0)31-772 1000

Cover:
Pillars thermally imprinted on a P3HT/SWNTs thin film

Chalmers Reproservice
Göteborg, Sweden 2011

Nanostructured interfaces in thin hybrid and flexible solar cells
Master's Thesis in the *Master's programme Sustainable Energy Systems*
Nicolas Boulanger
Department of Energy and Environment
Department of Applied Physics
Chalmers University of Technology

ABSTRACT
Global final energy consumption was around 8,428 Mtoe in 2008 and is expected to grow by 36 % between 2008 and 2035 according to the International Energy Agency. At the same time, global warming has become an issue and objectives have been set to reduce the emissions of greenhouse gases (GHG). This leads to the need to develop low GHG emitting energy sources. This situation is ideal for the development of solar cells, which produce electricity from sunlight without greenhouse gas emissions. Several technologies are being developed such as Si based solar cells, dye sensitized solar cells and thin hybrid and organic solar cells.
The latter are relatively cheap and can easily be mass produced. However, their efficiency is low compared to silicon based cells and research is still in progress to solve that issue. One promising way of improving the efficiency of organic solar cells is to blend carbon nanotubes (CNTs) as electron acceptors into the active layer of the cell. Those CNTs could serve as an electronic pathway towards the cell electrodes. This project aims to find cheap and easy ways of aligning the CNTs inside the active layer of the cell. This alignment can be useful for increasing the efficiency of the CNTs as electron pathways. Methods tried to align the CNTs are nanoimprint lithography (NIL), electric field assisted self-assembly and substrate rubbing. The samples are then characterized by using optical microscopy, atomic force microscopy, scanning electron microscopy, Raman spectroscopy, X-ray photoelectron spectroscopy and electrical conductivity measurements.
This thesis shows that thermal NIL as well as room temperature solvent assisted NIL can be effectively used to align CNTs in a polymer film. This is particularly visible in the Raman spectroscopy measurements. More experiments and the use of a polarised Raman spectroscope are required in order to conclude on the effectiveness of using substrate rubbing in order to align the CNTs.

Keywords: carbon nanotubes, P3HT, solar cell, nanoimprint lithography, electric field assisted self-assembly, substrate rubbing, alignment

Nanostruktuterat gränsnitt i tuna hybrid och flexibla solceller
Examensarbete inom masterprogrammet *Sustainable Energy Systems*
Nicolas Boulanger
Institutionen för Energi och Miljö
Institutionen för Teknisk Fysik
Chalmers tekniska högskola

SAMMANFATTNING

Världens energiförbrukning var 2008 ungefär 8428 Mtoe och förväntas växa med 36% fram till 2035 enligt International Energy Agency. Samtidigt har den global uppvärmningen blivit en viktig fråga, och mål om att minska utsläppen av växthusgaser har fastställts. Detta skapar ett behov av att utveckla energikällor med låga utsläpp av växthusgaser. Denna situation är idealisk för utveckling at solceller, som producerar el från solljus utan utsläpp av växthusgaser. Flera tekniker, som kiselbaserade och färgsensiterade, utvecklas parallellt. Bland dessa tekniker återfinns även hybrid- och organiska solceller.
Dessa celler är relativt billiga och kan lätt massproduceras, men deras verkningsgrad är låg jämfört med Si-baserade celler och forskning pågår fortlöpande för att öka den. Ett lovande sätt att förbättra verkningsgraden hos organiska solceller är att använda kolnanorör som elektronacceptorer i det aktiva lagret i cellen. Nanorören kan där fungera som en elektronisk transportväg till cellens elektroder. Detta projekt syftar till att hitta billiga och enkla sätt att orientera nanorör i det aktiva lagret i cellen i en specifik riktning. Denna inriktning kan vara användbar för att öka nanorörens effektivitet som elektronisk transportväg. De metoder som här har tillämpats för att rikta nanorör är nanolitografi (NIL), elektriskt fält -assisterad self-assembly och substratstrykning. Proverna har sedan analyserats med hjälp av optisk mikroskopi, atomkraftsmikroskopi, svepelektronmikroskopi, ramanspektroskopi och mätning av elektrisk ledningsförmåga.
Denna avhandling visar att termisk NIL såväl som rumstemperatur lösningsmedelsassisterad NIL kan användas för att rikta nanorör i en polymerfilm. Detta visas särskilt av ramanspektroskopi-mätningarna. Ytterligare experiment och användning av till exempel polariserad ramanspektroskopi krävs för att dra slutsatser om effektiviteten av substratstrykning för att rikta nanorör.

Nyckelord: P3HT, solceller, nanolitografi, elektriskt fält -assisterad self-assembly, substratstrykning

Contents

List of Figures

Acknowledgements

This thesis project has taken place in the department of Physics of the University of Umeå, Sweden. I would like to thank my superviser at Umeå, David Barbero, for making this project possible and for his generous assistance all along this work. I would also thank Michael Zäch and Mattias Eng for having kept an eye on me during all this time. Moreover, I would like to specifically thank Madeleine Ramstedt for the help with the XPS measurements, Per Hörstedt for providing the SEM pictures and András Gorzsás and Thomas Wågberg for the help with the Raman spectroscopy measurements.
I would also like to express my gratitude to my group members Ivan Huuva and Jianbao Zhao for their support and help during my work in Umeå. The members of Thomas Wågberg's and Ludwig Edman's groups should not be forgotten, as their company during this time in Umeå was highly enjoyed.
Tuong-Van "Tipi" Nguyen, Hélène "Tippu Tip" Fournière, Daniel Ek Weis, Jean-Édouard "Lumpy" Desaigues and Fabrice "Obelix" Reding should be remembered as well for their constant support, good humour and insights.
Finally, I would like to praise my family for their constant support and unfading love during my studies, and without whom none of this would have ever been possible...

Notations

Roman upper case letters

AFM	Atomic force microscopy
CCS	Carbon capture and storage
CNT	Carbon nanotube
CVD	Chemical vapor deposition
DMF	Dimethylformamide
EHD	Electrohydrodynamic
ESCA	Electron spectroscopy for chemical analysis
ETFE	Ethylene(tetrafluoroethylene)
GHG	Greenhouse gases
HOMO	Highest occupied molecular orbital
IEA	International Energy Agency
IR	Infrared
LUMO	Lowest unoccupied molecular orbital
Mtoe	Million tonnes of oil equivalent, 1 Mtoe is equivalent to 0.086 TWh electricity
MWNT	Multi-walled carbon nanotube
NIL	Nanoimprint lithography
OPV	Organic photovoltaic
P3HT	Poly(3-hexylthiophene)
P3OT	Poly(3-octylthiophene)
PCBM	[6,6]-phenyl-C_{61}-butyric acid methyl ester
PDMS	Polydimethylsiloxane
PMMA	Poly(methyl methacrylate)
PS	Polystyrene
PTFE	Polytetrafluoroethylene (mostly known under the brand name *Teflon*)
RBM	Radial breathing mode
SEM	Scanning electron microscopy
SWNT	Single-walled carbon nanotube
UV	Ultraviolet
XPS	X-ray photoelectron spectroscopy

Roman lower case letters

at %	Percent atoms
eV	Electron volt, about $1.602\ 10^{-19}$ J
gcd	Greatest common divisor

mmHg	Millimeter of mercury, around 133.322 Pa
o-DCB	Ortho-Dichlorobenzene
rpm	Revolutions per minute
wt %	Percent weight

Chapter 1

Introduction

1.1 The energy challenge

In 2008, the world total final energy consumption was around 8,428 Mtoe, from which 17.2 % is electricity [IEA, 2010a]. This corresponds to a final electricity consumption of 1,450 Mtoe, which is about 16,860 TWh. This energy consumption is expected to increase by around 36% between 2008 and 2035, according to the International Energy Agency (IEA) [IEA, 2010b]. At the same time, climate change is a growing concern and objectives have been set to reduce CO_2 and other greenhouse gases emissions in order to mitigate the effects of climate change [French, 1998]. The fact that the energy demand is expecting to increase and that, meanwhile, greenhouse gas emissions have to be cut down requires several strategies to be developed in order to respond to this challenge.
Three strategies can be considered:

- Development of carbon capture and storage technologies,
- Energy efficiency measures and change of lifestyle,
- Development of low greenhouse gas emitting energy sources

Carbon capture and storage (CCS) is currently under development and several techniques are being studied [Chalmers and Gibbins, 2010; Graus et al., 2011; Celia et al., 2011]. The idea is to separate the CO_2 content from the flue gases of the fuel combustion and to store it, either underground or at sea [Jozef, 2009; Rau, 2011]. The CO_2 extraction can even be done during the combustion of the fuel by using techniques such as chemical looping [Noorman et al., 2011]. The CCS technology possibilities look promising, but several drawbacks can limit its interest, such as the risk of leakage of the CO_2 from its storage place [Patil et al., 2010].
A second strategy to consider is to try to make people aware of the problem and to put incentives on energy efficiency measures and to promote a change of lifestyle in order to reduce the energy demand. This can be achieved by putting in place subsidies or taxes, but whether it will work or not depends on the country in which they are applied [Markandya et al., 2009]. The areas where energy efficiency measures could be taken are broad, with for example renovation of houses or construction of low-energy houses [Mlecnik, 2010; Blengini and Carlo, 2010].

Finally, non or low greenhouse gas emitting energy sources have to be developed. Such energy sources are already in use in the current energy mix, such as wind power, hydro power and nuclear power [Kaldellis and Zafirakis, 2011; Lenzen, 2010; Kessides, 2010]. The latter, however, is highly controversial: waste management, proliferation risks and accident consequences are issues which should not be considered lightly [Ramana, 2009; Tuttle and Becker, 2000]. Solar cells are also a realistic option, with the ability to convert energy from the sun into electricity [Rockett, 2007].

1.2 Thin film organic solar cells

Amongst the numerous solar cells designs, thin film organic solar cells have a great potential [Yianoulis and Giannouli, 2008]. Being polymer based, their fabrication process is already well developed and methods and tools for large scale production are already available [Brabec et al., 2001]. However, the efficiencies of those cells are quite low, with the highest efficiencies recorded being around 5 % [Hoppe and Sariciftci, 2008].
Another issue with polymer solar cells is the ageing process of the polymer. Indeed, the action of the outdoor environment on the solar cell can degrade the polymer composing it, therefore reducing its efficiency [Jørgensen et al., 2008; Gardette et al., 2010]. However, it seems that adding fullerenes into the polymer tends to stabilize the cell performances. Experiments have been conducted and showed that the studied polymer/fullerene mix was stable over a period of at least 10,000 hours, which was the investigated time range of the study [Manceau et al., 2010].
Carbon nanotubes (CNTs) can also be used in polymer solar cells. Indeed, the inclusion of carbon nanotubes into a polymer matrix enables the fabrication of thin films with good electrical conductivity. Then, they also allow electron transfer as well as hole transfer, implying that they can be used either as an electron donor or acceptor [Barnes et al., 2010; Dissanayake and Zhong, 2011]. Depending on the polymer and the CNTs used, the percolation threshold (the minimal concentration of CNTs in polymer allowing electrical conductivity) can be as low as 4 wt% with poly(3-octylthiophene) (P3OT), 0.39 wt% with poly(methyl methacrylate) (PMMA) or 0.75 wt% with poly(3-hexylthiophene) (P3HT) [Kymakis and Amaratunga, 2006; Barnes et al., 2010; Alexandrou et al., 2009].
Moreover, CNTs have unique properties making them advantageous to use in thin film organic solar cells. For a start, they allow ultrafast charge separation at the interface between the nanotubes and the polymer, meaning that the losses in the cell efficiency due to recombination process are reduced drastically [Stranks et al., 2011].
However, some precautions have to be taken with nanotubes integration into solar cells, as their impact on health and environment is still not clear [Dumortier et al., 2006; Helland et al., 2007].

1.3 Working principle

A thin film solar cell consists of a stack of several layers:

- The active layer, in which the charge generation occurs
- A buffer layer aimed at gathering the generated charges

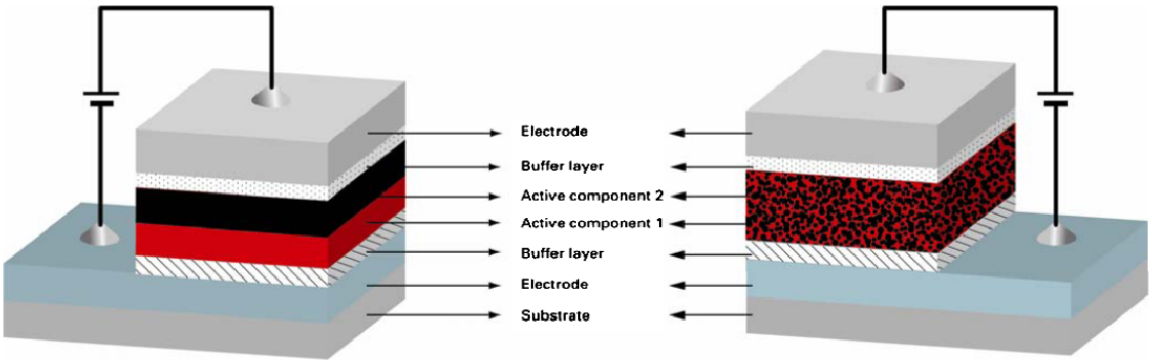

Figure 1.1: Examples of thin film solar cell. *Left picture:* bilayer structure. *Right picture:* bulk-heterojunction structure. [Nicholson and Castro, 2010]

- The electrodes

Depending on the type of solar cell considered, the active layer can have different configurations. Two of these configurations are shown in figure 1.1. As shown on that figure, the active layer is constituted of two materials: one electron donor material and one electron acceptor material.
The working principle of organic solar cells is based on the photovoltaic effect discovered by Bequerel in 1839 and further explained by Einstein in 1905 [Petrova-Koch, 2009; Einstein, 1905]. This effect takes place at the core of the solar cell, in the active layer.
As exposed by Nicholson *et al* [2010], the working principle of a solar cell can be decomposed in five steps:

- The absorption of a photon in the donor material of the cell leading to the generation of an exciton (bound electron - hole pair). Light absoprtion can also happen in the donor material but is less common.
- The diffusion of the exciton within the donor material
- The dissociation of the exciton at the donor/acceptor interface
- The diffusion of the generated charges towards the cell electrodes
- The collection of the charges by the electrodes

1.3.1 Light absorption and exciton generation

The active layer of the cell absorbs only a part of the solar spectrum, depending on the material used. Figure 1.2 shows for example the part of the solar spectrum which is at least partially absorbed by P3HT. Absorption also occurs in the acceptor material, but in organic photovoltaics, the acceptor material consists of fullerenes which have a pretty low light absorption [Nicholson and Castro, 2010].
The absorbed light has an energy content that depends on its wavelength according to the Planck-Einstein equation

$$E = h\nu \tag{1.1}$$

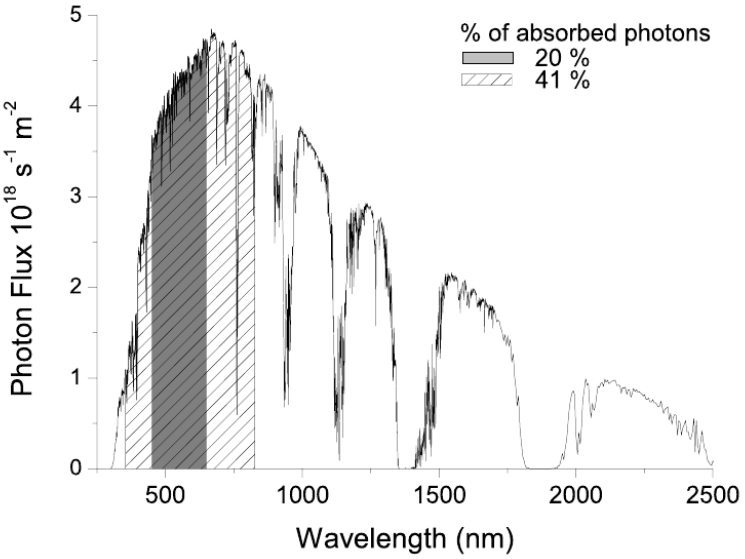

Figure 1.2: AM1.5 solar spectrum, with the absorption band of P3HT [Nicholson and Castro, 2010]

where E is the photon energy content in eV, ν is the light frequency in Hz and h is the Planck's constant and has a value of about $4.135*10^{-15}$ eV.s. If the photon energy is larger than the electronic bandgap of the acceptor material, an electron-hole pair will be created in the material by transfering an electron from the highest occupied molecular orbital (HOMO) to the lowest unoccupied molecular orbital (LUMO) of the donor material. This exciton will then diffuse in the donor material. Another way to improve the light absorption properties of the cell is to use low bandgap polymer, such as P3HT for example with a bandgap of 2.1 eV [Bundgaard and Krebs, 2007; Nicholson and Castro, 2010].

1.3.2 Exciton diffusion

Being an electron-hole pair, an exciton is by nature unstable and chances are that it recombines during its diffusion towards the electron acceptor material. Typical exciton diffusion lengths in organic semiconductors are between 1 and 20 nm. Therefore, the active region of the solar cell which takes part in the usable charges generation is in a volume centered on the donor/acceptor interface and only a few nanometers thick [Nicholson and Castro, 2010]. It implies that, considering exciton diffusion, it is useless for the active layer to be too thick. One way to tackle this issue is to increase the surface area of the donor/acceptor interface by nano-patterning or by making bulk heterojunction, in which the donor and the acceptor materials are interpenetrating, as shown on the right side of figure 1.1.

1.3.3 Exciton dissociation, diffusion and collection

Once at the donor/acceptor interface, the electron will go in the acceptor material, while the hole remains in the donor. In the case where the electron donor material is P3HT and the acceptor is a single-walled carbon nanotube, this separation process can be as short as a couple of picoseconds [Stranks et al., 2011]. After separation, the electron/hole pair remains linked through the donor/acceptor interface and the existing electric field is used to dissociate the pair, leading to the creation of free charges in the active layer [Mihailetchi et al., 2004; Koster et al., 2005]. These free charges then diffuse towards the cell electrodes where they are collected.

1.3.4 Solar cell power conversion efficiency

The solar cell power conversion efficiency is given by the formula

$$\eta_p = \frac{V_M J_M}{P_{inc}} = \frac{V_{OC} J_{SC} FF}{P_{inc}} \tag{1.2}$$

where η_p is the power conversion efficiency, V_{OC} and J_{SC} are respectively the open circuit voltage and the short circuit current defining the maximum power point V_M and J_M, P_{inc} is the incoming light power [Nicholson and Castro, 2010]. V_{OC} and J_{SC} can be determined by the current versus voltage characteristics of the cell. FF is called the fill factor and is related to the charge transport [Schilinsky, 2004].
An other value which is related to the solar cell efficiency is the ratio of produced excitons to the number of photons reaching the cell. This ratio is called the external quantum efficiency (EQE); it depends on the incoming wavelength λ and is given by the formula

$$EQE(\lambda) = \frac{\text{produced excitons}}{\text{incident photons}} = A(\lambda)\,\eta_g(\lambda)\,Q(\mu\tau) \tag{1.3}$$

where $A(\lambda)$ is the absorption coefficient for the wavelength λ, $\eta_g(\lambda)$ the photogeneration efficiency, $Q(\mu\tau)$ the charge collection efficiency and $\mu\tau$ the mobility–lifetime product. Usually, $\eta_g(\lambda)$ is close to 1, and most of the losses occurs during the charge collection (exciton diffusion and dissociation followed by charges diffusion and collection) [Schilinsky et al., 2002].

1.4 Path for improvement

As for now, solar cell efficiencies are low compared to other electricity production techniques. To give an idea, table 1.1 gives the average efficiencies of diverse electricity generation techniques.
As a comparison, table 1.2 gives the best efficiencies achieved for thin film solar cells depending on the technology used.
It is quite clear that improvements have to be done in order to make thin film solar cells competitive with the conventional electricity production techniques. Several ways of improving the cell efficiency are being researched. One way to achieve that is to increase the electrodes surface area, in order to increase the charge collection efficiency ($Q(\mu\tau)$ in equation 1.3) [Kong et al., 2011]. A solution is to pattern the top transparent

	Efficiency	
Production method	**Without CO_2 capture**	**With CO_2 capture**
Coal	45%	35%
Oil	50%	40%
Natural Gas	55%	45%
Biomass	40%	30%
Nuclear	30%	–
Hydropower	50–90%	–

Table 1.1: Electrical efficiencies of typical electricity production techniques [Azar et al., 2006; Marc A, 2001; Barros and Peypoch, 2007]

Type of cell	**Efficiency**
Copper indium gallium diselenide cell	10%
Dye-sensitized cell	8%
Bulk heterojunction cell (P3HT/fullerenes)	8%

Table 1.2: Efficiencies of commercial thin film solar cells depending on the technology used

electrode in such a way that light can enter the cell but is reflected back inside when coming from inside the cell, which helps to increase the light absorption of the cell and therefore its absorption efficiency ($A(\lambda)$ in equation 1.3) [Cho et al., 2011]. This project looks into ways of increasing the efficiency of bulk heterojunction solar cells consisting of P3HT and single-walled nanotubes (SWNTs) by orienting the nanotubes inside the P3HT layer, improving the path for the electrons to travel towards the electrodes. This should improve the $Q(\mu\tau)$ term of equation 1.3.

1.5 Thesis outline

This thesis consists in seven chapters, described as follows:

- Chapter 1 contains a general introduction and exposes briefly the working principle of thin film solar cells.
- Chapter 2 describes the different techniques used in this project to align the nanotubes, as well as introduces a few depiction techniques used.
- Chapter 3 presents the main materials used during the project and some of their properties.
- Chapter 4 introduces the different characterization methods used throughout this project.
- Chapter 5 reports the different experiments conducted during the project.

- Chapter 6 exposes the different measurements conducted and the obtained results.
- Chapter 7 concludes this thesis and gives some recommendations.

Chapter 2

Background and scope

The goal of this project is to align carbon nanotubes in a polymer film. The focus is placed on single-walled carbon nanotubes (SWNTs) and the polymer used here is P3HT. Those materials are commonly used in thin hybrid solar cells and are presented with more details in chapter 3. The nanotubes are supposed here to act as electron acceptors as well as a way to provide a path for those electrons towards the cell electrodes, as described in section 1.3 page 2. The way to align carbon nanotubes which has been studied the most in this project is nanoimprint lithography, but several others ways to align the CNTs have also been briefly tested.

2.1 Nanoimprint lithography

2.1.1 Principles

Nanoimprint lithography (NIL) is a technique in which a mold is pressed against a polymer layer in order to transfer patterns from the mold to this polymer. In order to limit the effort required to deform the polymer, the temperature is usually increased above the glass transition temperature T_g, therefore softening the polymer. An illustration of this process is shown on the left side of figure 2.1. First, the mold is put in contact with the polymer film. Then, the temperature is increased in order to soften the film, making the embossing possible. Pressure is applied to the mold in order to emboss the film. Once the film is embossed, the temperature is decreased under T_g and the mold is finally removed. NIL is commonly achieved by using rigid molds, such as silicon molds usually made using electron beam lithography, a costly and time taking process. But as mentioned by Barbero *et al*, strong force is required to remove the mold, which can lead to its destruction. To avoid that problem, flexible molds made from ethylene(tetrafluoroethylene) (ETFE) have been developed [Barbero et al., 2007]. The NIL process using a flexible fluoromold is shown on the right of figure 2.1. Despite its apparent simplicity, the NIL process is able to make patterns down to about 10 nm. Examples of such patterns done with a flexible ETFE mold are shown in figure 2.2.
In both techniques presented here, heating of the polymer is done in order to soften the film to be embossed. Heating the polymer can lead to several problems: a too high temperature would degrade the polymer. Also, the difference in the thermal expansion coefficients of the mold and of the polymer to be embossed can deform the final imprinted

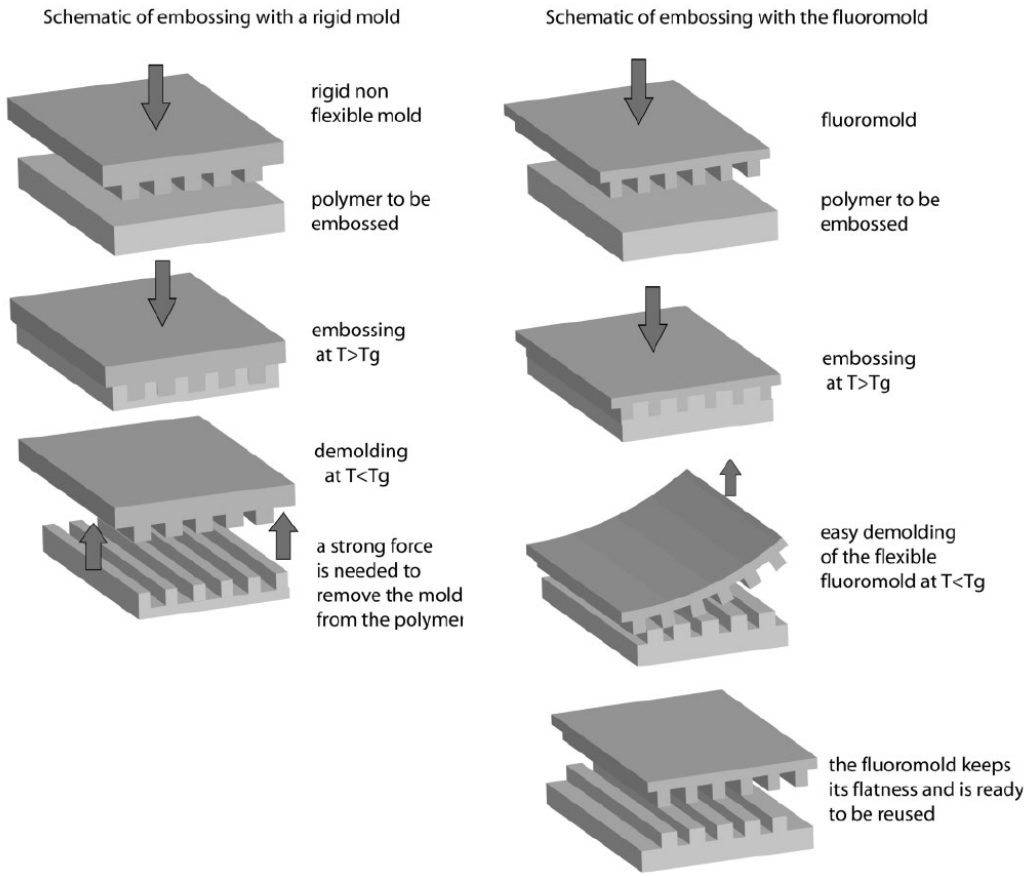

Figure 2.1: *Left picture*: Schematic diagram of embossing with a rigid mold. *Right picture*: Schematic of embossing with a flexible fluoromold. [Barbero et al., 2007]

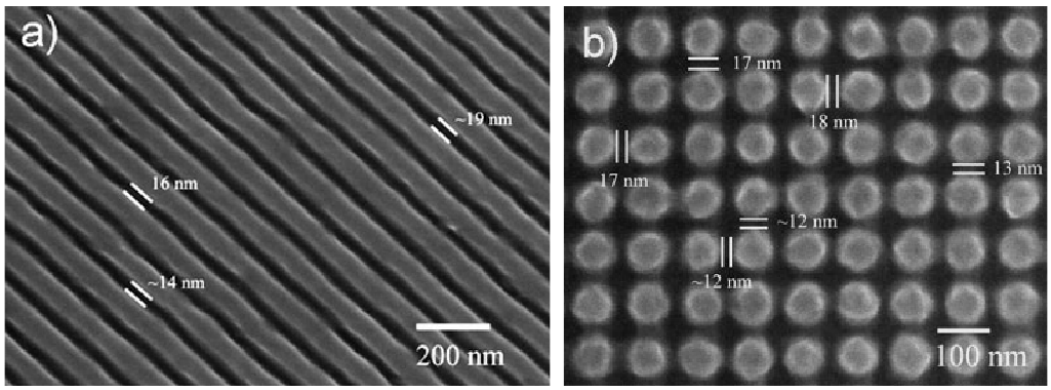

Figure 2.2: SEM images of imprinted structures using a flexible ETFE mold. *a*: Channels imprinted in polystyrene (PS). *b*: 70nm pillars with a period of 90nm imprinted in PS. [Barbero et al., 2007]

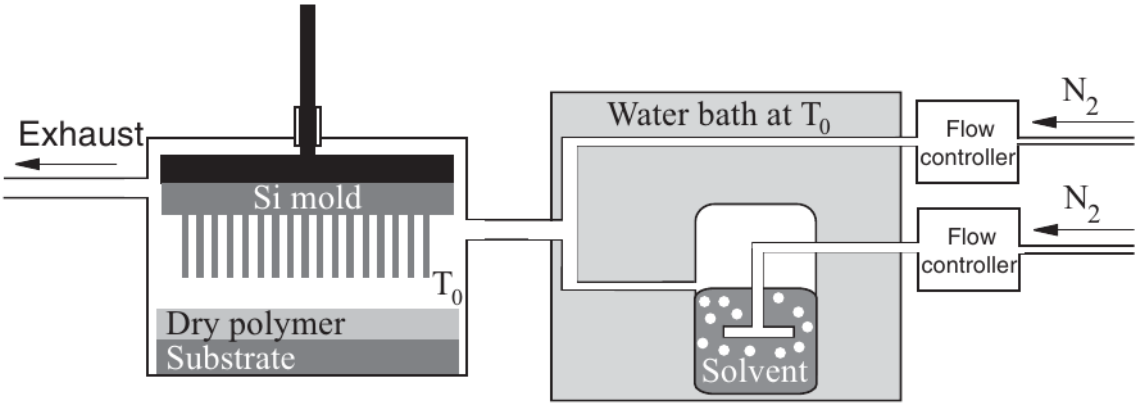

Figure 2.3: Experimental setup used by Voicu *et al* to proceed to solvent assisted imprint lithography. [Voicu et al., 2007]

features [Voicu et al., 2007]. Therefore, a NIL technique which does not involve heating of the polymer has also been developed. This technique uses solvent vapour as a way to swell the polymer at room temperature in order to proceed to the imprint using conventional rigid molds [Voicu et al., 2007]. A representation of the experimental setup used by Voicu *et al* to demonstrate solvent assisted imprint lithography is shown in figure 2.3. With that technique, instead of heating the polymer over T_g in order to emboss it, a flow of solvent vapour is used to soften the polymer. The solvent vapour swells the polymer, and pressure is applied on the mold in order to emboss the polymer film. Then, the solvent vapour is evacuated and a flow of pure N_2 is used to dry the polymer film before removing the mold.

2.1.2 Nanoimprint lithography as a way to align carbon nanotubes

In this project, NIL is used as a way to try to align CNTs inside a polymer matrix. The idea is to take advantage of the polymer flow during the embossing process to drag the CNTs and therefore align them in the embossed patterns. Several studies concerning the polymer flow behaviour during the embossing stage of the NIL process can be found. A schematic representing that stage can be seen in figure 2.4.

The cavity is first filled on the sides. Then, the remainder of the cavity is filled by an upward polymer flow due to the compression of the polymer film by the mold.

The cavity filling process is size dependent. In this project, it is expected to follow the one shown in figure 2.4: the cavity is filled by the polymer which is going in an upward direction. Therefore, nanotubes mixed with the polymer or previously deposited on the substrate can be expected to be dragged along the polymer flow during the imprint. When the polymer dries respectively solidifies again, the nanotubes are expected to be trapped in the imprinted patterns, aligned along the former current lines. This is shown in figure 2.5.

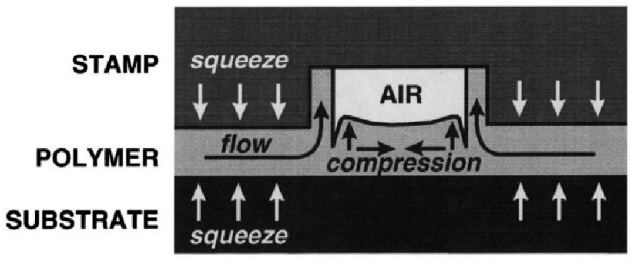

Figure 2.4: Filling of a stamp cavity during the NIL embossing stage. [Heyderman et al., 2000]

Figure 2.5: Expected nanotubes alignement due to NIL. *Grey:* Si substrate, *black:* nanotubes, *red:* polymer, *green:* mold. From left to right: The mold is placed upon the softened film. Then pressure is applied, leading to filling of the cavity as shown in figure 2.4 and displacing the nanotubes. Finally the film is dried, leaving the nanotubes aligned in the polymer film.

2.2 Electrohydrodynamic instabilities

The application of an electric field to a liquefied polymer film can lead to the formation of patterns [Schäffer et al., 2001]. These patterns can be obtained either by self assembly using a smooth electrode and varying the electric field strength or by using a patterned electrode in order to reproduce its patterns [Schäffer et al., 2000]. Schematics of these setups are shown in figure 2.6.
Also, it has been shown that nanotubes can be aligned on a substrate using an electric field [Ural et al., 2002]. The setup presented by Ural *et al* is used to directly grow aligned carbon nanotubes. This setup is presented in figure 2.7.
Therefore, in this project another way to align carbon nanotubes will be studied. A polymer film containing nanotubes will be liquefied and an electric field will be applied. The combined effect of the field on both the polymer and the nanotubes is expected to help align the nanotubes vertically, making them able to act as a path for the electrons in a solar cell.

2.3 Substrate rubbing

It has been shown that polymer chains can be aligned locally by rubbing repeatedly the said polymer on a substrate [Leolukman and Kim, 2005]. This effect can be used to align fibers or crystals in a cheap and easy way. Indeed, liquid crystals have already been successfully aligned on rubbed polymer surfaces [Stöhr et al., 1998]. Therefore, it is

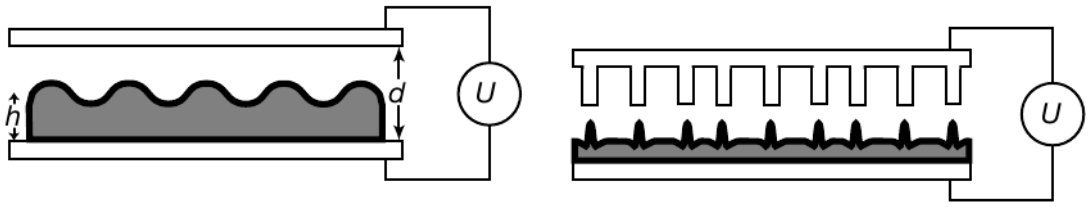

(a) Smooth electrode (b) Patterned electrode

Figure 2.6: Schematics of the electric field experiment setups from Schaeffer *et al.* The electrodes are separated by a distance d, the polymer film has an initial thickness h. The left side picture shows a setup using a smooth electrode whereas the right side picture shows the replication of the pattern of the electrode. [Schäffer et al., 2000]

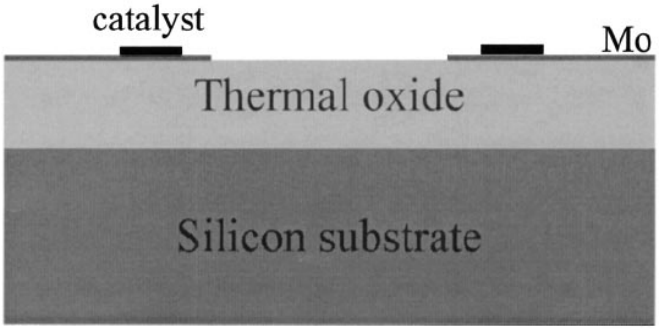

Figure 2.7: Schematics of the setup used by Ural *et al* to grow aligned nanotubes. The nanotubes will grow from the catalyst. The electric field is provided by the two Mo electrodes. [Ural et al., 2002]

interesting to see if nanotubes can be aligned in the same way on a polymer substrate. Depending on the materials used, and more specifically the solvents used, the polymer will have to be chosen carefully. As polytetrafluoroethylene (PTFE) is very resistant to solvent and as its fibers can be aligned by rubbing, it is chosen as the substrate on which the carbon nanotubes are deposited to try that alignment method [Wittmann and Smith, 1991; Defaux et al., 2009; Ranney and Parker, 1997].

2.4 Controlling the nanotubes alignment

The alignment of the nanotubes can be achieved using several methods. Assuming good conditions, AFM can provide an information on the horizontal alignment of the nanotubes, as they are expected to be using the substrate rubbing method. Also, polarized Raman spectroscopy can determine nanotubes alignment, as shown in the paper from Haggenmueller *et al* [Haggenmueller et al., 2000]. An example of the detection of carbon nanotubes alignment by using Raman spectroscopy is shown in figure 2.8. In that figure, it can be seen that the Raman signal from the nanotubes is getting weaker as the angle between the nanotubes' alignment direction and the incident polarization of the measuring laser increases. More details about Raman spectroscopy are given in section 4.2 on page 27.
The alignment of the nanotubes is expected to increase the electrical conductivity of the cell. Therefore, electrical conductivity measurements can also be done to see the evolution of the electrical characteristics of the samples prepared during this project. This kind of measurement can be used for every type of sample realised during the project, depending on the measurement setup.
Finally, the alignment of the nanotubes in the polymer film can be checked using scanning electron microscopy. By freeze cracking the samples, it is possible to look at the slice of the polymer film and therefore to detect the position of the nanotubes and/or the nanotubes aggregates in it.

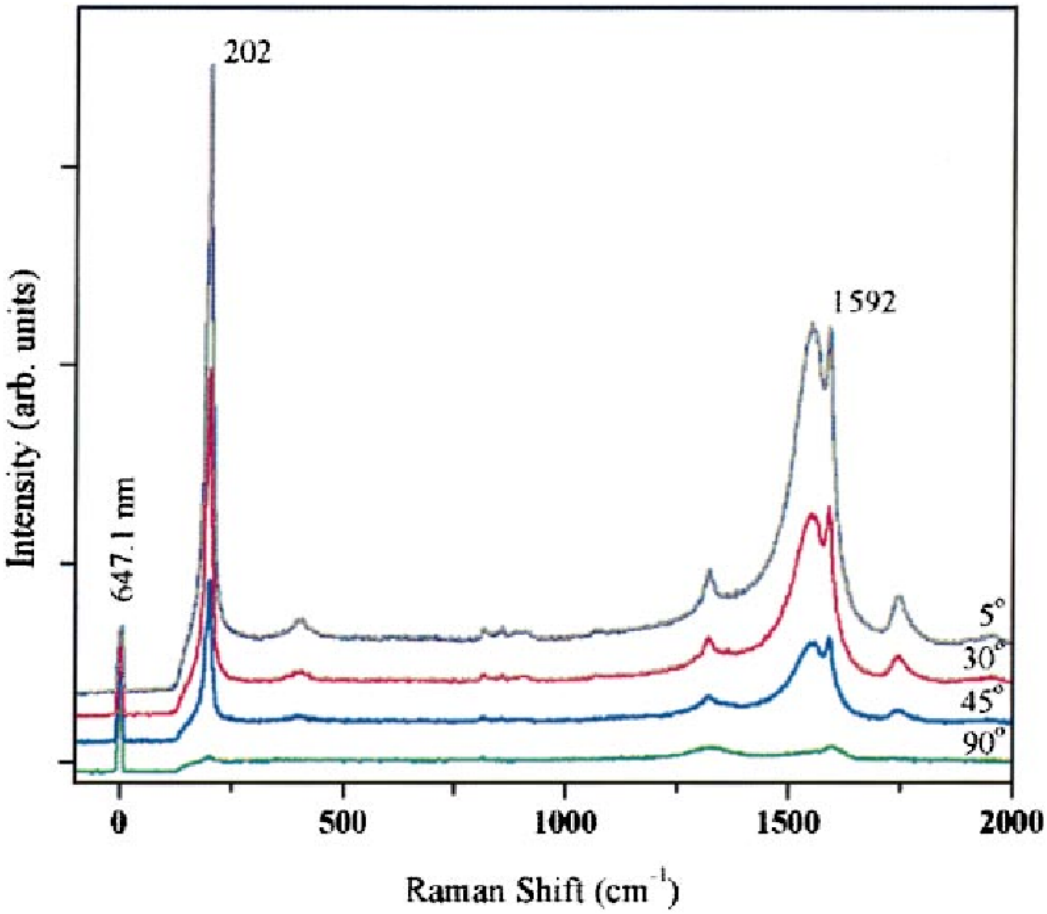

Figure 2.8: Raman spectra of a SWNT-PMMA composite fiber with preferential alignment of the SWNTs. The peaks due to the CNTs are at 202 and 1592 cm^{-1}. The indicated angles correspond to the angle between the fiber and the incident polarization of the Raman excitation laser. [Haggenmueller et al., 2000]

Chapter 3

Materials used

3.1 Carbon nanotubes

3.1.1 Brief history

When speaking about carbon nanotubes, one should make the distinction between multi-walled and single-walled nanotubes, as described in section 3.1.2. The discovery of SWNTs can be established without much doubt in 1993 and has been reported in two papers from Iijima *et al* and Bethune *et al* [Iijima and Ichihashi, 1993; Bethune et al., 1993]. Identifying the discovery of multi-walled carbon nanotubes (MWNTs) is difficult and controversial. The credit for their discovery is usually given to Sumio Iijima who created such carbon configurations in 1991 using an arc-discharge evaporation method [Iijima, 1991]. However, other works prior to this one tend to demonstrate the existence of MWNTs, as stated by Monthioux *et al* [Monthioux and Kuznetsov, 2006].

3.1.2 Characteristics

Carbon nanotubes are made of layers of rolled graphene sheets. Those sheets constitute the different walls of the tubes, as shown on figure 3.1. From now on, the thesis is focusing on single-walled carbon nanotubes only, as those have good electronic charasteristics and are therefore the ones used in the project.

In order to construct the nanotube starting from the graphene sheet, one must choose how the graphene sheet has to be rolled. In order to do that, two atoms are chosen and the sheet is rolled in a way that those two atoms coincide. The vector linking those two atoms is called the chiral vector. This vector, noted $\vec{C_h}$, is defined by the couple of integers (n, m) and the basis vectors $\vec{a_1}$ and $\vec{a_2}$ defined on the lattice of the graphene sheet, as shown in figure 3.2 [Dresselhaus et al., 1995].

Depending on the values of (n, m), the nanotube is either called *zigzag* nanotube ($(n, 0)$ types), *armchair* ((n, n) types) or *chiral* ((n, m) types, with $n < m$). Such tubes are shown in figure 3.3.

By knowing the carbon-carbon distance in the graphene sheet and the value of the couple (n, m), it is possible to determine some characteristics of the nanotubes, such as their diameter. The graphene sheet is constituted of a succession of hexagons. By noting a_{c-c}

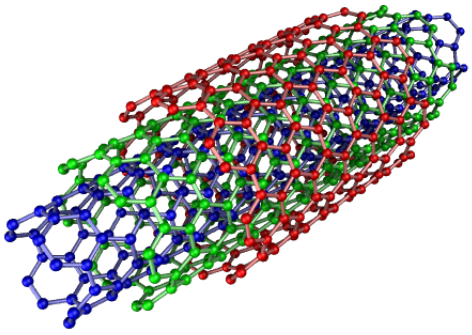

Figure 3.1: Multi-walled carbon nanotube constituted of three graphene layers

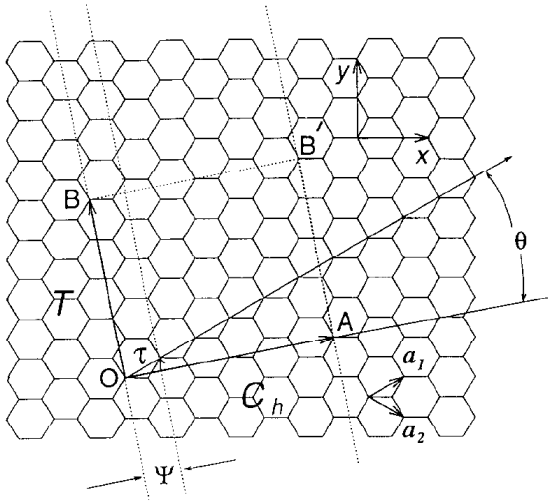

Figure 3.2: The graphene sheet is shown with the chiral vector $\vec{C_h} = n\vec{a_1} + m\vec{a_2} = \vec{OA}$. $\vec{OB}$ is the lattice vector and is perpendicular to $\vec{OA}$. θ is the angle between $\vec{C_h}$ and the zigzag axis. This figure corresponds to $(n, m) = (4, 2)$. [Dresselhaus et al., 1995]

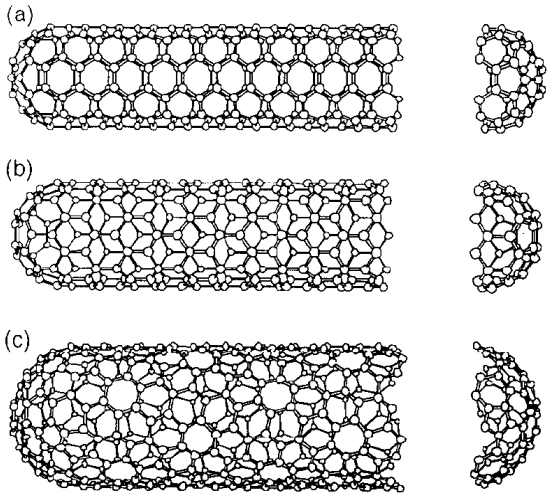

Figure 3.3: Single-walled carbon nanotubes of different chiralities. a) armchair, b) zigzag, c) chiral. [Dresselhaus et al., 1995]

the carbon-carbon distance, the length a of the unit vectors $\vec{a_1}$ and $\vec{a_2}$ is:

$$a = \sqrt{3}a_{c-c} \tag{3.1}$$

By definition, the length of the chiral vector $\vec{C_h}$ is the circumference L of the nanotube and is:

$$L = ||\vec{C_h}|| = a\sqrt{n^2 + m^2 + nm} \tag{3.2}$$

Therefore, the nanotube diameter d_t is:

$$d_t = \frac{L}{\pi} = \frac{a\sqrt{n^2 + m^2 + nm}}{\pi} \tag{3.3}$$

More than just determining the geometrical characteristics of the nanotube, the (n, m) couple also defines if the nanotube acts as a semiconductor or a metallic one. Indeed, if $n - m$ is a multiple of 3, the nanotube is metallic. Otherwise the nanotube acts as a semiconductor with a bandgap inversely proportional to its diameter [Dresselhaus et al., 1995]. However, other factors such as the curvature of the nanotube and the nanotubes-nanotubes interactions due to aggregation can also influence the electronic properties of the nanotubes and therefore the rule mentioned just earlier can be subject to exceptions [Lu and Chen, 2005]. Different (n, m) configurations and an indication on whether the nanotube is metallic or semiconducting are shown in figure 3.4.

3.1.3 Electronic properties

The electronic characteristics of SWNTs are of crucial importance. Indeed, in this project, they are used as an electron acceptor as well as a pathway towards one of the solar cell electrodes, as described in more details in chapter 2 on page 9.
The influence of the SWNTs in the solar cell is mostly due to their electronic band structure. This energy band structure can be derived from the one coming from graphene.

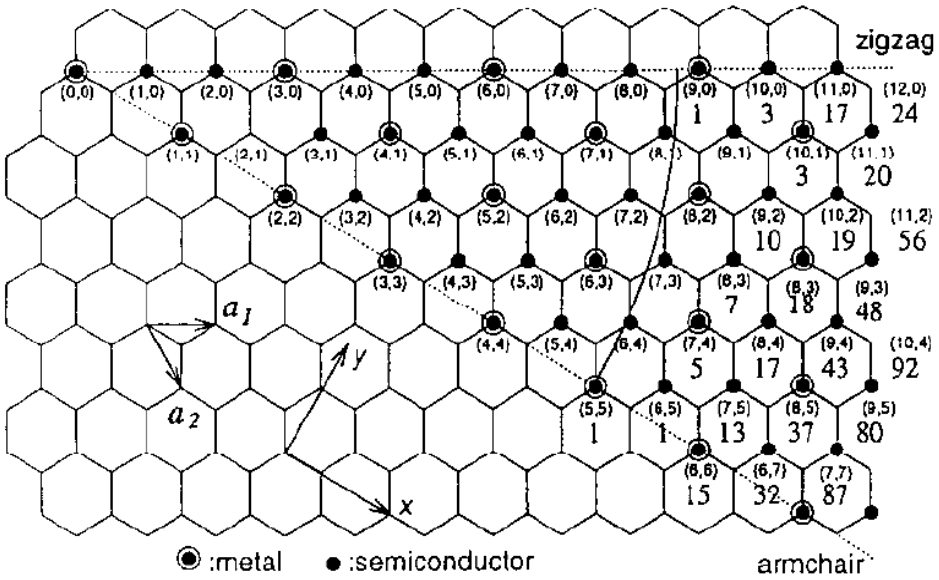

Figure 3.4: Graphene sheet with an indication of the different (n, m) couples and the electronic properties of the corresponding nanotubes [Dresselhaus et al., 1995].

More details about the electronic band structure can be found in the appendix A on page 69 or in the book of Saito *et al* [Saito, 1998]. Depending on the (n, m) value, the SWNT acts either as a metal or as a semiconductor. Indeed, if $n - m$ is a multiple of 3, then the SWNT acts as a metal [Saito, 1998; Dresselhaus et al., 1995]. This effect can be clearly seen on the energy band plots of the SWNTs. As an example, the energy band plot of a $(7, 1)$ SWNT is shown in figure 3.5a, and the energy band plot from a $(6, 5)$ SWNT in figure 3.5b.
It can be clearly seen on the figure 3.5a that the valence and the conduction band of the $(7, 1)$ SWNT intersect, leading to a metallic behaviour. On the other hand, the figure 3.5b shows that a gap exists between the valence and the conduction band of the $(6, 5)$ SWNT, leading it to have the behaviour of a semiconductor. However, the nanotubes produced in reality can have defects that alter their electronic properties [Geng et al., 2008].
The SWNTs used in this project have been bought from Sigma-Aldrich. They are $(6, 5)$ SWNTs and are thus supposed to be semiconducting. Their theoretical electronic band structure diagram is shown in figure 3.5b. The certificate of analysis of the nanotubes is available in appendix C page 75.

3.1.4 Production

CNTs can be produced by several processes. In this thesis, a few of them are briefly presented:

- Arc discharge
- Laser ablation

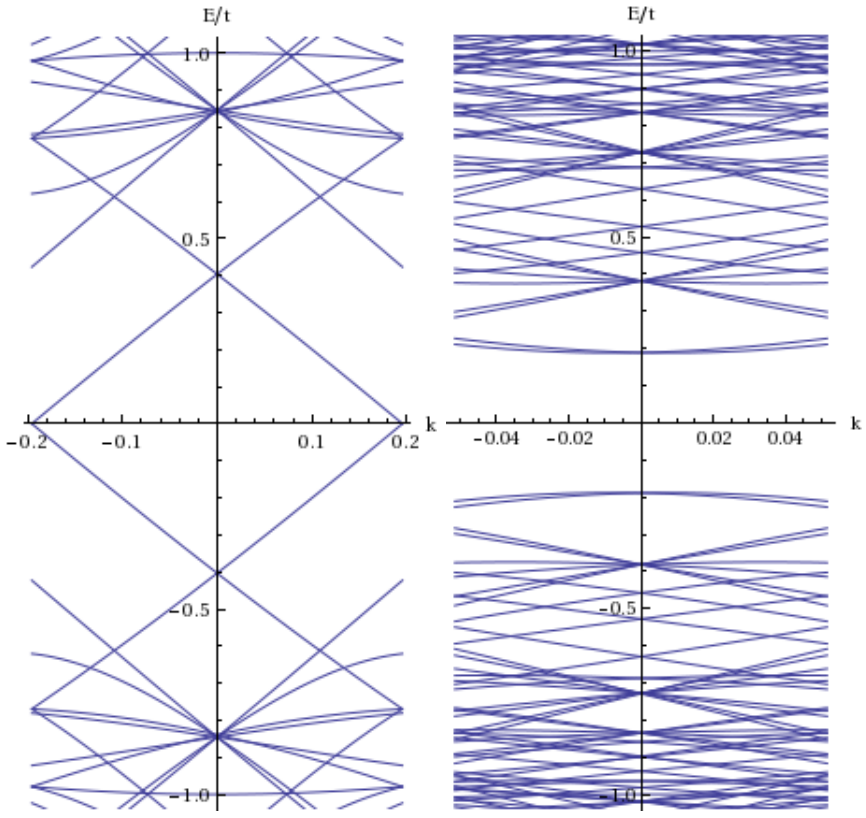

(a) $(7, 1)$ SWNT (b) $(6, 5)$ SWNT

Figure 3.5: Electronic band structure of a $(7, 1)$ and b $(6, 5)$ SWNTs plotted with the program in appendix B on page 73.

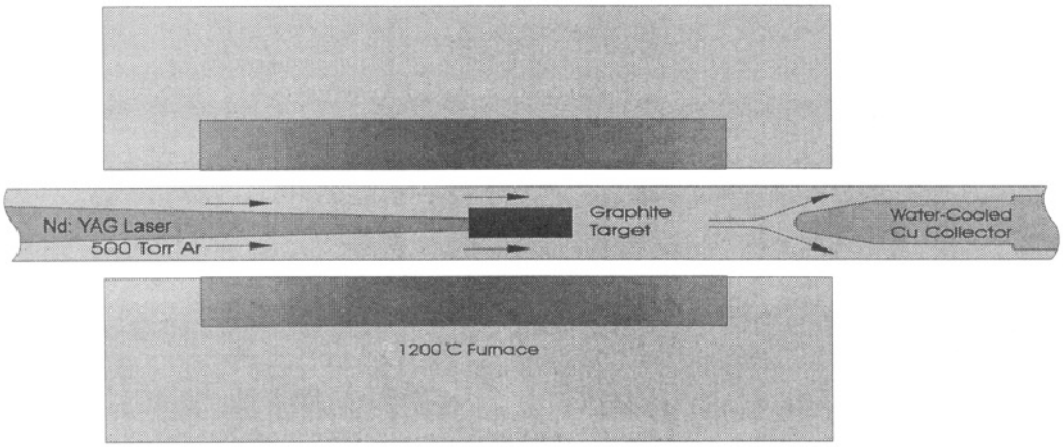

Figure 3.6: Laser ablation setup [Guo et al., 1995a]

- Chemical vapor deposition

Arc discharge

This method uses two graphite electrodes placed close to each other. An electric potential is then applied in order to produce an arc discharge between the two electrodes [Collins and Avouris, 2000]. This method was first developed in the NEC laboratories in 1992 by Ebbesen *et al.* The voltage applied to the electrodes was around 18 V, one graphite rod was 6 cm in diameter, the other 9 cm. They were placed at around 1 mm of each other and the electric current was around 100 A. With these parameters, the nanotube to particle yield is 25 % of the starting material [Ebbesen and Ajayan, 1992]. This method products both SWNTs and MWNTs [Collins and Avouris, 2000].

Laser ablation

This method uses a laser targeted on a graphite rod in a chamber at high temperature. The nanotubes as well as other nanoparticles then condense on a cooler collector. The operation is achieved under an atmosphere consisting of inert gas such as argon for example [Collins and Avouris, 2000]. A representation of the setup is shown in figure 3.6. This method can be used to grow SWNTs: Guo *et al* report yields of 50 % of the graphite target transformed in SWNTs using a mixture of Co and Ni as catalyst [Guo et al., 1995b].

Chemical vapor deposition

This method uses a catalyst on which the CNTs will be growing. The catalyst consists of particles and are heated in the reactor, while a carbon containing gas flows by. The first attempt to produce CNTs using CVD took place in 1993 by José-Yacamán *et al.* The catalyst was iron heated at 700 °C and the carbon containing gas was acetylene. Up to 65 % of the resulting carbon material form corresponded to CNTs [José-Yacamán et al., 1993]. Another CVD process patented as CoMoCAT has been developed in 2005 by Lolli

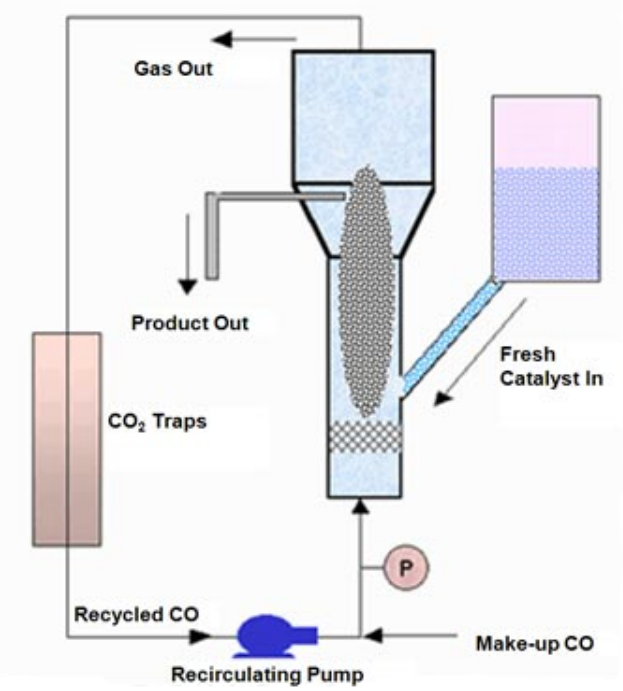

Figure 3.7: The CoMoCAT process *©Southwest Nanotechnologies*

et al. This process uses $CoMo/SiO_2$ as catalyst and CO as carbon containing gas. The reaction takes place in a fluidized bed reactor heated between 700 ℃ and 850 ℃. This method has a high selectivity on the (n,m) values of the nanotubes [Lolli et al., 2006]. This last process is represented in figure 3.7.

3.2 Poly(3-hexylthiophene)

Poly(3-hexylthiophene) (P3HT) is a conjugated polymer and is part of the polythiophene group. Its structure is shown in figure 3.8. Its glass transition temperature is around 67℃ [Aryal et al., 2009].

This polymer is commonly used as an electron donor material in organic solar cells, associated with fullerenes or carbon nanotubes as acceptor materials [Hoppe and Sariciftci, 2008]. Its light absorption spectrum is mostly in the range of 400 to 600 nm, and is shown in figure 3.9.

Also important to the solar cell characteristics is the value of the electronic band gap of the material, which affects the light absorption characteristics of the material. For P3HT, this band gap is around 2.1 eV [Koster et al., 2006]. It should be noted that the polymer chains alignment in the P3HT films also heavily influences the light absorption properties of the material [Bundgaard and Krebs, 2007]. An example of how P3HT crystallizes in films can be seen in the AFM picture (figure 3.10) where P3HT needles can be observed at the surface of a drop-cast film of P3HT on a silicon substrate. The properties of the P3HT used in that project are shown in appendix D page 77.

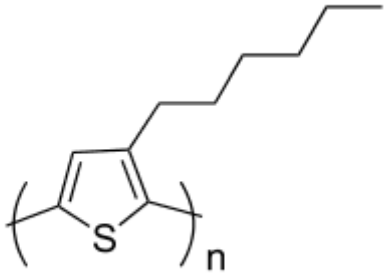

Figure 3.8: P3HT structure

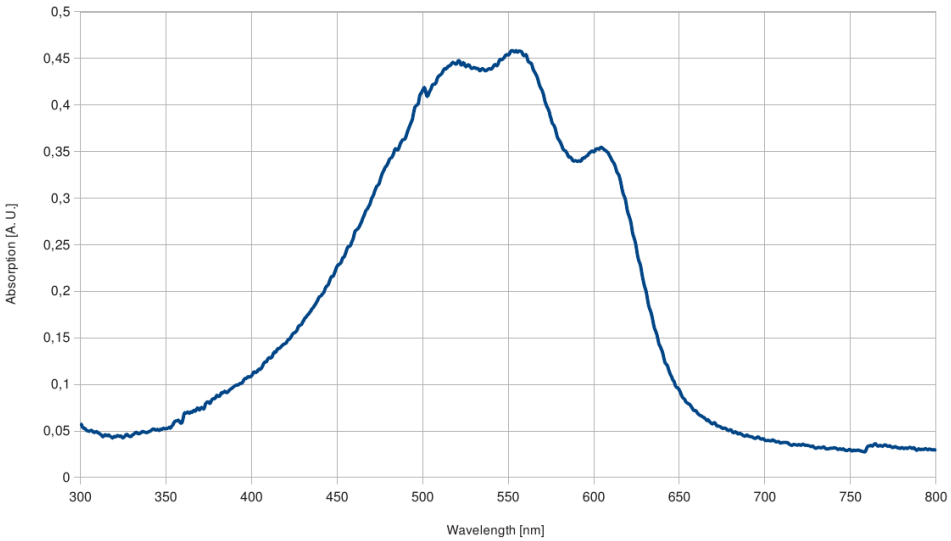

Figure 3.9: Light absorption spectrum of P3HT in solution in o-DCB as measured on a Shimadzu UV-2100 spectrophotometer

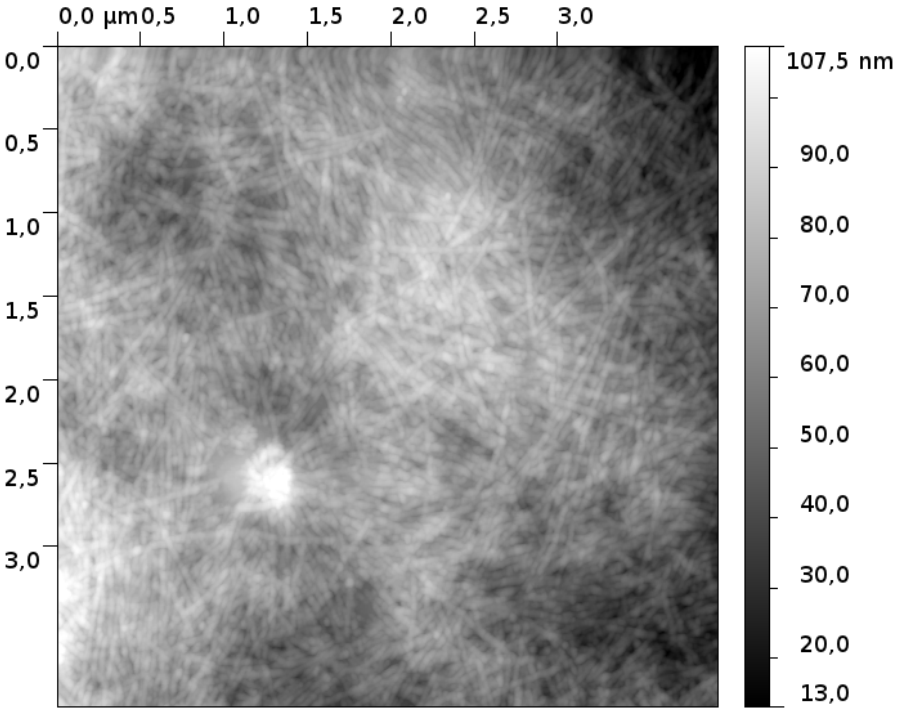

Figure 3.10: AFM height image of a drop-cast P3HT film.

3.3 Polystyrene

Polystyrene is used in this project for being able to do Raman spectroscopy. Its glass transition temperature is around 107℃ [Rieger, 1996]. Its structure is shown on figure 3.11.

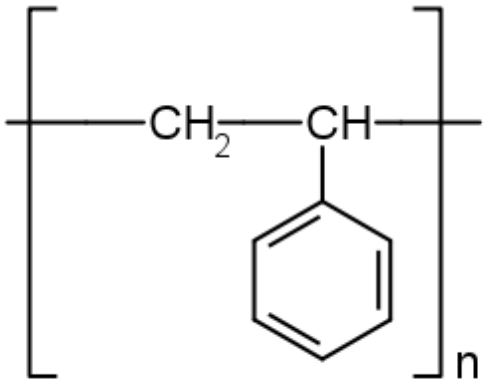

Figure 3.11: Polystyrene structure

Chapter 4

Characterization methods

In this project, several characterization methods have been used to control and test the produced samples. In this chapter, a brief presentation of these techniques is made.

4.1 Spectrophotometry

Spectrophotometry is used in this project for measuring the light absorption properties of the material used. Light is generated from a white light lamp and goes through prisms that disperse light and break it up into its constituent spectral colors. The prism can rotate, allowing the selection of specific wavelengths. The resulting beam either goes directly through an unique sample holder, or is separated into two beams and goes through two sample holders. After passing through the holders, the light hits a sensor which is used to measure the intensity of the light hitting it. By knowing the wavelength of the light hitting the sample as well as its intensity before and after passing through the sample, it is possible to trace the absorption spectrum of the measured sample.
In order to determine the part of the absorption due to a specific constituent in a solution or a thin film, measurements of the solution or the film without that specific constituent and then with it has to be made in order to compare the two spectra. In the case of a single beam spectrophotometer, two measurements are therefore needed whereas in the divided beam spectrophotometer, only one measurement with both the reference sample and the sample to be measured is required.
The spectrophotometer used in this project is a Shimadzu UV-2100, shown in figure 4.1. Its measuring range goes from 200 to 900 nm in wavelength.
The Shimadzu UV-2100 uses a divided light beam to make the measurements, allowing the use of a reference sample at the same time as the measured sample. The two sample holders are shown on figure 4.2. The types of sample measured in this spectrophotometer are solution and polymer thin films. An example of absorption spectrum for a P3HT solution in ortho-dichlorobenzene (o-DCB) is shown in figure 3.9.

4.2 Raman spectrometry

Raman spectrometry is used here to determine the position of the components of the samples made and evaluate their relative concentration. Raman spectrometry has also

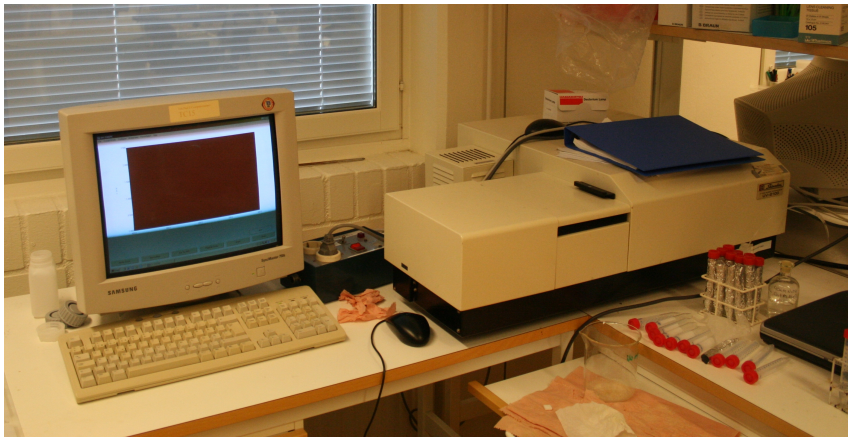

Figure 4.1: The Shimadzu UV-2100 used in this project

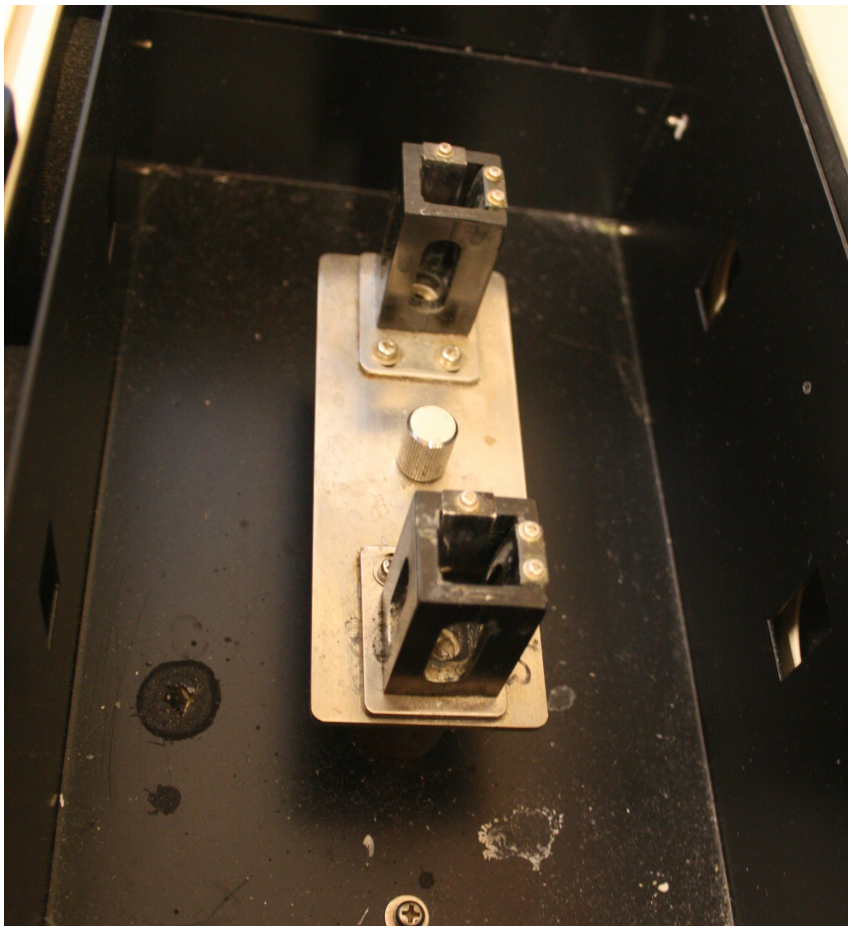

Figure 4.2: Shimadzu UV-2100 sample holders. The holder at the top holds the reference sample and the one at the bottom holds the measured sample.

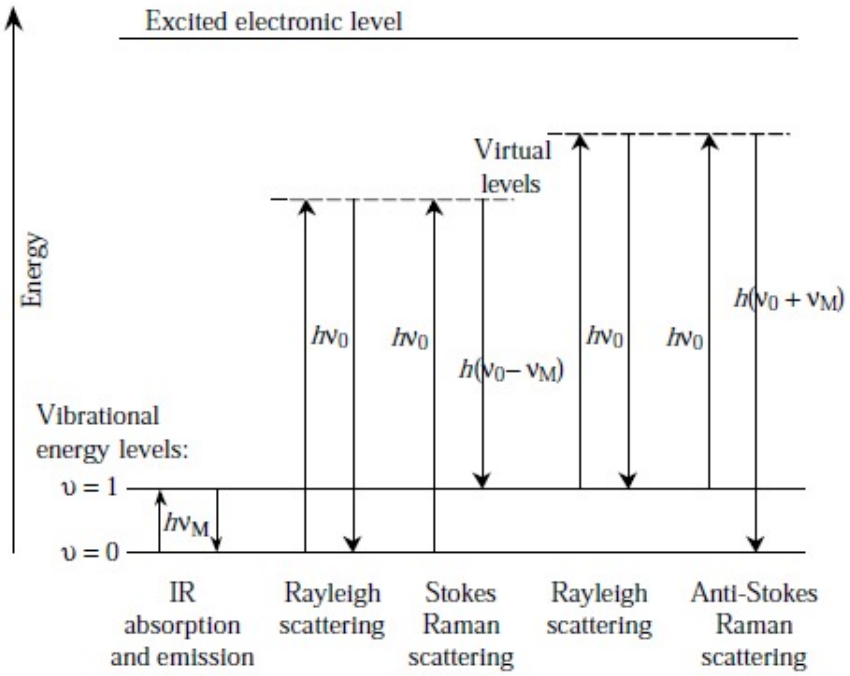

Figure 4.3: Different types of scattering due to light [Keresztury, 2006]

been used to attempt to determine nanotubes alignment in several samples.

4.2.1 Working principle

Raman spectroscopy is based on Raman scattering discovered in 1928 by Raman *et al* [1928]. It is based on inelastic scattering between an incoming light ray and the studied material. Raman spectroscopy exploits two kinds of inelastic scattering: Stokes scattering and anti-Stokes scattering, as shown on figure 4.3 [Keresztury, 2006].
As can be seen in figure 4.3, Stokes and anti-Stokes scattering involve particles hit by a photon of wavelength ν_0 and energy $h\nu_0$ which re-emit a photon with a slightly modified wavelength, depending on the type of scattering happening. Therefore, by comparing the incoming light spectrum with the outgoing spectrum, it is possible to map the different shifts in wavelength due to inelastic scattering of light by the examined sample. These shifts are called Raman shift. In practice, the incoming light comes from a laser, which makes it easier to detect the Raman shifts happening since the laser has a single wavelength.

4.2.2 Equipment

The Raman spectrometer used for this project is a Renishaw InVia Raman spectrometer shown in figure 4.4. It is equipped with three different lasers:

- a tunable 457.9 nm, 488.0 nm, 514.5 nm Ar-ion laser of maximum power 20 mW

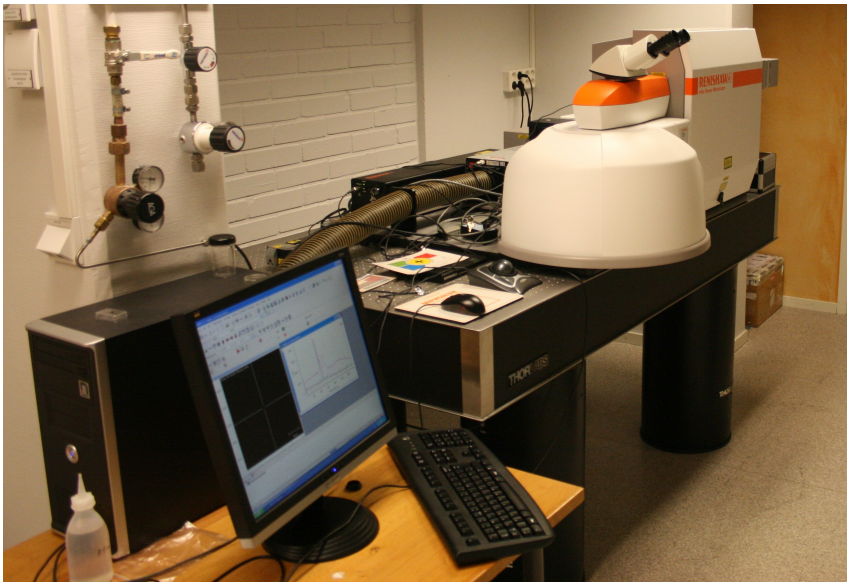

Figure 4.4: Renishaw InVia Raman spectroscope

- a 633 nm HeNe laser of maximum power 20 mW

- a 785 nm infrared diode laser of maximum power 300 mW

4.3 X-ray photoelectron spectroscopy

X-ray photoelectron spectroscopy (XPS), also called electron spectroscopy for chemical analysis (ESCA), is a measurement method which provides the knowledge of the atomic composition of the surface of the examined sample.

XPS involves a monochromatic X-ray beam hitting the area of interest of the examined sample. Due to this irradiation, electrons from the observed surface are ejected at different speeds and collected by a detector. Their kinetic energy is linked to their binding energy and is related to their atom of origin. Their number depends on the concentration of their atom of origin. The atomic composition of the sample can therefore be determined on the observed surface and at a depth up to about 10 nm [Ratner and Castner, 2009]. XPS has been popularised in 1967 by Kai Siegbahn, who won the Nobel prize for this in 1981 [Siegbahn, 1982].

The XPS used in this project is a Kratos Axis Ultra DLD. The X-rays are emitted by a monochromated Al Kα operated at 150W. The measurement area has for dimensions 0.3x0.7 mm^2.

4.4 Microscopy techniques

4.4.1 Optical microscopy

Optical microscopy is used as a quick way to assess the samples, and to check the imprinted patterns on the relevant samples. It is also used to check the cleanliness of the silicon substrate when preparing the first samples of the project.

4.4.2 Atomic force microscopy

Atomic force microscopy (AFM) is used in this project to determine surfaces characteristics and to control imprinted patterns.

Working principle AFM provides topographic information of the examined surface by scanning a probe over it and by measuring its vertical displacement. A schematic of an atomic force microscope is shown in figure 4.5.

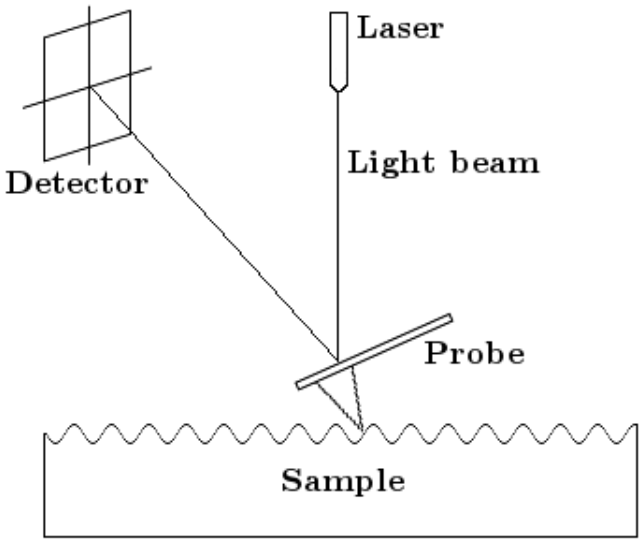

Figure 4.5: Schematic of an atomic force microscope

The scanning of the surface can be achieved using different methods. Only the one used in this project is described: the tapping mode. In this mode, the probe oscillates at a frequency close to its resonance frequency and the oscillation is set at a given amplitude. The probe then approaches the surface until it is tapping it, therefore the mode's name. The probe parcours the surface horizontally, and taps the surface at specified intervals. The vertical position of the probe is captured by a 4 quadrant detector which reads the deflection of a laser beam focused on top of the AFM probe, and which allows the measurement of the probe oscillation amplitude. By monitoring this amplitude and by adjusting the vertical position of the probe in order to keep it constant by using a feedback loop, a topography image of the examined surface can be constructed.

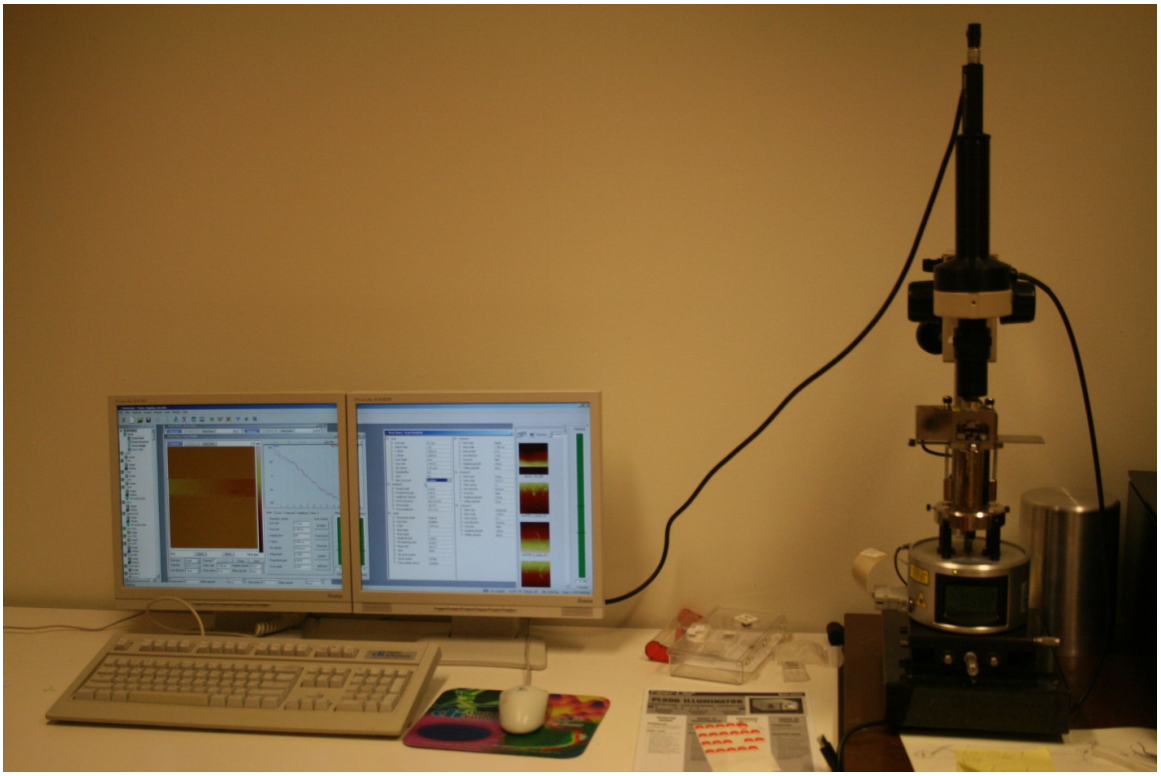

Figure 4.6: Veeco Multimode atomic force microscope

Equipment The atomic force microscope used is a Veeco Multimode and is shown in figure 4.6. The probes used are CT130 and CT300 from Nanoscience Instruments. A CT130 is shown in figure 4.7. The black dot at the end of the cantilever in figure 4.7 is the sharp probe which actually scans the surface of the examined sample.

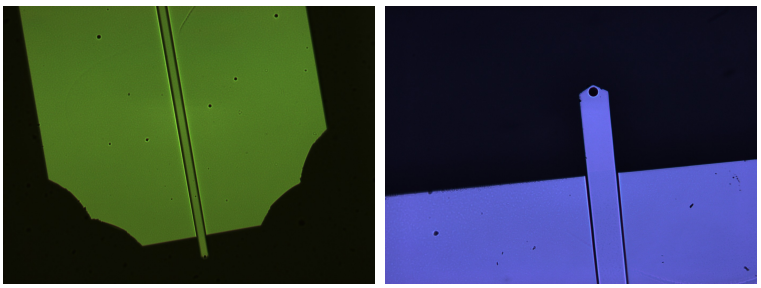

(a) Cantilever (b) Cantilever and probe

Figure 4.7: CT130 probe

4.4.3 Scanning electron microscopy

Scanning electron microscopy (SEM) has been used in this project to examine the cross section of pillars obtained in nanoimprinted samples. Attempts have been made to ob-

serve nanotube aggregates and therefore to be able to visually confirm their alignment. The scanning electron microscope used in this project is a Cambridge Stereoscan 360 iXP.

Working principle The first scanning electron microscope has been built in 1935 by Knoll and had a resolution limit of about 100 μm [Bogner et al., 2007]. In order to analyze the sample, an electron beam is generated and focused on the examined area of the sample. When reaching the observed spot, the electrons from the beam interact with atoms of the sample and lose energy by scattering. Several phenomenons take place:

- Electrons from the conduction band of the sample are ejected: they are called *secondary electrons*.
- Electrons from the electron beam can be reflected outside the sample: they are the *back-scattered electrons*.
- An atom from the sample can have one of its inner-shell electrons getting ejected, leading to the excitation of the atom. The deexcitation of the atom can lead to the emission of an *Auger electron* or of an *X ray* photon.

In this project, only secondary and back-scattered electrons have been detected. Secondary electrons provide information about the topography of the sample whereas back-scattered electrons hint about the composition of the sample, specifically about contrast in the material density: light elements will appear darker than heavier elements.

4.5 Electrical conductivity measurement

Electrical conductivity measurements have been conducted in order to indirectly detect alignment of the nanotubes in the polymer substrate of several samples. Indeed, the nanotubes alignment is expected to increase the conductivity of the samples, as they are assumed to provide a path for the electrons into the polymer.
For this measurement, the samples are placed between two brass electrodes and a varying voltage is applied. The resulting current is measured in order to plot a current/voltage curve for the examined sample. The equipment used is an AUTOLAB PGSTAT 302 and the setup with the two electrodes is shown in figure 4.8.
However, the top electrode is slightly larger than the sample, making impossible to measure the conductivity of the central area of the sample. This might be problematic as the sides of the sample are not perfectly smooth. Also, silver paste is used between the silicon substrate and the bottom electrode in order to improve the conductivity. If the paste sticks to the sides of the sample, short circuit might happen during the measurements. Finally, the surface of the sample might not be perfectly smooth, and the same goes for the top electrode. This might pose problems for having good contact between the top electrode and the surface of the sample. Therefore, soft electrodes have been made from PDMS stamps. The PDMS stamps have been cut and a first titanium layer of 1 nm has been deposited as a sticking layer. Then, 60 nm of gold have been deposited in order to assure electrical conductivity of the electrode. Such electrode is shown on figure 4.9. The obtained electrode is then stuck to the top brass cube with silver paste and finally

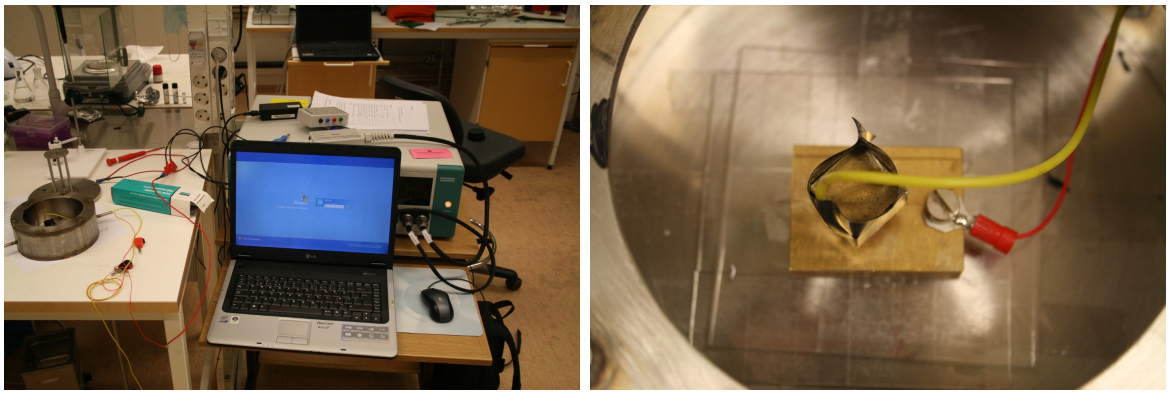

(a) Measurement setup (b) Piled electrodes

Figure 4.8: The electrical conductivity measurement setup and the electrodes

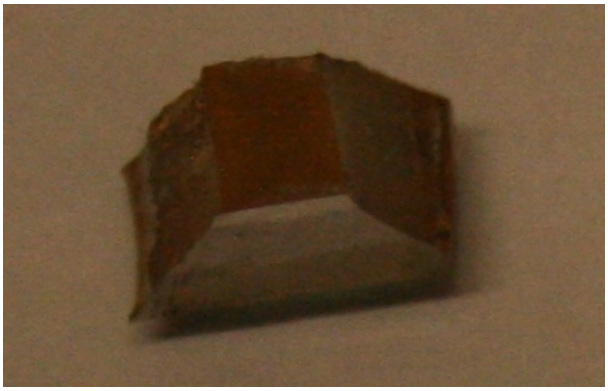

Figure 4.9: Coated PDMS electrode

placed on the sample to be measured. The potential difference applied ranges from 0 to 10 V and increases by 0.05 V/s. The resulting current is measured. Each time, about 10 measurements are done and the average of the measurements done is plotted.

Chapter 5

Experimental work

5.1 Dispersing the carbon nanotubes

The first step is to disperse the nanotubes in solvent in order to either disperse them directly on a silicon substrate or to prepare solutions of polymer mixed with nanotubes. Therefore, a solvent compatible with the polymer used as well as allowing a stable dispersion of nanotubes is required. Using surfactants in order to ease the dispersion process is possible as shown by Tan *et al* [Tan and Resasco, 2005]. However, this solution is not used in this project in order to limit the modifications brought to the nanotubes, as the risk of affecting the interaction between the nanotubes and the polymer is to be avoided. Instead, o-DCB and dimethylformamide (DMF) are solvents allowing nanotubes dispersion without surfactants of up to respectively 0.015 and 0.022 mg/mL nanotubes in solvent [Cheng et al., 2010]. As DMF does not dissolve P3HT, o-DCB is chosen to prepare the nanotubes dispersion [Chaudhary et al., 2007].
Once into solvent, the nanotubes are dispersed by sonication. However, too intense sonication can damage the nanotubes, therefore affecting their electrical properties [Lu, 1996; Geng et al., 2008]. Sonication can also damage the polymer chains, meaning that the nanotubes have to be dispersed in solvent prior to mixing them into polymer for making the nanotubes/polymer mix [Caruso et al., 2009].
Nanotubes are extremely volatile, making them difficult to handle with precision. Therefore, the nanotubes dispersion solution is made in two steps. First, a small amount of nanotubes is poured into a 1.5 mL vial and 1 mL of o-DCB is added. The vial is then shaken, wetting the nanotubes and preventing them to fly away. Next, the vial is poured into a 50 mL Erlenmeyer flask and o-DCB is added. The resulting solution is then sonicated at low power in an ultrasonic bath for one hour. The ultrasonicator used is a VWR Ultrasonic Cleaner having a working frequency of 35 kHz and has been set to 30°C, power 3. The solution made contains a high nanotubes concentration compared to what is required to have a proper dispersion. Therefore, just after the sonication process, a few milliliters are extracted in order to prepare the nanotubes dispersion containing 0.01 mg/mL nanotubes in o-DCB. Once made, this solution is also sonicated one hour in an ultrasonic bath with the same parameters as before. Both solutions are kept in closed flasks sealed with parafilm in order to avoid solvent evaporation as much as possible, keeping the nanotubes concentration unchanged.
In order to be sure of the quality of the dispersion when preparing the nanotubes/polymer

solutions or dispersing the nanotubes on a silicon substrate, the nanotubes dispersion is sonicated at low power for one hour just before being used.

5.2 Making the films

o-DCB has a vapour pressure of 1.22 mmHg at 20°C, leading to long evaporation times [Hoth et al., 2008]. This expected long evaporation time can lead to problems for making thin films. In order to check this, a solution of 10 wt % polystyrene (PS) in o-DCB containing dispersed nanotubes is made and attempts to make thin films using a spin coater are done. Several speeds ranging from 500 rpm to 3,000 rpm have been tried. The maximum spinning time used is 120 s and the acceleration is 6,000 rpm/s. The resulting films are highly defective. Indeed, after spinning, the films are still liquid, and most of the polymer has flown away during the spinning process, leading after drying to splash like patterns, as show in figure 5.1.

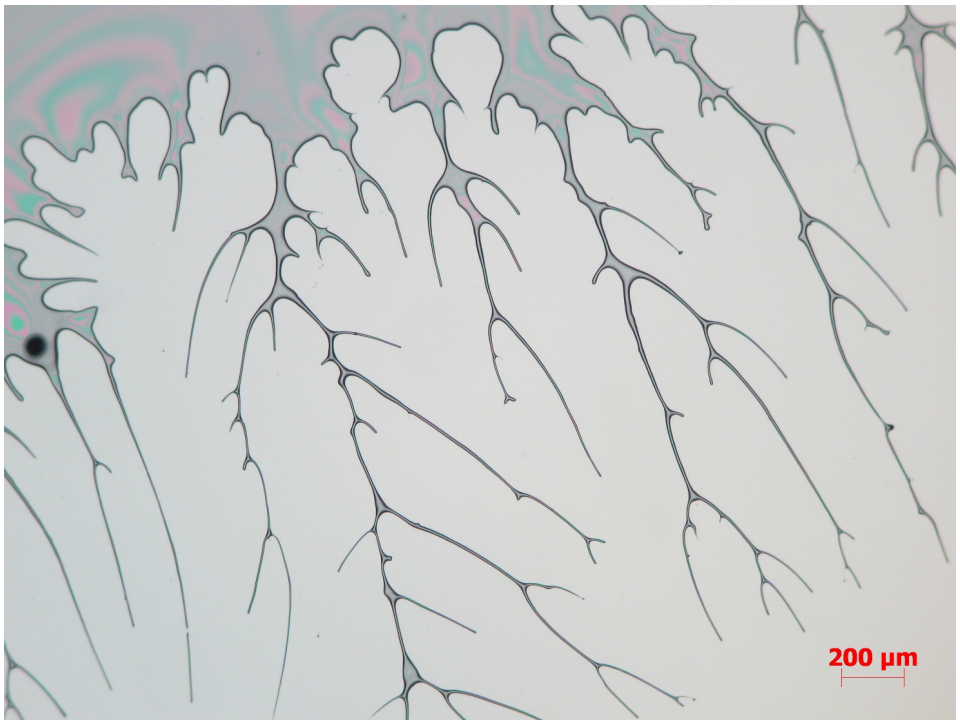

Figure 5.1: "Thin film" resulting from 10 wt % PS in o-DCB spun coated on a silicon substrate at 500 rpm

At the same time, another attemp is achieved using a 1 wt % PS solution in the nanotubes dispersion. This is done in order to try to increase the relative concentration of nanotubes compared to PS. Indeed, the 10 wt % PS solution contains 0.1 wt % CNTs. Reducing the PS concentration in the nanotube dispersion allows to increase the concentration of nanotubes relative to PS and still having a good dispersion of the nanotubes. As explained above, several spin speeds are tested in order to try to get thin films. The problems are the same: most of the solution is ejected during the spinning process and the film is still not dry after exiting the spin coater. In order for it to be dry, the film

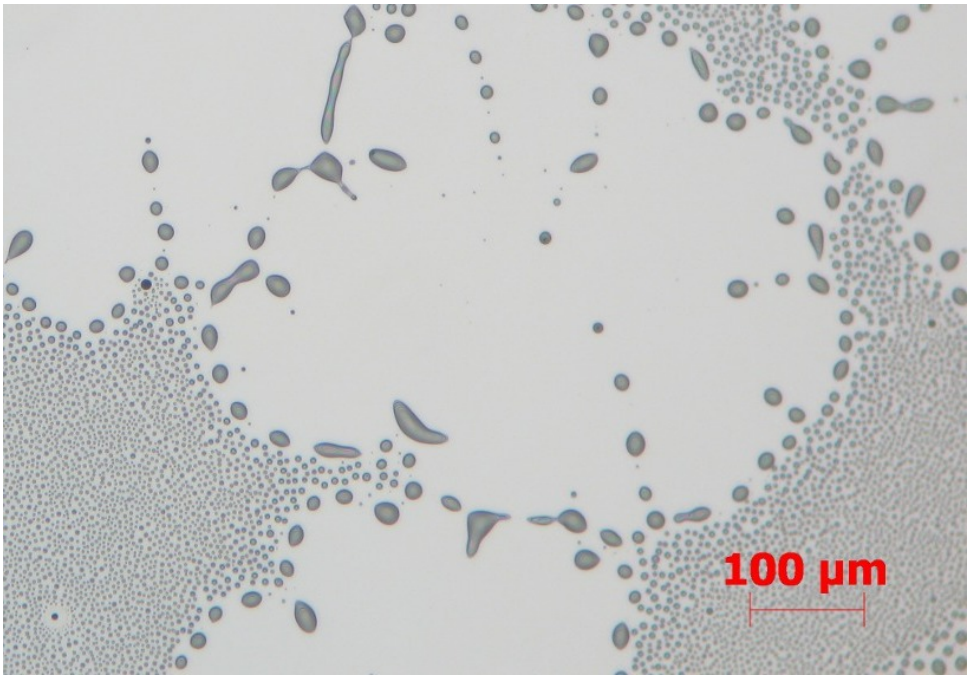

Figure 5.2: "Thin film" resulting from 1 wt % PS in o-DCB spun coated on a silicon substrate at 1000 rpm

is heated at around 100℃ during 20 min. An example of a resulting film obtained after drying is shown on figure 5.2.
A last attempt with a spin speed of 200 rpm for 120 s using an acceleration of 6,000 rpm/s seems to leave enough solution on the substrate to provide a thin film. After spin coating, the sample is kept at 100℃ during around 20 min in order to both dry and anneal the polymer film.
This method is also used to prepare P3HT films. A solution of 1 wt % P3HT in the nanotubes dispersion is made. The spin coating and the drying/annealing procedures are done, and the resulting film is then examined in optical microscopy. A picture of the resulting film is shown on figure 5.3.
Stripes of different colors can be seen: they show the evolution of the drying front during the annealing process. Those different visible colors in the polymer films also indicate that the film is not homogeneous. Another film is prepared by drop casting, and the drying process occurs at room temperature. The resulting film looks more uniform. Therefore, in order to have the same film processing conditions for PS and P3HT, all the films used in the project are made by drop casting and dried under room temperature.

5.3 Nanoimprint lithography

5.3.1 Thermal nanoimprint lithography

Experiments are conducted in order to find proper parameters for imprinting samples using thermal NIL. The imprinter used is an Eitre 3 from Obducat and is shown on

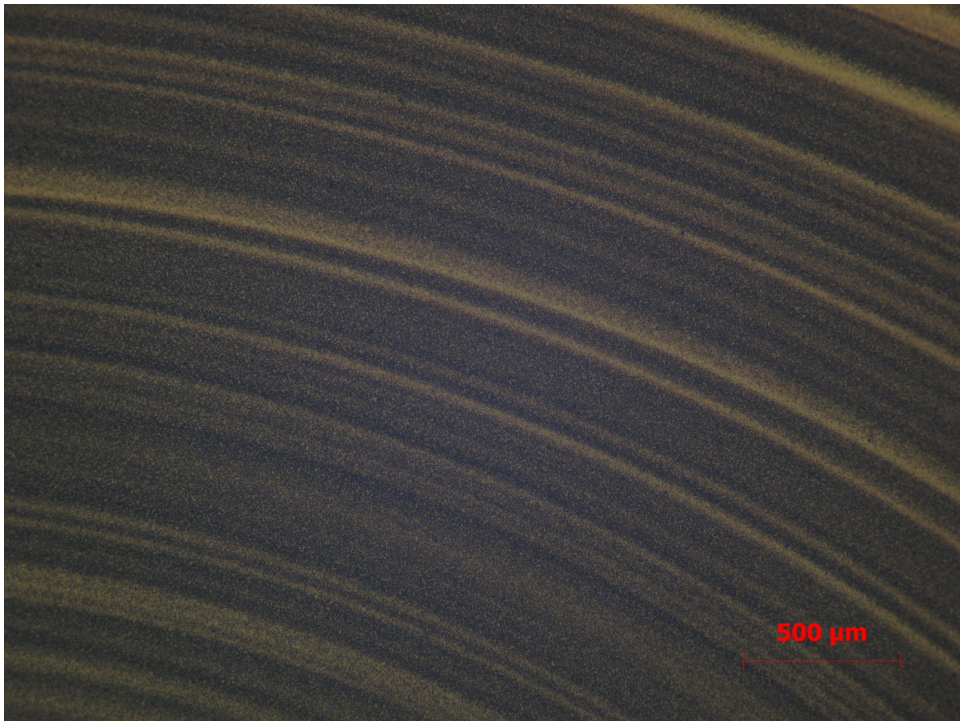

Figure 5.3: P3HT film spin coated and heated at 100℃ for 20 min

figure 5.4a. The maximum temperature available is 250℃ and the maximal pressure is 70 bar. The sample holding stage is air cooled and is shown on figure 5.4b. The sample is first placed on the sample holder. Then, the mold is positioned on top of it, and an aluminium foil covers the setup. The holder is then placed in the printing column, the printing program is entered in the controlling computer and the imprint is started. The pressure is applied on the complete aluminium foil which is deformed in the process, allowing the pressure to be distributed accross the complete area of the holder, making sure that the pressure is the same everywhere accross the sample.

First, a soft polydimethylsiloxane (PDMS) mold with different patterns is used. The patterns that are produced on this type of mold are two types of columns and two types of lines. One of each are shown on figure 5.5, along with AFM pictures.

Several temperature, pressure and time of imprint were tried without much success. Either the patterns do not appear at all on the P3HT film, or they are very faint. Examples of patterns done are shown in figure 5.6.

In addition to the lack of well defined patterns on the thin film, it is noticed that the PDMS mold gets damaged during the imprinting process. Assuming that it might be because the mold is to soft, other tests are done using an ETFE mold instead. After several tries, the thermal NIL parameters found to work well for P3HT are a pressure of 50 bar, a temperature of 170℃ and an imprint time of 600 s. An example of such an imprint is shown in figure 5.7.

Attempts to imprint polystyrene using an ETFE mold are also done. The imprinting parameters found to work well are a pressure of 20 bar, a temperature of 150℃ and an imprinting time of 180 s.

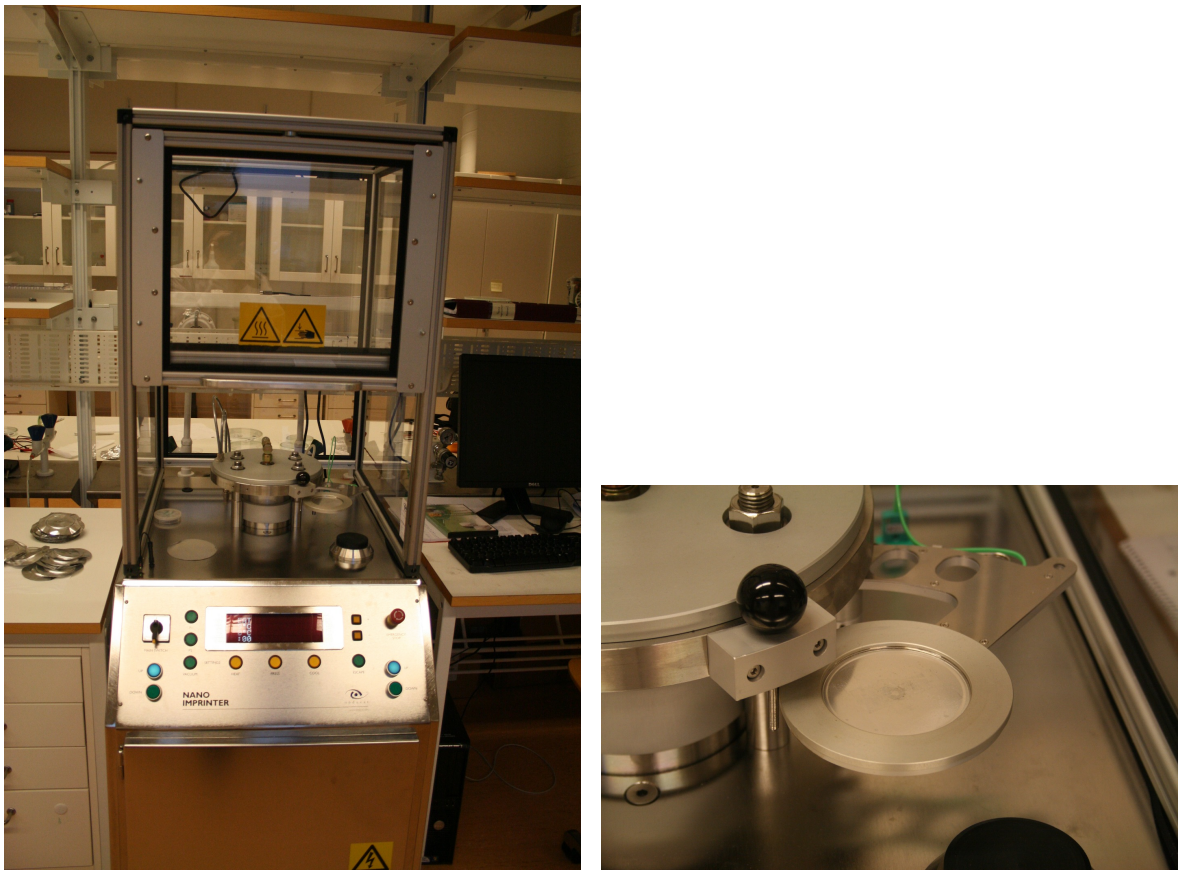

(a) Obducat Eitre 3 imprinter (b) Sample holder

Figure 5.4: Obducat Eitre 3 thermal imprinter and its sample holder

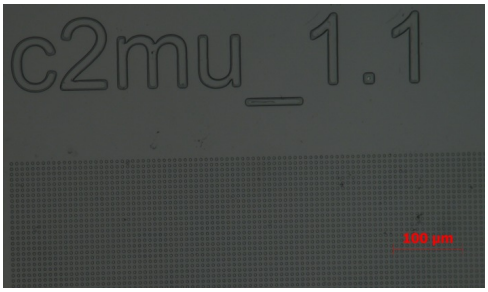

(a) Columns c2mu-1.1

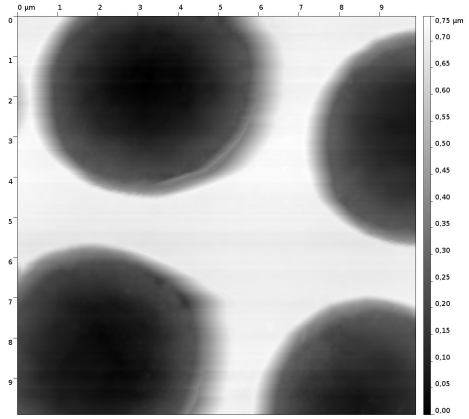

(b) AFM picture of the c2mu-1.1 patterns

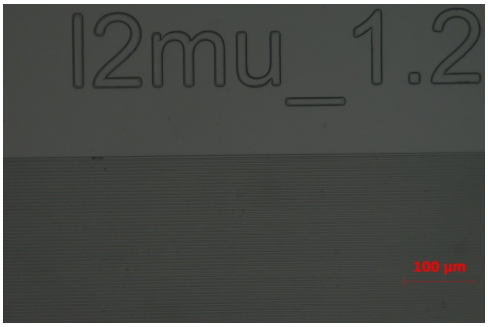

(c) Lines l2mu-1.2

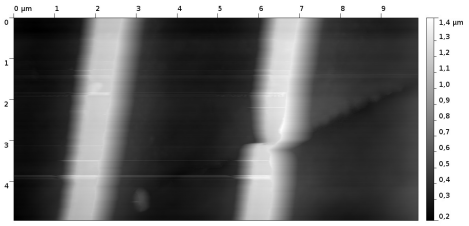

(d) AFM picture of the l2mu-1.2 patterns

Figure 5.5: PDMS test mold for thermal NIL

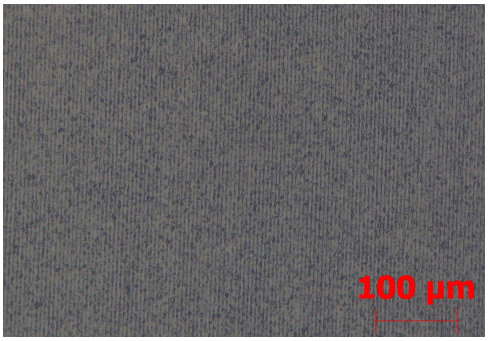

(a) Lines imprinted 300 seconds at 15 bar

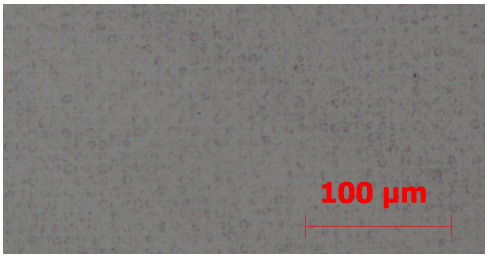

(b) Columns imprinted 900 seconds at 15 bar

Figure 5.6: Features imprinted on P3HT thin films with a PDMS mold

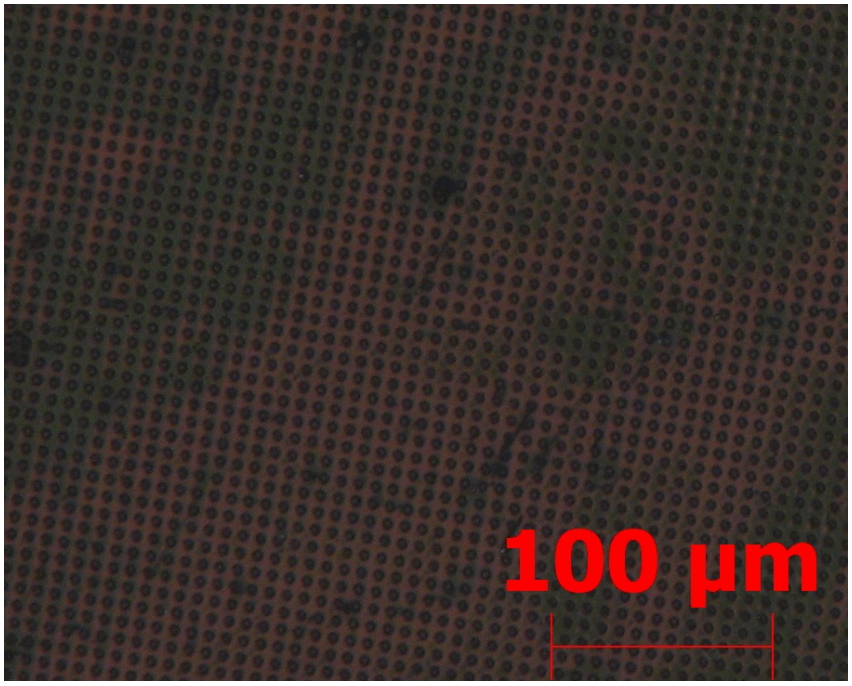

Figure 5.7: Imprinted columns using an ETFE mold on a P3HT film

5.3.2 Room temperature solvent-assisted nanoimprint lithography

In parallel to the determination of the parameters required to thermally imprint PS and P3HT films, room temperature solvent-assisted NIL is tried. The determination of the parameters required to imprint P3HT films is done in collaboration with Jianbao Zhao, another master student in Barbero's group. After several attempts, it is realised that the best way to imprint P3HT films at room temperature is to use drop casting: a drop is deposited on the substrate and is directly imprinted in the imprint chamber. The formed film then dries with the mold still in position [Zhao, 2011]. The setup used for solvent-assisted NIL is shown in figure 5.8.
Polystyrene films are easier to imprint using this imprint method. After several tries, the imprint parameters used are a wetting time with solvent entering the chamber for 2 minutes, then the mold is put in place while solvent is still entering the chamber for 2 more minutes. Finally, the mold is kept in place and the flow of solvent vapour is replaced by a flow of N_2 for about an hour, in order to dry the film. An exemple of pillars imprinted on a PS film using these parameters is shown in figure 5.9.

5.4 Electric field assisted self-assembly

For this experiment, the same chamber as the one used for solvent-assisted NIL is used. The electrodes are the one used later in the project for electric conductivity measurement. The setup has been shown in figure 4.8 on page 34. During this experiment, the film has to be liquefied, so that the nanotubes can move freely in the polymer film. In order to

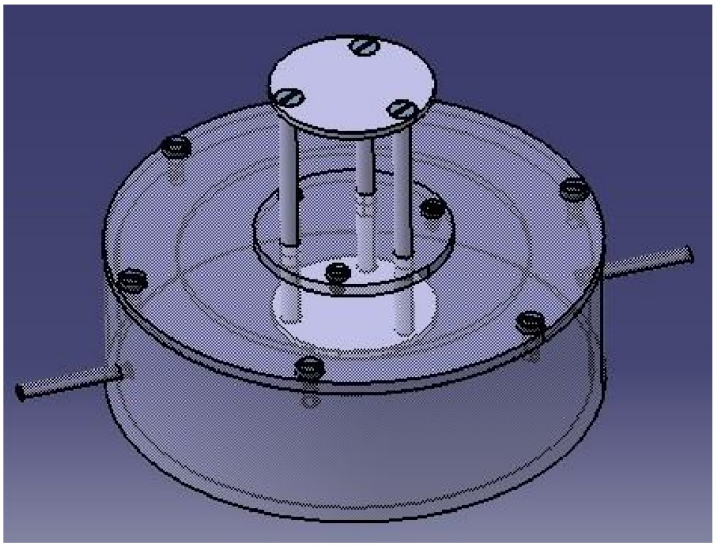

Figure 5.8: Imprint chamber for room temperature solvent-assisted nanoimprint lithography [Zhao, 2011]. The chamber is slightly transparent, and the moving piston is non-transparent. The solvant vapour enters the chamber by the tube on the right of the chamber.

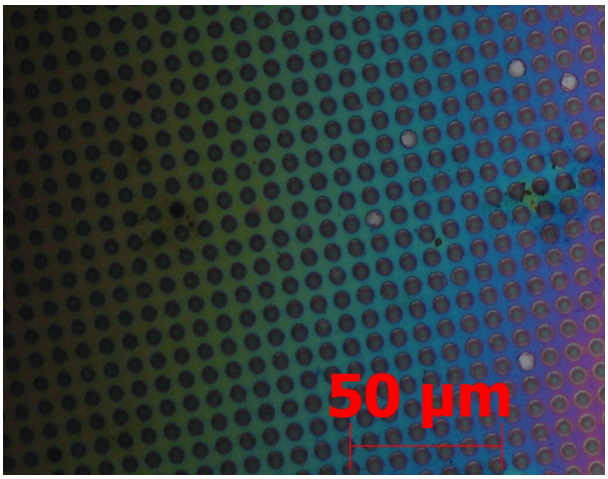

Figure 5.9: Pillars imprinted on a PS film using room temperature solvent-assisted NIL

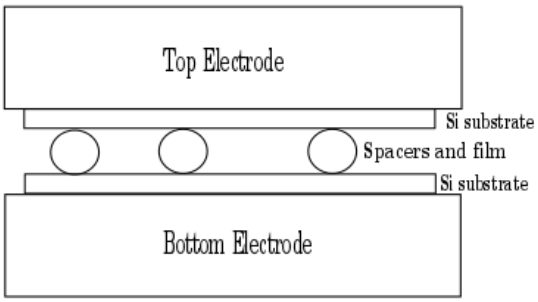

Figure 5.10: Schematic of the electric field assisted self-assembly setup

keep the polymer on the substrate and not to make it flow away under the weight of the electrodes, spacers have to be used. A schematic of the setup with the spacers is shown in figure 5.10.
The spacers used are silicate sphere of 1.56 μm. A potential difference of up to 30 Volts is applied between the top and the bottom electrode.

5.5 Substrate rubbing

A piece of PTFE is cleaned and placed in the thermal nanoimprinter on a smooth silicon substrate. It is imprinted on it at 250℃, 30 bar during 300 seconds in order to remove all the traces resulting from the manufacturing of the original PTFE sheet. Some marks are still visible after this process, but as they are very faint, the resulting piece of PTFE is used anyway. In order to align the polymer fibers, the PTFE is then placed on a piece of silicon heated up to 200℃ and rubbed in a specified direction with tweezers. Then, drops of CNTs dispersed in o-DCB are deposited on the rubbed surface and the obtained sample is let to dry in ambient temperature.

Chapter 6

Results and Discussion

6.1 Raman reference spectra

Raman spectroscopy has been heavily used in this project to map the nanotubes position in the different samples made. But in order to distinguish the nanotubes from the polymer or from the substrate, reference spectra of each material have to be known. Also, the laser wavelength has to be chosen amongst those available. Reference spectra for SWNTs using a 633 nm excitation wavelength have been found in literature and are shown in figure 6.1. The peaks shown in figure 6.1a correspond to the radial breathing mode (RBM) of the nanotubes and depend on the nanotubes diameter [Chapelle et al., 1998]. In figure 6.1b, two bands can be observed: one at around 1300 cm^{-1} and one around 1600 cm^{-1}. They are called respectively D-band and G-band. The G-band is due to the graphene sheet constituting the nanotubes and the D-band corresponds to defects in those graphene sheets [Schmid et al., 2011]. The ratio between the intensity of the D-band and the G-band can be used to characterize the amount of defects in the nanotubes [Cheng et al., 2010].
In order to be able to identify the substrate used in the different Raman measurements, spectra of a clean silicon substrate and of a clean piece of PTFE have been recorded using the 633 nm laser, as the reference spectra obtained for SWNTs looks well defined for this excitation wavelength. The measured spectra for clean silicon and clean PTFE are shown in figure 6.2.
It can be noticed for both substrate spectra that no peaks are present in the 1600 cm^{-1} region. This allows good detection of the nanotubes G-band. The silicon substrate also allows the detection of the D-band of the nanotubes, contrary to the PTFE where this detection is made difficult due to the presence of peaks in the 1200–1400 cm^{-1} region. Also, with both substrates it is difficult to determine the nanotubes RBM, as both substrates have peaks in the 100–500 cm^{-1} region.
Finally, reference spectra for P3HT and polystyrene are also recorded with a 633 nm excitation wavelength and are shown in figure 6.3.
The P3HT spectrum shown in figure 6.3a shows a peak at around 1500 cm^{-1} on top of a broad feature. This broad feature is due to fluorescence effect, meaning that the laser power required to measure the P3HT signal has to be weak in order not to saturate the Raman spectroscope detector. This might prove problematic for detecting nanotubes mixed in P3HT, as the nanotubes might not react to the laser excitation if the laser

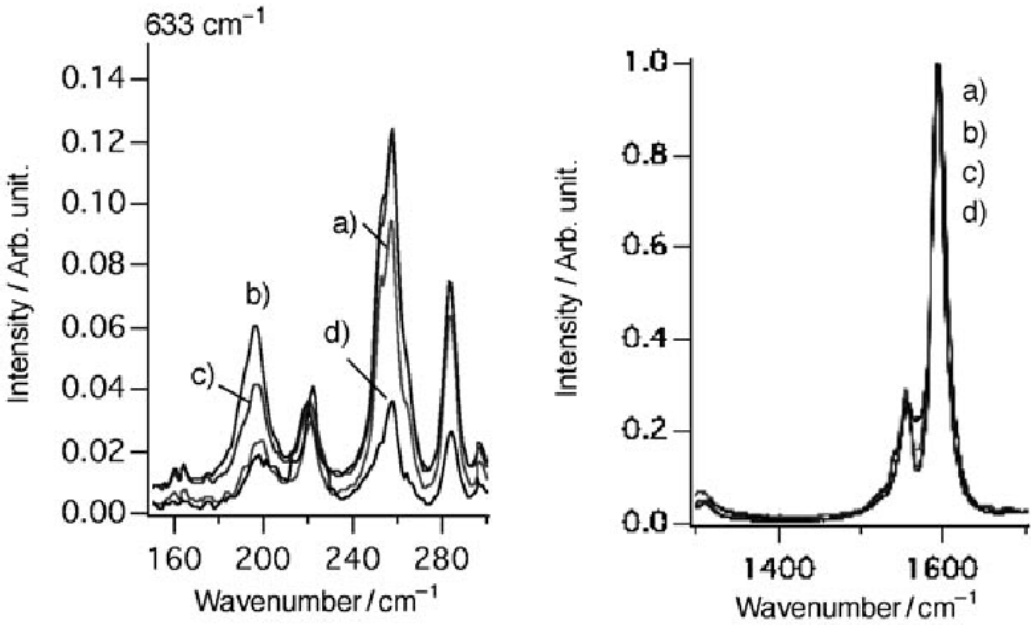

(a) Radial breathing mode

(b) D and G band

Figure 6.1: Raman spectra of CNT films prepared from mixed solvents. a) ODCB, b)ODCB-MeOH, c) ODCB-benzene and d) ODCB-$CHCl_3$. 633 nm excitation wavelength. [Maeda et al., 2009]

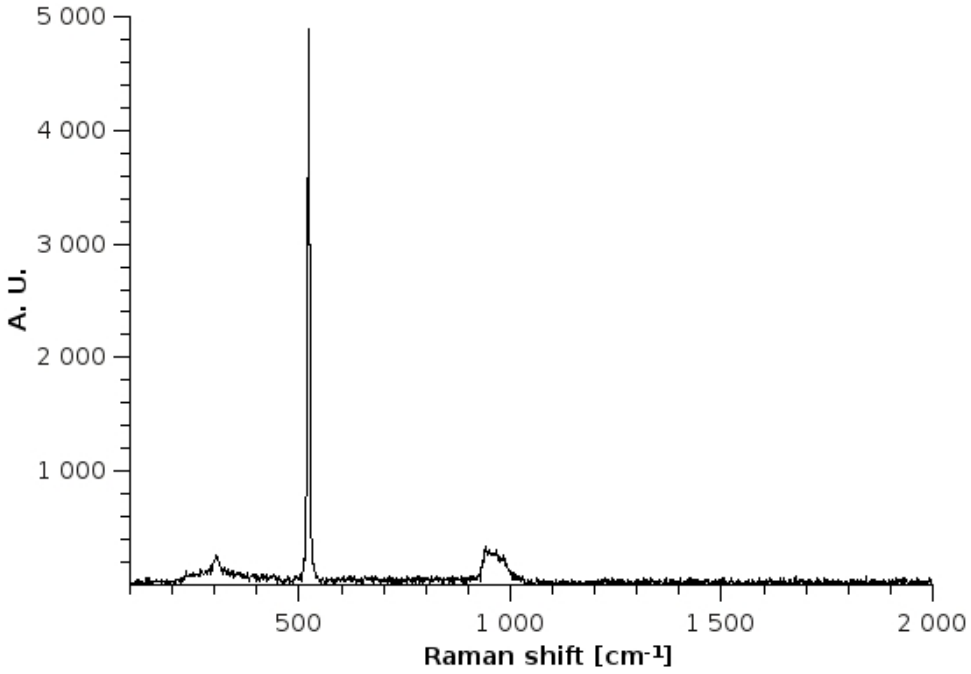

(a) Si substrate

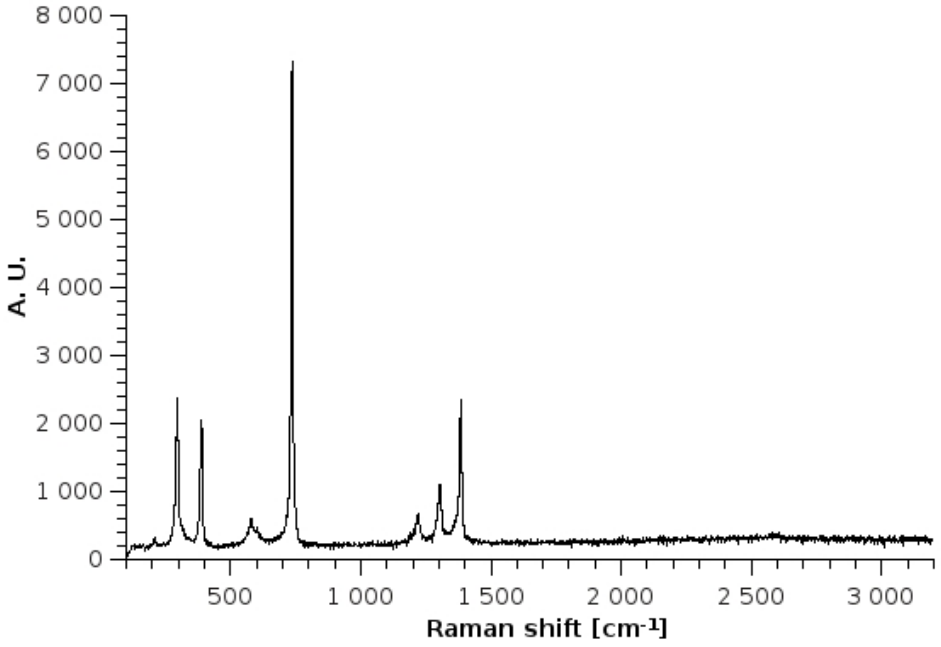

(b) PTFE substrate

Figure 6.2: Reference spectra for Si (a) and PTFE (b) recorded with a 633 nm excitation wavelength

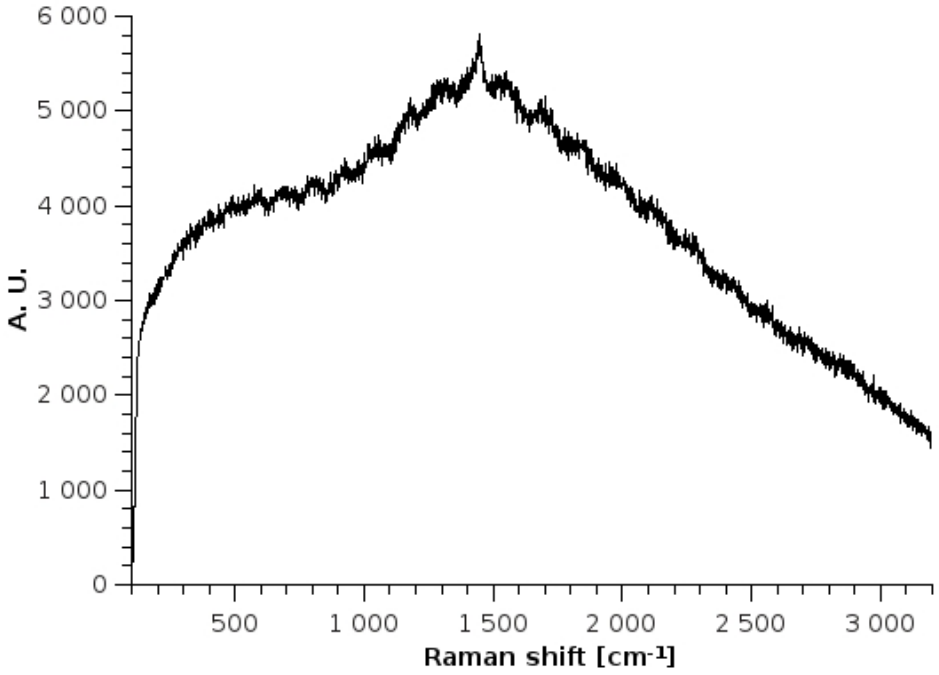

(a) P3HT on Si substrate

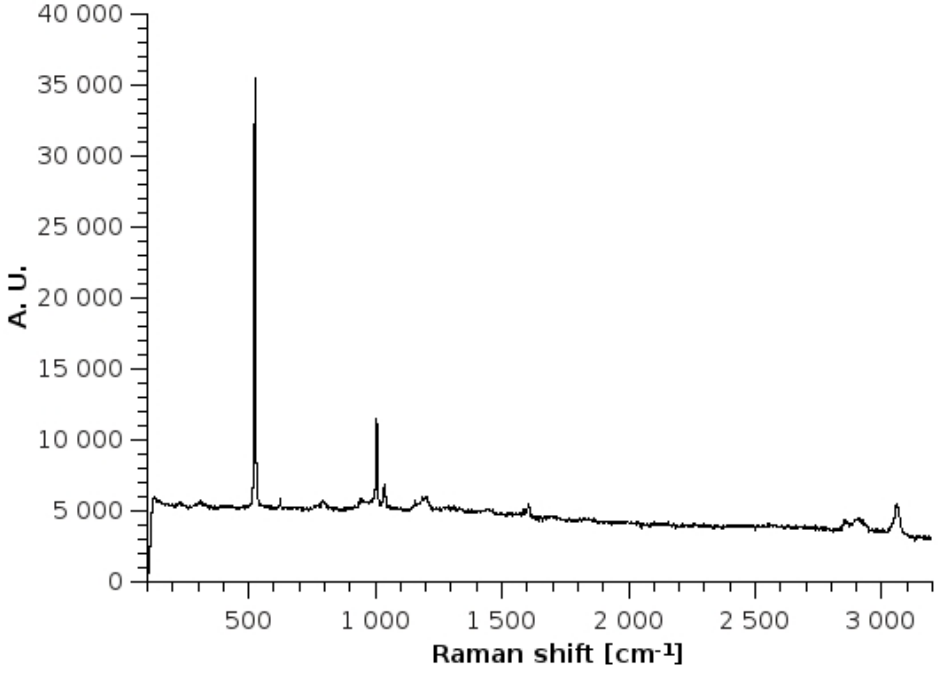

(b) PS on Si substrate

Figure 6.3: Reference spectra for P3HT (a) and PS (b) on silicon substrate recorded with a 633 nm excitation wavelength

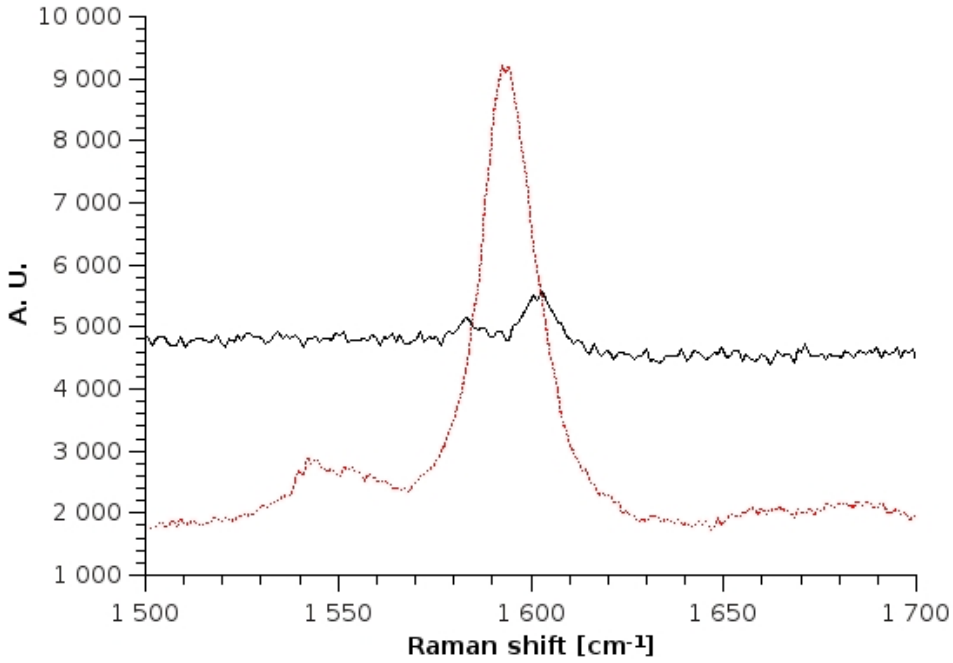

Figure 6.4: Close-up on the 1600 cm^{-1} peak in the PS and the PS/CNTs Raman spectra. Both spectra are recorded at an excitation wavelength of 633 nm, with a single 10 s accumulation. *Black continuous line*: pure PS film, spectrum recorded with a laser power of 2 mW. *Red dotted line*: PS/CNTs mix, spectrum recorded with a laser power of 1 mW.

power is too weak. Indeed, the spectrum figure 6.3a has been recorded at 0.0001 % of the laser power, which corresponds to a power of about 0.02 μW. It can be noticed that the silicon peak from the substrate at around 500 cm^{-1} is masked, which might be due to the combination of the film thickness and the fluorescence from P3HT.

The PS spectrum in figure 6.3b shows several peaks, including one in the 1600 cm^{-1} area. This one could pose problems as it might interfere with the peaks coming from the nanotubes. Therefore, a PS/CNTs mix has been done and Raman spectroscopy measurements have been done in order to compare the signal between pure polystyrene and polystyrene with mixed nanotubes in the 1600 cm^{-1} region. The resulting spectra are shown on figure 6.4.

It is quite clear that even if it has been recorded at a higher power, the signal coming from the polystyrene is less intense than the combined PS/CNTs signal, even recorded at a lower power. This means that the signal from the nanotubes is predominant compared to the polystyrene signal, meaning that the detection of CNTs can be achieved by targeting the 1600 cm^{-1} peak.

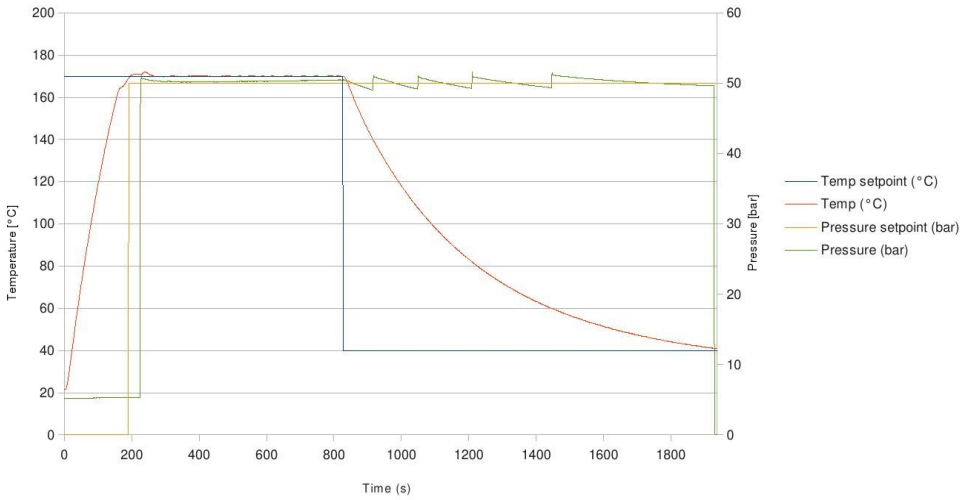

Figure 6.5: Imprint log of the P3HT/CNTs mixed thin film

6.2 Effect of nanoimprint lithography on nanotubes distribution

Two different techniques have been used to prepare the polymer/CNTs film:

- Homogeneous polymer/CNTs mixtures,
- Two layer films, with the nanotubes deposited first and pure polymer drop-cast on top.

6.2.1 Polymer/nanotubes mix films

A solution containing 1 wt % nanotubes dispersed in a 0.1 wt % P3HT dissolved in o-DCB has been made, and a film has been drop-cast with this solution. The obtained film has been thermally imprinted at 170℃ at a pressure of 50 bar for 600 seconds using a flexible ETFE mold, as shown in figure 6.5. The resulting patterns are shown in figure 6.6.
The resulting film is examined using Raman spectroscopy. However, due to the fluorescence issue coming from P3HT, the laser power to be used is too low for the nanotubes to produce a signal, as shown in figure 6.7.
Indeed, only the signal coming from P3HT is visible. The extremely sharp peak obtained at around 1650 cm^{-1} is probably due to a cosmic ray hitting the detector during the measurement. In order to decrease the fluorescence effect from P3HT, other excitation wavelengths are used and longer exposition times are tried in order to have a signal coming from the nanotubes. After several attempts, the help of Thomas Wågberg proved effective and signal from the nanotubes is detected, as shown in figure 6.8. The parameters used are an excitation wavelength of 785 nm, 20s accumulation time, 10 accumulations and a laser power of 0.3 mW.
The peak from nanotubes is expected to shift slightly from the 1600 cm^{-1} value due to the change in excitation wavelength and appears in the spectrum at around 1510 cm^{-1}

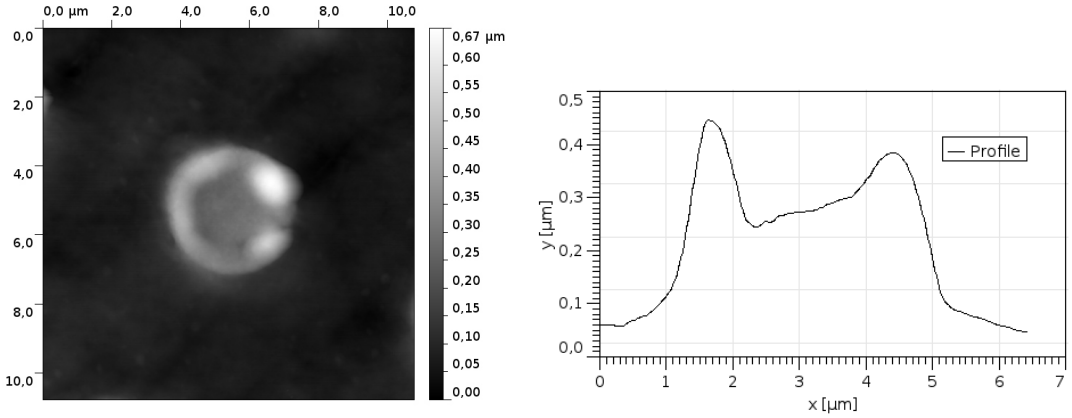

(a) AFM picture (b) Profile

Figure 6.6: AFM picture of the resulting patterns of the P3HT/CNTs mixed film. The columnar structure is not completely filled as can be seen in figure 6.6b, due to non optimal imprinting conditions.

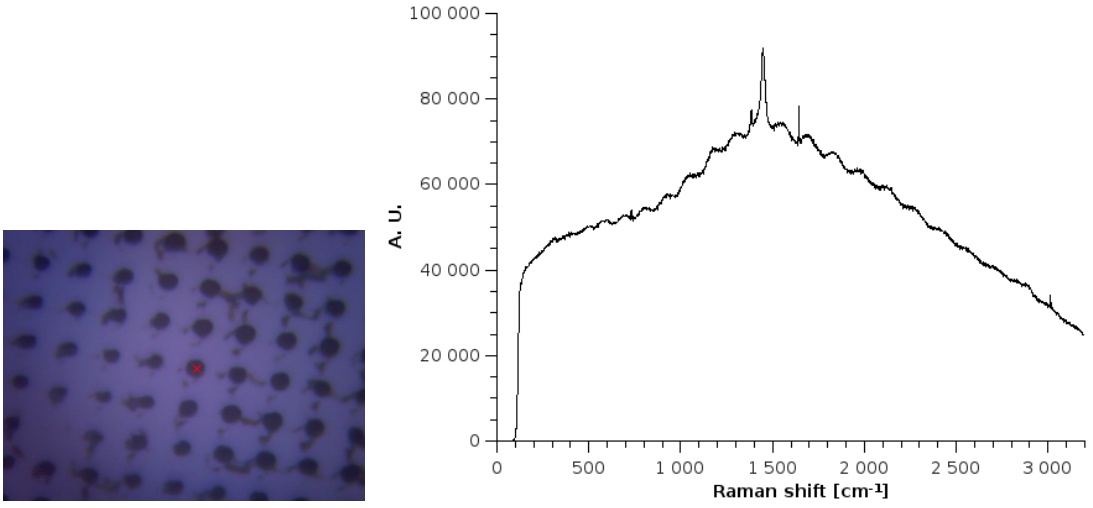

(a) Measured spot (b) Raman spectrum

Figure 6.7: The red cross in figure 6.7a shows the measured spot. Figure 6.7b shows the resulting Raman spectrum obtained with an excitation wavelength of 633 nm and a power of 0.02 μW. The sample used for the scan is the same as in figure 6.6.

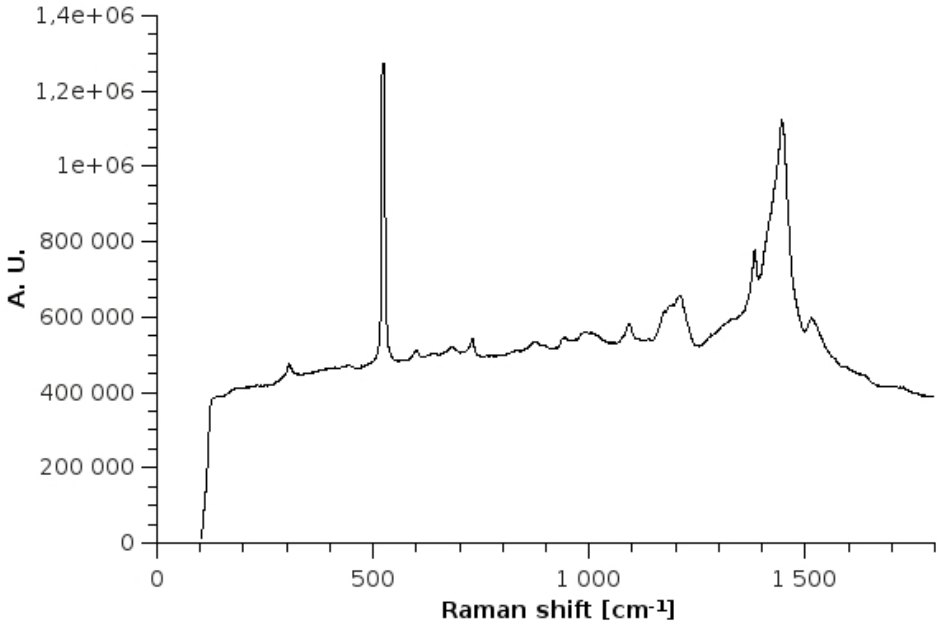

Figure 6.8: Raman spectrum at an excitation wavelength of 785 nm, 20s accumulation time, 10 accumulations and a laser power of 0.3 mW. The sample is the same as shown in figure 6.6.

[Heise et al., 2009]. This single measurement takes around 20 minutes, and the signal gathered from the nanotubes is still weak compared to the background signal, making it problematic to map the sample using Raman spectroscopy. A rough map consisting of 25 scans has been made around a pillar. The mapping took about 7 hours to complete, and the map of the CNTs peak can be seen in figure 6.9.
This map does not show any clear effect coming from the pillars. The only noticeable effect is the seemingly low concentration of nanotubes on the left side of the map, in the area which seems to be completely between the pillars. However, the signal from the nanotubes is weak and the map resolution is low. Increasing the number of accumulations can improve the gathering of the nanotubes peak but this means that the scans will take longer time to complete. Also, this map has steps of 2.5 μm between each scan. The pillar being slightly less than 4 μm in diameter, it is obvious that the resolution of the map has to be increased. Indeed, this method would work better with a smaller step size to better differentiate the pillars from the area outside the pillars. However, considering the long measurement time, other solutions have to be found to characterize the nanotubes in the imprinted sample.
SEM has been conducted on the sample using both secondary electrons detection and back-scattered electrons detection, and the resulting pictures are shown in figure 6.10.
The secondary electron image in figure 6.10a shows the topography of the sample. It can be seen that the residual polymer layer between the pillars is really thin, in the order of 100 nm. The back-scattered electrons image in figure 6.10b shows that the pillar in the front has a fairly homogeneous composition, indicating that the CNTs dispersion in the polymer mix is fairly good. The fact that the nanotubes are too small to be observed

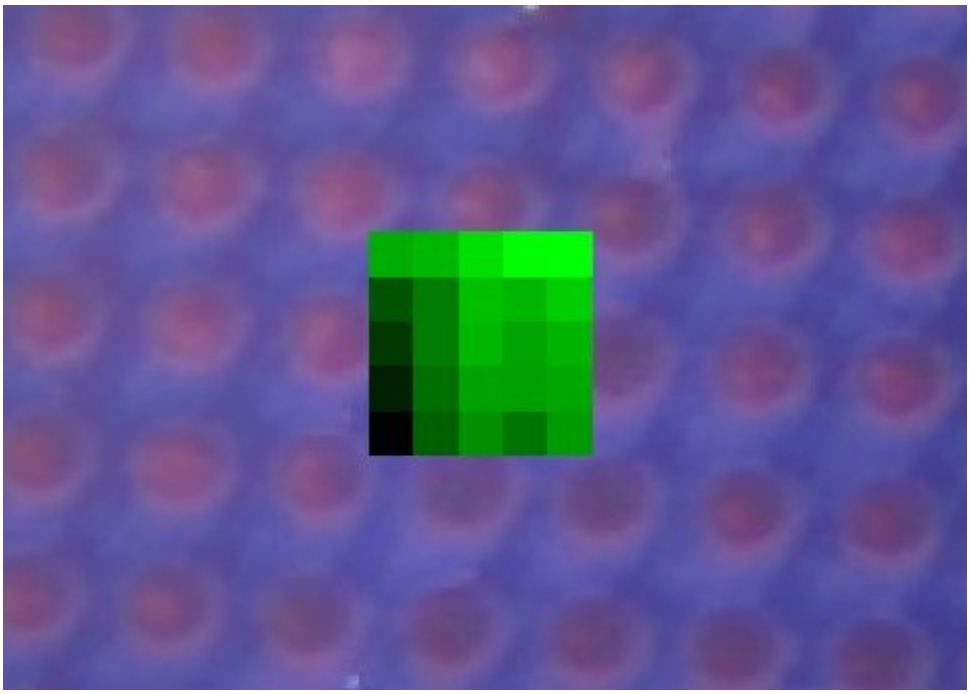

Figure 6.9: Mapping of a P3HT/CNTs pillar with a 785 nm excitation wavelength. The laser is focused at the bottom of the features, as shown on figure 6.13a. The sample is the one shown in figure 6.6.

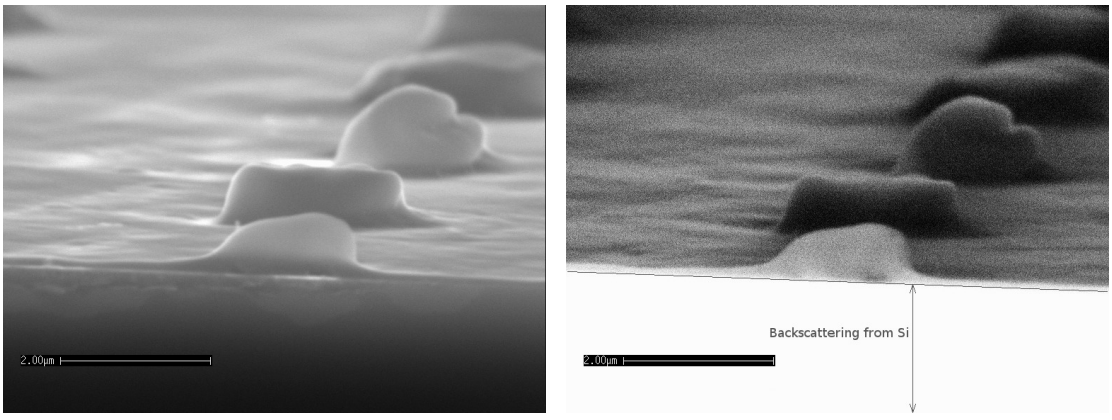

(a) Secondary electrons (b) Back-scattered electrons

Figure 6.10: SEM picture of pillars not fully imprinted in P3HT/CNTs film. The white layer on the right image is the silicon layer. The scale bar represents 2 μm. This sample was made in the same conditions as samples from figures 6.6 to 6.9.

directly with the available SEM prevents to draw any conclusion about the influence of the nanoimprint lithography process on their orientation when using a direct mix between the polymer and the nanotubes.

6.2.2 Dual layer films

PS/CNTs dual layer film In order to better visualize the effect of NIL on the mixing of CNTs in the polymer film, samples made of two different layers are prepared. First, nanotubes are spread on a silicon substrate by letting drops of CNTs dispersed in o-DCB directly dry on the substrate at ambient temperature. Then, a layer of either polystyrene or P3HT is added, using the same technique as the one used to deposit the nanotubes. Therefore, the difference in nanotubes concentration in the sample is expected to be easier to characterize, and the possible effect of nanoimprint lithography on the nanotubes dispersion will be easier to assess.
A thin film is made with a layer of deposited CNTs on a silicon substrate and polystyrene is drop-cast on top in order to form a dual layer sample. Polystyrene is used here in order to be able to characterize the sample using Raman spectroscopy and to avoid fluorescence issues. A sample is patterned using solvent-assisted NIL with a flexible ETFE mold. The following procedure is followed:

- The sample is placed in the imprint chamber and toluene vapour is introduced during 20 minutes.
- The mold is placed on the sample and toluene vapour is still flowing in for 20 minutes.
- The mold is kept in place and N_2 is flowing in for 1 hour in order to dry the sample.

Some areas exist on the sample where the patterns are not well defined. However, large areas with patterns such as shown on figure 6.11 are well defined.
Raman spectroscopy is then used to track the nanotubes in the sample. The laser is focused in a plane at the base of the pillars, as shown in figure 6.13a, point F. The map consists of around 6000 scans, with a 0.2 μm step. The excitation wavelength is 633 nm and each scan consists of one acquisition lasting 1 s. The total scanning time is about 2h15. The 1600 cm^{-1} peak corresponding to the nanotubes has been tracked in a (1594 cm^{-1} – 1607 cm^{-1}) window and the resulting map is shown in figure 6.12.
The brighter the area in figure 6.12, the higher is the nanotubes concentration. From the Raman map, it is quite clear that the nanotubes have diffused in the polystyrene layer. Their presence is even more intense in the patterned pillars, which seems to indicate that the nanotubes effectively followed the polymer flow during the imprint process. This high resolution mapping seems to confirm the initial low resolution mapping in the P3HT/CNTs mixed film shown in figure 6.9. This can mean that the diffusion of the nanotubes in the polystyrene film is most likely due to the nanoimprint process. In order to check if the nanotubes diffusion is not due to a too thin film, thickness measurement of the area mapped in Raman is attempted using AFM. The resulting picture is shown in figure 6.13.
The AFM measurement seem to indicate that the film is pretty thick (hr$\geq$4 μm). Indeed, the tip of the AFM is unable to reach both the top of the film as well as its bottom, as

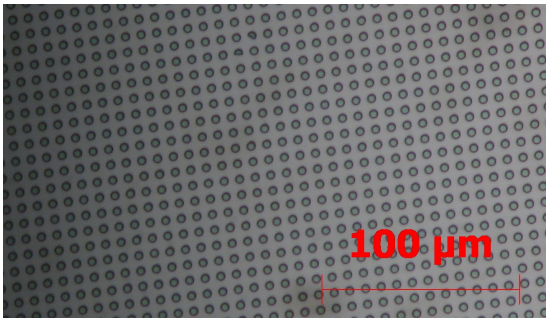

(a) Optical microscopy

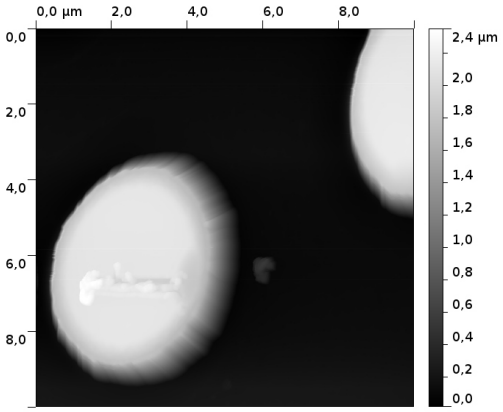

(b) AFM

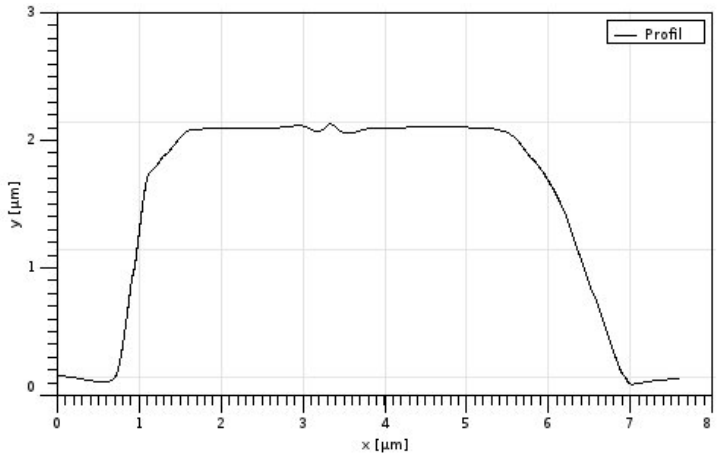

(c) Profile of the pillar

Figure 6.11: Solvent-assisted NIL fully imprinted patterns on a PS/CNTs film

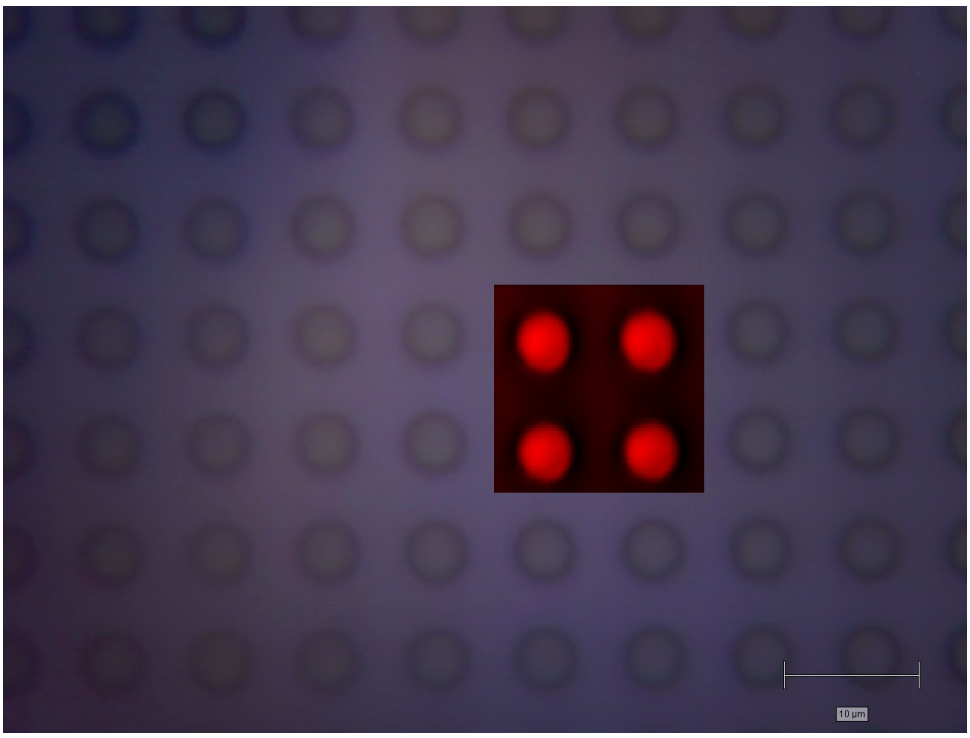

Figure 6.12: Distribution of the nanotubes concentration in a solvent imprinted PS/CNTs dual layer film at room temperature. The mapping focuses on the 1600 cm^{-1} peak. The intensity can be related to the amount of CNTs in the imprinted film. Brighter spots represent higher CNT content.

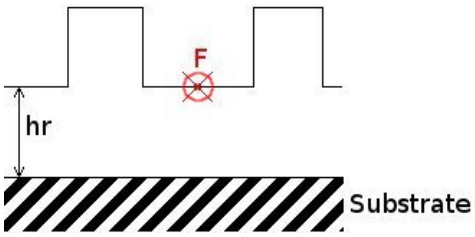

(a) Schematic of the film

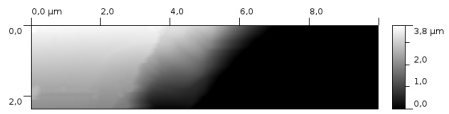

(b) AFM height image

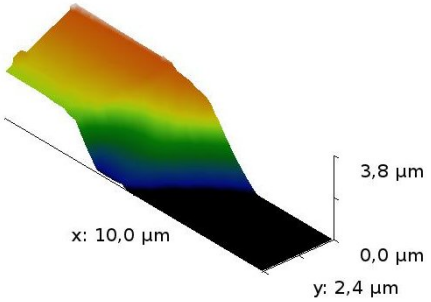

(c) 3D representation

Figure 6.13: Thickness measurement of the PS/CNTs patterned dual layer sample. In the schematic, *hr* represents the thickness of the residual layer, measured in the AFM picture by making a cut in the sample. *F* is the focal point where the laser has been focused for making the map shown in figure 6.12.

indicated by the pitch black area in the figure 6.13. The scanner z-range used is around 3.5 μm. In order to confirm this hypothesis, other samples are made, using P3HT which is a more useful material for patterning interfaces in solar cells.

P3HT/CNTs dual layer film In the same way as for the PS/CNTs dual layer films, first a layer of CNTs is deposited on a silicon substrate. This layer is made by covering the substrate with the CNTs dispersed in o-DCB dry on the substrate. Then P3HT is deposited on top of it by letting about 50 μL of a 2 wt % P3HT solution in chloroform dry on the deposited CNTs. As P3HT films are problematic to imprint using room temperature solvent-assisted NIL, only thermal NIL is used. The mold used is a flexible ETFE mold and the imprint parameters are the ones determined in chapter 5, section 5.3 on page 37 (170℃, 50 bar, 600 seconds). Because of problems with fluorescence, it has been decided to use SEM to image the imprinted film. Although SEM gives a different information than Raman spectroscopy, the back-scattered mode can give useful information about differences in densitiy in the films. Because of the difference in electronic density between CNTs and P3HT, it is expected to get a stronger back-scattered signal for the CNTs [Pensack et al., 2010].
The obtained sample are freeze-fractured and characterized in SEM in order to track the differences in density in the material, i.e. the position of the nanotubes after the imprint process. The cut is done in liquid nitrogen with the help of a scalpel blade in order to fracture the samples from the side, therefore preventing the film to peel off from the substrate. Several pictures obtained are shown in figure 6.14.
The SEM pictures show that the pillars have about the same dimensions as the ones shown in figure 6.11. The film thickness in the sample is about 18 μm. This high thickness combined with the density contrast appearing in the imprinted pillars seems to show that the NIL process has indeed an effect on the nanotubes distribution in the sample. The examined pillars shown in figure 6.14 are well defined, as shown by the secondary electrons pictures. Moreover, the back-scattered electrons pictures show high differences in material density across the sample.
What seems to be a difference in material density at the bottom of the film is in fact related to the topology of the sample, as shown on the secondary electrons pictures. Indeed, the fracture plane across the polymer film is not really plane in that area and the high irregularities in the material disturb the back-scattered electron measurements. However, the secondary electrons pictures show that the cut across the pillars is fairly regular. Only faint disturbances are visible, and are reflected equally faintly in the back-scattered electrons images. This is particularly visible in pictures 6.14e and 6.14f with the two vertical lines going downwards and starting at the top of the pillar.
Once the influence of the defects in the fracture plane has been taken into account, it is clear that the remaining contrasts in material density visible on the SEM pictures are not artifacts due to the topography of the pillar. The remaining explanation is that the nanotubes have been dragged along during the imprint process. But as the film is quite thick, the top of the mold has probably been filled with pure P3HT, preventing the nanotubes coming from the bottom of the film to travel completely up to the top of the pillars, as can be seen in figures 6.14b and 6.14f. Figure 6.14d shows CNTs reaching the top of the imprinted pillar.
Finally, XPS has been conducted on the sample in order to check if the nanotubes have

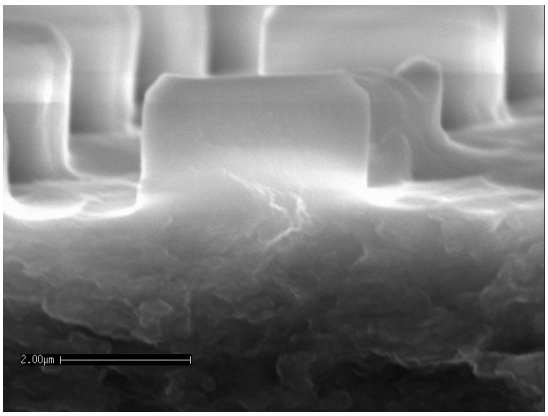

(a) Secondary electrons

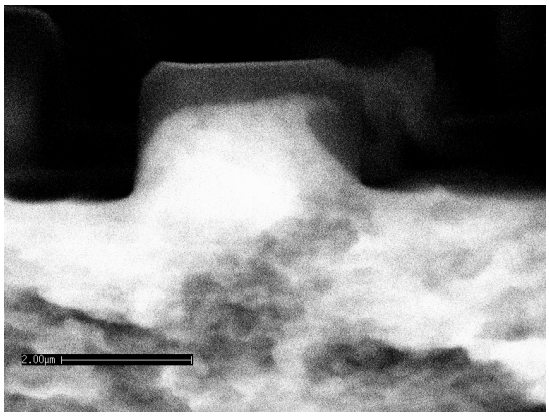

(b) Back-scattered electrons

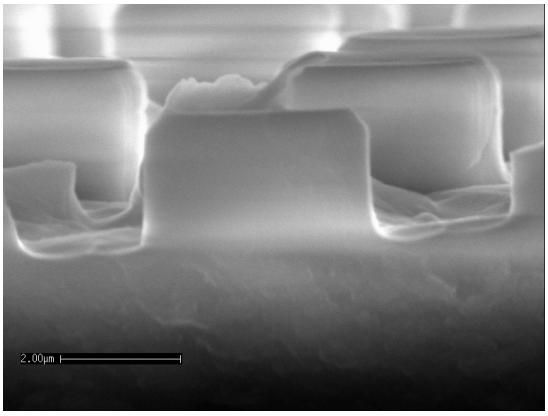

(c) Secondary electrons

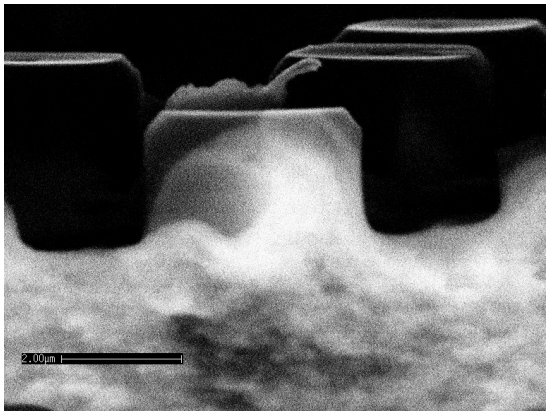

(d) Back-scattered electrons

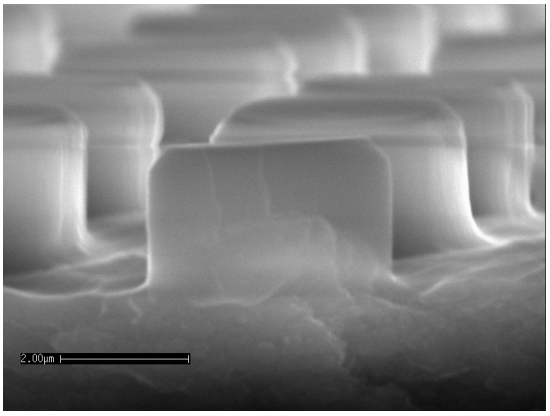

(e) Secondary electrons

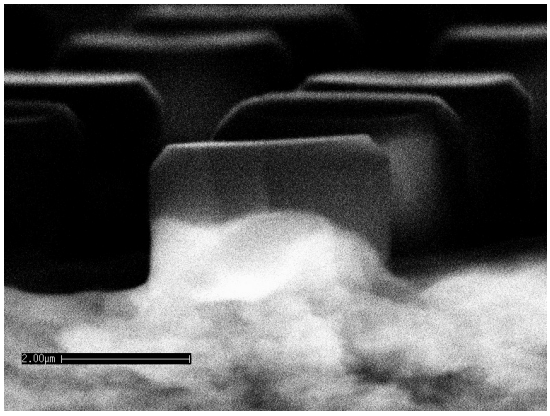

(f) Back-scattered electrons

Figure 6.14: SEM pictures of several cut pillars in a P3HT/CNTs dual layer sample thermally imprinted at a temperature of 170℃ and a pressure of 50 bar during 600 seconds. The scale bar represents 2 μm.

Measurement point	C/S ratio
Nanotubes on Si	–
Pure P3HT	14.3
Non imprinted sample	12
Patterned area, first spot	21.1
Patterned area, second spot	21.0
Outside patterned area	13.1

Table 6.1: XPS measurements results

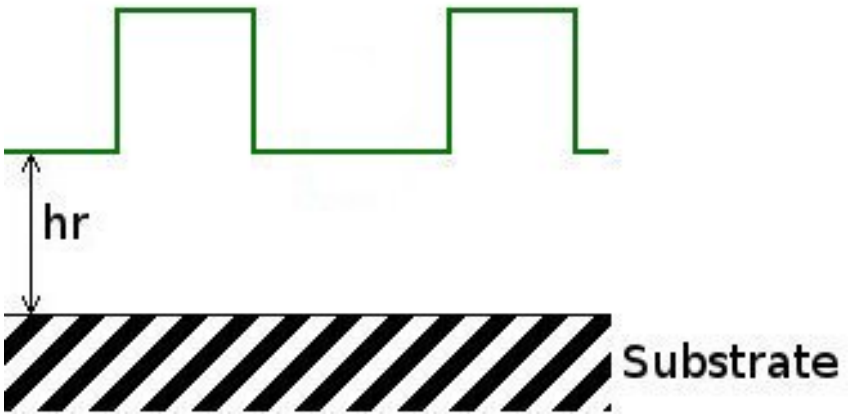

Figure 6.15: Representation of the surface area measured by the XPS. The imprinted patterns are not to scale. The thicker green line shows the thickness of the sample effectively measured by XPS. *hr* is the residual layer of the film.

traveled across the film everywhere or just in the imprinted areas. Therefore, measurements have been done both inside and outside the imprinted area. Reference measurements on CNTs deposited on silicon substrate and measurements on pure P3HT have also been accomplished. The different results are shown in table 6.1. It has to be remembered that XPS measurements probe the sample at the surface, and that the depth of the measured area is around 10 nm, as shown in figure 6.15.

In the XPS measurements, sulfur is used as a reference considering that it is present in P3HT. It is visible in the XPS measurements results that the carbon content in the patterned area is higher compared to the one outside of the patterned area. As explained on figure 6.15, this clearly involves a higher CNT content near the surface of the sample. Airborne carbon contamination from the lubrification of the XPS spectroscope can increase the amount of carbon recorded on the sample, but this contamination is expected to be similar for all samples, meaning that the increase in carbon content in the patterned areas is not due to it. The three different methods (Raman spectroscopy, XPS, SEM) used to probe the CNT distributions after imprinting seem to agree, and indicate that NIL increases the amount of CNTs inside the imprinted features.

6.3 Effect of electric-field assisted self-assembly on nanotubes distribution

For this experiment, a dual layer sample is made. First, CNTs from a dispersion in o-DCB are deposited on a silicon substrate. Then, the polystyrene layer is done by drop casting on the deposited nanotubes. The sample is then placed in a chamber on a brass electrode. Silver paste is used to improve the conductivity between the silicon substrate and the electrode. The top electrode consists of a silicon substrate on which 1.56 μm silicate sphere are deposited in order to act as spacers. This substrate is placed on a brass electrode with silver paste applied in between in order to improve the conductivity. Then this top electrode is positioned on top of the dual layer sample, as has been shown in figure 5.10 on page 43.
The chamber is then closed and toluene vapour is introduced while a 30 V potential is applied. After two hours, toluene vapour is replaced by a N_2 flow for two hours while the potential is still applied. Finally, the generator is switched off, the N_2 flow is stopped and the dry sample is extracted from the chamber. When the potential difference was applied, a small leak current of a nearly constant value of 0.04 mA was measured during the experiment. Once out of the chamber, the top electrode is removed and electrical conductivity measurements are done.

6.4 Electrical conductivity measurements

6.4.1 Sample processed by electric-field assisted self-assembly

Measurements are achieved on a PS/CNTs dual layer sample which has not been submitted to electric field and on one which has been submitted to the electric field. The resulting curves are shown on figure 6.16.
Both curves are noisy, which is not surprising considering the involved intensities. However, it is quite clear that the reference sample does not conduct electricity. This is not unexpected, as polystyrene does not conduct electricity and the nanotubes lay mostly at the bottom of the sample. However, the graph in figure 6.16b positively shows conductivity. This can mean that the nanotubes have moved during the electric field assisted self assembly process and act as conducting paths for the electrons. It is not quite clear if they have only moved due to the field, and if the result can be improved. Indeed, in litterature, alternating fields are used to align the nanotubes during their growth [Ural et al., 2002]. Therefore more experiments with alternating fields of different amplitudes and frequencies should be done to asses their effect on the nanotubes distribution in the sample. Also, high resolution TEM should be achieved in order to be able to individually see the nanotubes and therefore precisely determine their position and their possible alignment.

6.4.2 Sample processed by nanoimprint lithography

Electrical conductivity measurements on thermally nanoimprinted samples have also been done. First, the electrical conductivity of pure P3HT has been measured as a reference

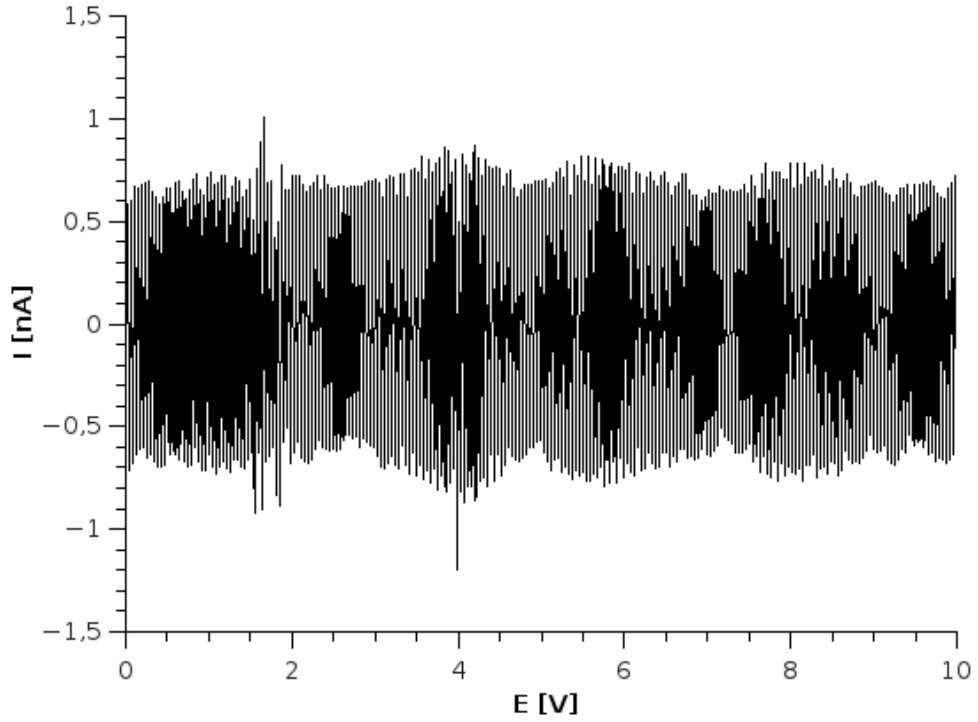

(a) Reference sample

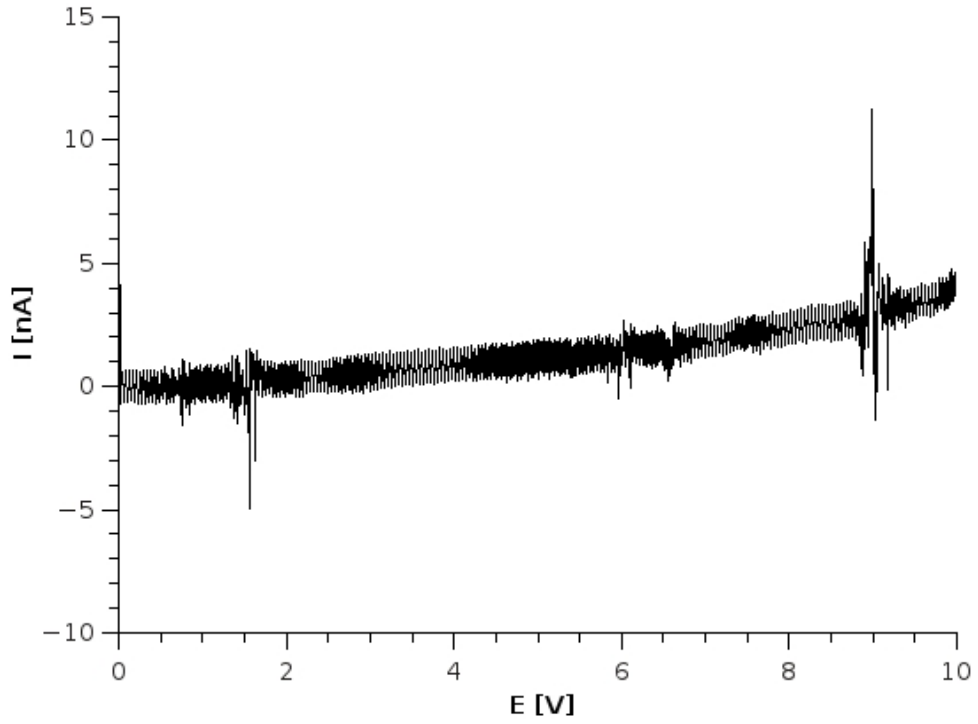

(b) Treated sample

Figure 6.16: Electrical conductivity measurements. *Top graph*: Reference dual layer sample. *Bottom graph*: Dual layer sample having been submitted to electric field.

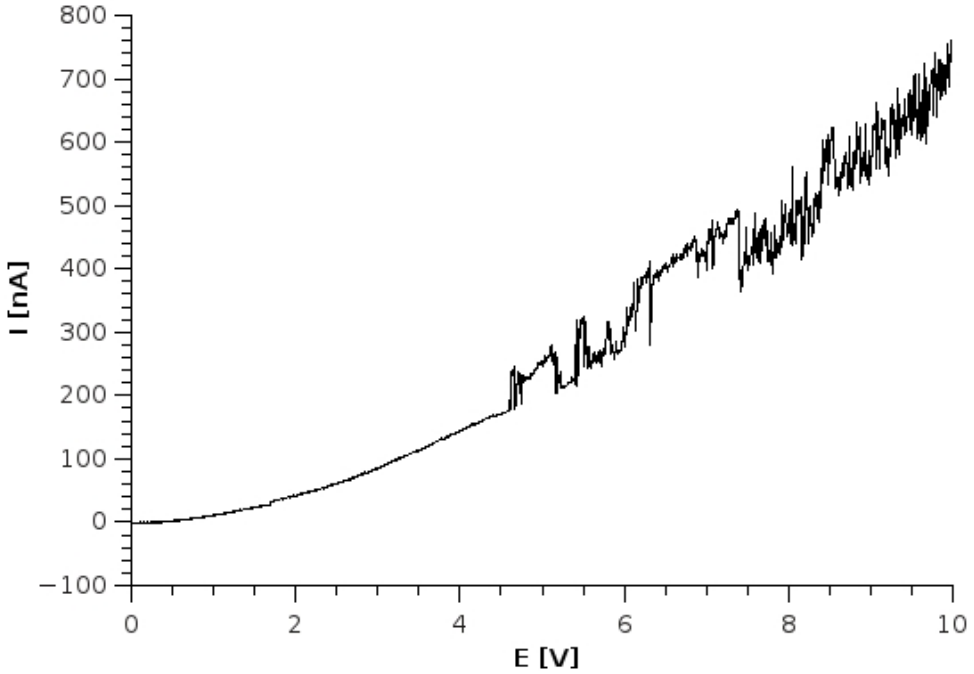

Figure 6.17: Electrical conductivity of a pure P3HT film

and is plotted in figure 6.17.

Then sample with a layer of deposited nanotubes and with a drop cast P3HT film on top is measured. The resulting curve is traced in figure 6.18.

The conductivity is reduced compared to the pure P3HT sample: the nanotubes deposited at the top of the silicon substrate prior to the deposition of the P3HT might act as a buffer reducing the conductivity of the sample. This could also be due to difference in film thickness between the two samples. However, they have been processed in the same way and by using the same solution, therefore the difference in thickness between the samples is expected to be quite low. Another dual layer sample with CNTs deposited on silicon substrate and P3HT drop cast on top is thermally imprinted with the same conditions as before (170℃, 50 bar, 600 seconds) and its electrical conductivity is measured. The resulting graph is shown in figure 6.19.

The electrical conductivity of the sample seems to have decreased. This can be due to the reduced contact area between the electrode and the patterned area of the sample, compared to the greater contact area between the electrode and the comparatively smoother surface area of the non imprinted sample. Indeed, the contact area of the patterned area is divided by 4 compared to the non patterned contact area. As the total weight of the electrode is quite low (around 24 g), the PDMS electrode is not expected to be too much deformed, therefore the contact between the electrode and the patterned sample is presumed to be at the top of the pillars. Assuming that the measured conductivity is proportional to the contact area, the measured current should be divided by at least 4 if there was no effect from the NIL process on the nanotubes disposion. However, this is not the case here, meaning that the imprint process can have had an effect on the nanotubes

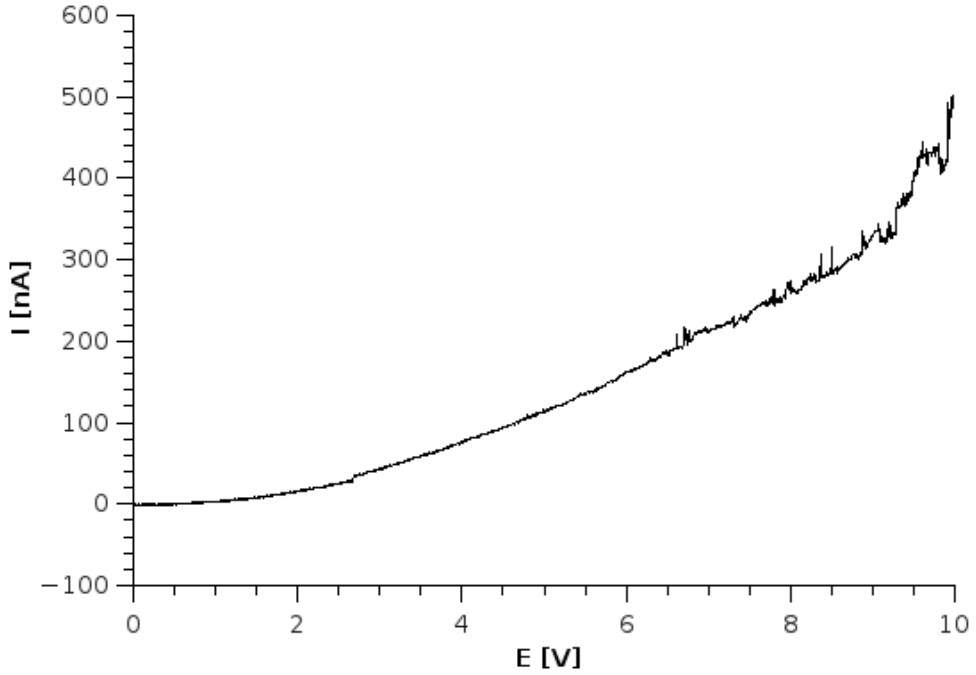

Figure 6.18: Electrical conductivity of a dual layer P3HT/CNTs sample

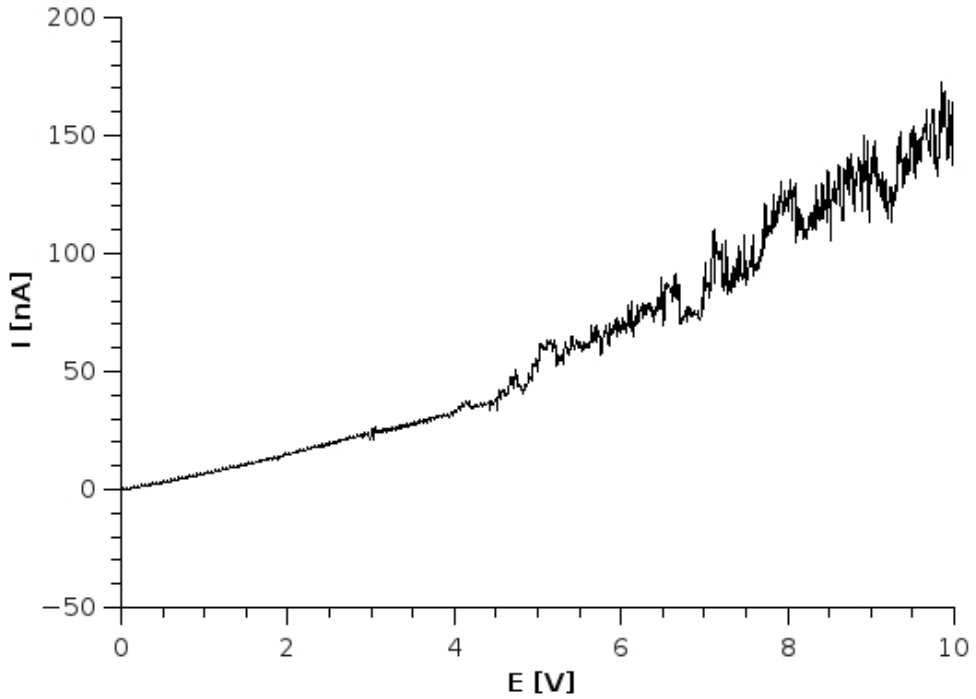

Figure 6.19: Electrical conductivity of an imprinted dual layer P3HT/CNTs sample

resulting in a slight improvement of the electrical conductivity of the sample compared to what was expected if there was no effect at all from the NIL on the nanotubes.
The fact that the measured current remains low also shows that the nanotubes are not able to make a contact between the bottom layer and the top area of the sample. This can be due to the too high thickness of the film as well as to the insufficient length of the nanotubes. Indeed, both dual layer samples which have been measured in this experiment have been made in the same fashion as the one analyzed in SEM and XPS. They are therefore expected to have a similar thickness of about 18 μm. This makes difficult for the nanotubes to create a direct path between the silicon substrate and the top surface of the sample, as their volumic concentration might be quite low.

6.5 Substrate rubbing

A piece of PTFE has been cut and imprinted on smooth silicon at 250°C and a pressure of 30 bar for 300 seconds. The PTFE slide has then been rubbed on a silicon piece heated at around 200°C. CNTs dispersed in o-DCB have then been deposited and Raman spectroscopy measurements have been done. In order to detect possible alignment of the CNTs, different measurements at the same spot for different orientations of the sample have been done. However, all the resulting spectra are identical, which indicates that no specific orientation of the CNTs is detected. This might be due to the fact that the layer of deposited nanotubes is too thick for a supposed alignment at the surface of the piece of PTFE to propagate up to the surface of the nanotubes layer. Therefore, two PTFE slides are prepared in the same fashion and CNTs are deposited on top of one prepared piece of PTFE. Before the film containing the nanotubes dispersion has time to dry, the second piece of PTFE is placed on top of it, sandwiching the nanotubes between the two slices. The PTFE pieces are placed in such a way that the rubbing directions match each other. When the nanotubes dispersion has dried, Raman spectroscopy is achieved on both samples. However, it seems that most of the nanotubes have been removed from the sample when the second piece of PTFE has been placed on top of the first one. Therefore, the signal coming from the nanotubes is localised to very few spots on the samples and is too weak to be usable to determine their orientation.
In order to be able to determine the nanotubes alignment on the PTFE slides, either a way to deposit an extremely thin layer of nanotubes all over the PTFE surface has to be found, or high resolution TEM can be used to track down the remaining individual nanotubes deposited on the PTFE slide and determine their position and orientation compared to the PTFE fibers, making possible to see if the PTFE fibers have helped to orient the deposited nanotubes in some way.

Chapter 7

Conclusion and recommendations

It has been shown that nanoimprint lithography can be considered as a way to influence the dispersion of nanotubes in a polymer film. Indeed, the three main methods used to characterize nanoimprinted samples in this project seems to confirm the fact that nanotubes are displaced during the imprint process. The Raman mapping shown in figure 6.12 on page 56 combined with the SEM pictures in figure 6.14 on page 58 clearly show that the nanotubes have been moved along the imprinted patterns. The differences between the SEM pictures in figure 6.10 on page 53 and figure 6.14 on page 58 shows that the dual layer configuration used in the project is more appropriate to easily determine the distribution of the nanotubes in the polymer film.

However, more verifications are needed in order to conclude categorically on the ability of NIL to even roughly align the nanotubes in polymer films. Transmission electron microscopy should be used to be able to see individual nanotubes and therefore assess their orientation. Also, thickness of the polymer film in the bi-layer configuration should be optimized in order to obtain better results. Thinner films would be more appropriate as they would be closer to actual films used in solar cells.

The electric-field assisted self-assembly process has been tried on a PS/CNTs dual layer sample. The electrical conductivity measurements done are shown in figure 6.16 on page 61. An increase in electrical conductivity is detected, which could indicate an effect from the nanotubes. However, the measured current is extremely small, in the order of a few nano amperes, which could also be due to impurities in the film. Also, the film is expected to be quite thick, which could prevent the nanotubes to form a conducting path from the silicon substrate to the surface of the sample. More experiments with thinner films should be done. Finally, the electric field used was stationary. Experiments involving alternating fields with different frequencies should also be done in order to determine the optimal parameters for nanotubes alignment in polymer film using electric-field assisted self-assembly.

Finally, the substrate rubbing experiment didn't produce any usable result. However, this type of experiment was just a side-project and has not been really fully developed. The alignment of the PTFE chains at the surface of the sample should be checked with AFM, a process which can prove to be complicated. A sharp tip should be used, and optimal imaging parameters have to be found in order to obtain a usable picture. Moreover, several nanotubes deposition methods should be tried, in order to have nanotubes depositions of different thicknesses in order to find the optimal thickness for a hypothetical

alignment of the nanotubes along the PTFE chains.

Appendices

Appendix A

Energy band of carbon nanotubes

The determination of the energy band structure of SWNTs is exposed in details in the book from Saito *et al* [1998]. The different parameters used in the calculations are defined in table A.1. The π and π^* band of graphene are first determined as

$$E_{g2D}\left(k_x, k_y\right) = \pm t\sqrt{1 + 4\cos\frac{\sqrt{3}k_x a}{2}\cos\frac{k_y a}{2} + 4\cos^2\frac{k_y a}{2}} \tag{A.1}$$

where k_x and k_y are the coordinates of the wavevector $\vec{k}$, and t is the transfer integral calculated with the atomic wavefunctions and the Hamiltonian of graphene.
The π and π^* bands of graphene calculated according to equation A.1 are shown in figure A.1
By using rotational and translational symmetries due to the construction mechanism of the SWNTs, the energy band structure of the different types of SWNTs can be determined based on the one from graphene. Still according to Saito *et al*, the one dimensional energy dispersion relation for armchair nanotubes (type (n, n)) is

$$E_q^a\left(k\right) = \pm t\sqrt{1 + 4\cos\frac{q\pi}{n}\cos\frac{ka}{2} + 4\cos^2\frac{ka}{2}} \tag{A.2}$$

with $-\pi \leq ka \leq \pi$ and $q = 1, \ldots, 2n$. This relation is plotted in figure A.2a for a $(5, 5)$ SWNT.
The one dimensional energy dispersion relation for zigzag nanotubes (type $(n, 0)$) is

$$E_q^z\left(k\right) = \pm t\sqrt{1 + 4\cos\frac{\sqrt{3}ka}{2}\cos\frac{q\pi}{n} + 4\cos^2\frac{q\pi}{n}} \tag{A.3}$$

with $-\frac{\pi}{\sqrt{3}} \leq ka \leq \frac{\pi}{\sqrt{3}}$ and $q = 1, \ldots, n$. This relation is plotted in figure A.2b for a $(9, 0)$ SWNT and in figure A.2c for a $(10, 0)$ SWNT.
Finally, the one dimensional energy relation for chiral nanotubes (type (n, m)) is

$$E_\mu\left(k\right) = E_{g2D}\left(k\frac{\vec{K_2}}{|\vec{K_2}|} + \mu\vec{K_1}\right) \tag{A.4}$$

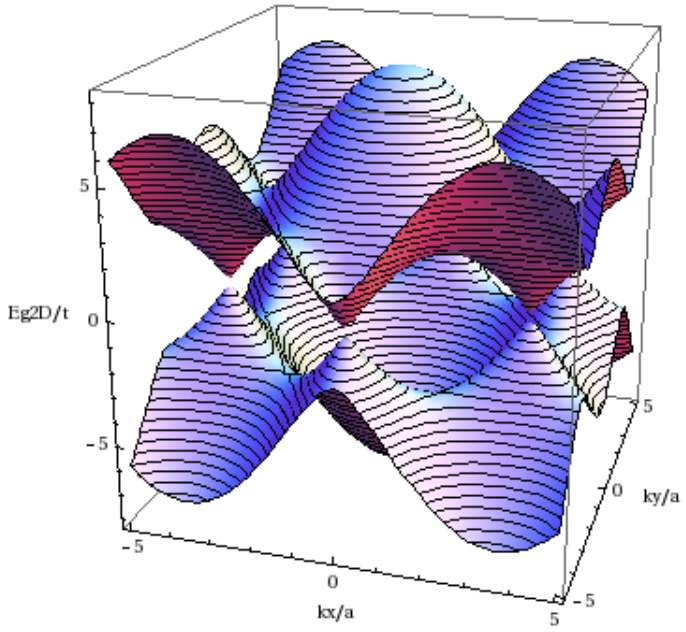

Figure A.1: π and π^* band of graphene

with $-\frac{2\pi}{3T} \leq k \leq \frac{2\pi}{3T}$, $\mu = 0, \ldots, N-1$ and with $\vec{K_1}$ and $\vec{K_2}$ defined as

$$\begin{cases} \vec{K_1} = \frac{1}{N}\left(-t_2\vec{b_1} + t_1\vec{b_2}\right) \\ \vec{K_2} = \frac{1}{N}\left(m\vec{b_1} - n\vec{b_2}\right) \end{cases} \tag{A.5}$$

The one dimensional energy band structure of a $(6,5)$ SWNT is plotted in figure A.2d.

symbol	**name**	**value/formula**
a_{c-c}	carbon-carbon distance	1.42 Å
a	length of unit vector	$a = \sqrt{3}a_{c-c}$
$\vec{b_1}$,$\vec{b_2}$	reciprocal lattice vectors	$\frac{2\pi}{a}\left(\frac{1}{\sqrt{3}}, 1\right)$, $\frac{2\pi}{a}\left(\frac{1}{\sqrt{3}}, -1\right)$
d_R	$\gcd(2n+m, 2m+n)$	
N	Number of hexagons in the nanotube unit cell	$N = \frac{2\left(n^2+m^2+nm\right)}{d_R}$

Table A.1: Parameters used in the enrgy band structure calculation

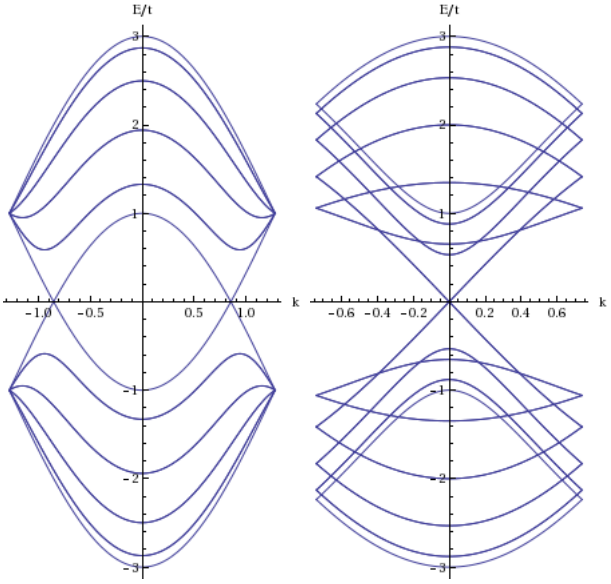

(a) $(5, 5)$ SWNT (b) $(9, 0)$ SWNT

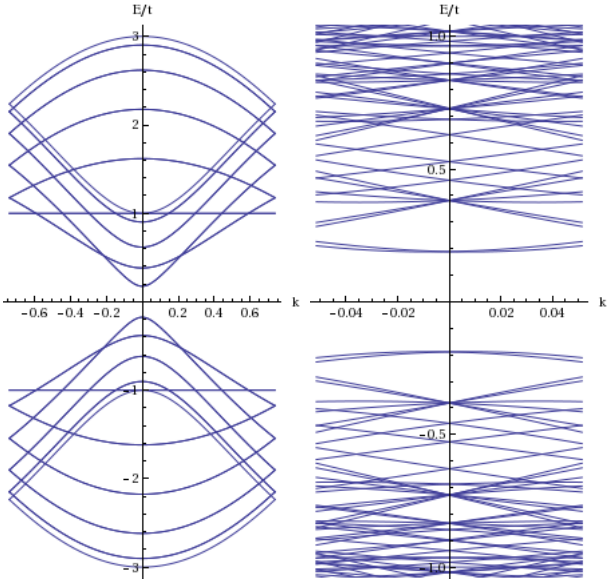

(c) $(10, 0)$ SWNT (d) $(6, 5)$ SWNT

Figure A.2: Energy band structure of several types of SWNTs.

Appendix B

Mathematica code for the electronic band structure determination of single-walled carbon nanotubes

The Mathematica code used in the project for determining the electronic band structure of SWNTs is based on the equations presented in appendix A.

```
1  (* For graphene *)
2  acc = 1.42;
3  a := Sqrt[3]*acc;
4  t := 2.7;
5  Eg2D[k_] := t*Sqrt[1 + 4*Cos[Sqrt[3]*k[[1]]*a/2]*Cos[k[[2]]*a/2]
       + 4*Cos[k[[2]]*a/2]^2];
6
7  (* For SWNT *)
8  b1 := {1/Sqrt[3], 1}*2*Pi/a;
9  b2 := {1/Sqrt[3], -1}*2*Pi/a
10 dR[n_, m_] := GCD[2*n + m, 2*m + n];
11 t1[n_, m_] := (2*m + n)/dR[n, m];
12 t2[n_, m_] := -(2*n + m)/dR[n, m];
13 Enne[n_, m_] := 2*(n^2 + m^2 + m*n)/dR[n, m];
14 K1[n_, m_] := 1/Enne[n, m]*(-t2[n, m]*b1 + t1[n, m]*b2);
15 K2[n_, m_] := 1/Enne[n, m]*(m*b1 - n*b2);
16 L[n_, m_] := a*Sqrt[n^2 + m^2 + n*m];
17 T[n_, m_] := Sqrt[3]*L[n, m]/dR[n, m];
18
19 (* Armchair nanotube (n,n) *)
20
21 Earm[k_, n_, q_] := t*Sqrt[1 + 4*Cos[q*Pi/n]*Cos[k*a/2] + 4*Cos[
       k*a/2]^2]
22 supArm[n_] := Table[Plot[Earm[k, n, q]/t, {k, -Pi/a, Pi/a}], {q,
       1, 2*n}]
23 totArm[n_] := Append[supArm[n], Table[Plot[-Earm[k, n, q]/t, {k,
       -Pi/a, Pi/a}], {q, 1, 2*n}]]
```

```
24 CuArm[n_] := Show[totArm[n], PlotRange -> Automatic, AspectRatio
       -> 2, AxesLabel -> {"k", "E/t"}, Axes -> True, AxesOrigin ->
       {0, 0}];
25
26 (* Zigzag nanotube (n,0) *)
27
28 Ezig[k_, n_, q_] := t*Sqrt[1 + 4*Cos[Sqrt[3]*k*a/2]*Cos[q*Pi/n]
      + 4*Cos[q*Pi/n]^2]
29 supZig[n_] := Table[Plot[Ezig[k, n, q]/t, {k, -Pi/(Sqrt[3]*a),
      Pi/(Sqrt[3]*a)}], {q, 1, 2*n}]
30 totZig[n_] := Append[supZig[n], Table[Plot[-Ezig[k, n, q]/t, {k,
      -Pi/(Sqrt[3]*a), Pi/(Sqrt[3]*a)}], {q, 1, 2*n}]]
31 CuZig[n_] := Show[totZig[n], PlotRange -> Automatic, AspectRatio
       -> 2, AxesLabel -> {"k", "E/t"}, Axes -> True, AxesOrigin ->
       {0, 0}];
32
33 (* Chiral nanotube (n,m) *)
34
35 Echi[k_, mu_, n_, m_] := Eg2D[k*K2[n, m]/Norm[K2[n, m]] + mu*K1[
      n, m]]
36 supChi[n_, m_] := Table[Plot[Echi[k, mu, n, m]/t, {k, -2*Pi/(3*T
      [n, m]), 2*Pi/(3*T[n, m])}], {mu, 0, Enne[n, m] - 1}]
37 totChi[n_, m_] := Append[supChi[n, m], Table[Plot[-Echi[k, mu, n
      , m]/t, {k, -2*Pi/(3*T[n, m]), 2*Pi/(3*T[n, m])}], {mu, 0,
      Enne[n, m] - 1}]]
38 CuChi[n_, m_] := Show[totChi[n, m], PlotRange -> {{-2*Pi/(3*T[n,
       m]), 2*Pi/(3*T[n, m])}, {-1, 1}}, AspectRatio -> 2,
      AxesLabel -> {"k", "E/t"}, Axes -> True, AxesOrigin -> {0,
      0}];
```

Appendix C

SWNTs Certificate of Analysis

Certificate of Analysis

SIGMA-ALDRICH

Product Name	Carbon nanotube, single-walled, (6,5) chirality, carbon >90 %, ≥77% (carbon as SWCNT), 0.7-0.9 nm diameter (by fluorescence)
Product Number	704148
Product Brand	ALDRICH
CAS Number	308068-56-6

TEST	SPECIFICATION	LOT MKBD4116V RESULTS
Purity	≥77.0 % T1% (Estimate of SWNT Content by Weight (TGA))	78.0 %
Residual Mass	≤10.0 % (TGA)	7.7 %
Carbon	≥90.0 % (TGA)	92.3 %
Chirality Distribution	≥1.8 P2B (QC Parameter for control of chirality distribution at 979 to 985 nm (UV-vis-NIR Spectroscopy))	3.4
Quality Factor	≥0.940 Q (D:G Ratio)Raman Spectroscopy	0.941
Note	Conforms Please see Technical Bulletin AL-252 for explanation of quality parameters. Spectra available upon request.	Conforms
Specification Date:		JUN 2010
Date of QC Release:		APR 2010
Print Date:		AUG 18 2010

Barbara Rajzer, Supervisor
Quality Control
Milwaukee, Wisconsin USA

Appendix D

P3HT Certificate of Analysis

American Dye Source, Inc.
555 Morgan Blvd.,
Baie d'Urfé, Quebec, Canada, H9X 3T6
Tel: (514) 457-0070 • Fax: (514) 457-0071
E-mail: info@adsdyes.com

Colorants de Source American, Inc.
555 boul. Morgan,
Baie d'Urfé, Québec, Canada, H9X 3T6
Tél: (514) 457-0070 • Fax: (514) 457-0071
Courriel: info@adsdyes.com

CERTIFICATE OF ANALYSIS

Product: Polythiophene Derivative ADS306PT

Chemical Name: Poly(3-hexylthiophene-2,5-diyl), Regio-regular

Chemical Structure:

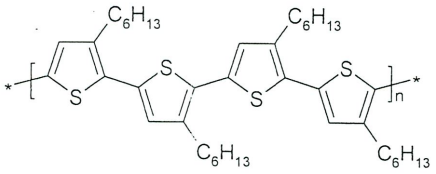

CAS #: N/A

Lot #: 10K046A

Date: December 06th, 2010

Analysis

Appearance:	Brown Fibers
Volatile Moisture Balance (TGA):	< 1%
Molecular Weight (GPC):	43 000 (PS Standards)
Polydispersity:	1.8
UV-Vis (λ_{max} Absorption) :	449 nm (THF)
Photoluminescence (λ_{max} Emission):	564 nm (THF)
Metal Content (AA analysis) :	
Ni :	< 59 ppm

Authorized Signature:

References

Alexandrou, I., Lioudakis, E., Delaportas, D., Zhao, C. Z., and Othonos, A. (2009). Monitoring charge exchange in P3HT-Nanotube composites using optical and electrical characterisation. *Nanoscale Research Letters*, 4(7):635–639.

Aryal, M., Trivedi, K., and Hu, W. (2009). Nano-Confinement induced chain alignment in ordered P3HT nanostructures defined by nanoimprint lithography. *Acs Nano*, 3(10):30853090.

Azar, C., Lindgren, K., Larson, E., and Mllersten, K. (2006). Carbon capture and storage from fossil fuels and biomass costs and potential role in stabilizing the atmosphere. *Climatic Change*, 74(1-3):47–79.

Barbero, D. R., Saifullah, M. S. M., Hoffmann, P., Mathieu, H. J., Anderson, D., Jones, G. A. C., Welland, M. E., and Steiner, U. (2007). High resolution nanoimprinting with a robust and reusable polymer mold. *Advanced Functional Materials*, 17(14):2419–2425.

Barnes, T. M., Bergeson, J. D., Tenent, R. C., Larsen, B. A., Teeter, G., Jones, K. M., Blackburn, J. L., and van de Lagemaat, J. (2010). Carbon nanotube network electrodes enabling efficient organic solar cells without a hole transport layer. *Applied Physics Letters*, 96(24).

Barros, C. P. and Peypoch, N. (2007). The determinants of cost efficiency of hydroelectric generating plants: A random frontier approach. *Energy Policy*, 35(9):4463–4470.

Bethune, D. S., Klang, C. H., de Vries, M. S., Gorman, G., Savoy, R., Vazquez, J., and Beyers, R. (1993). Cobalt-catalysed growth of carbon nanotubes with single-atomic-layer walls. *Nature*, 363(6430):605–607.

Blengini, G. and Carlo, T. D. (2010). Energy-saving policies and low-energy residential buildings: an LCA case study to support decision makers in piedmont (Italy). *INTERNATIONAL JOURNAL OF LIFE CYCLE ASSESSMENT*, 15(7):652–665.

Bogner, A., Jouneau, P., Thollet, G., Basset, D., and Gauthier, C. (2007). A history of scanning electron microscopy developments: Towards "wet-stem" imaging. *Micron*, 38(4):390–401.

Brabec, C. J., Sariciftci, N. S., and Hummelen, J. C. (2001). Plastic solar cells. *Advanced Functional Materials*, 11(1):15–26.

Bundgaard, E. and Krebs, F. (2007). Low band gap polymers for organic photovoltaics. *Solar Energy Materials and Solar Cells*, 91(11):954–985.

Caruso, M. M., Davis, D. A., Shen, Q., Odom, S. A., Sottos, N. R., White, S. R., and Moore, J. S. (2009). Mechanically-Induced chemical changes in polymeric materials. *Chemical Reviews*, 109(11):5755–5798.

Celia, M., Nordbotten, J., Court, B., Dobossy, M., and Bachu, S. (2011). Field-scale application of a semi-analytical model for estimation cif CO_2 and brine leakage along old wells. *International Journal of Greenhouse Gas Control*, 5(2):257–269.

Chalmers, H. and Gibbins, J. (2010). Carbon capture and storage: the ten year challenge. *PROCEEDINGS OF THE INSTITUTION OF MECHANICAL ENGINEERS PART C-JOURNAL*, 224(C3):505–518.

Chapelle, M. L. D. L., Lefrant, S., Journet, C., Maser, W., Bernier, P., and Loiseau, A. (1998). Raman studies on single walled carbon nanotubes produced by the electric arc technique. *Carbon*, 36(5-6):705–708.

Chaudhary, S., Lu, H., Müller, A. M., Bardeen, C. J., and Ozkan, M. (2007). Hierarchical placement and associated optoelectronic impact of carbon nanotubes in Polymer-Fullerene solar cells. *Nano Letters*, 7(7):1973–1979.

Cheng, Q., Debnath, S., Gregan, E., and Byrne, H. J. (2010). Ultrasound-Assisted SWNTs dispersion: Effects of sonication parameters and solvent properties. *The Journal of Physical Chemistry C*, 114(19):8821–8827.

Cho, K. S., Mandal, P., Kim, K., Baek, I. H., Lee, S., Lim, H., Cho, D. J., Kim, S., Lee, J., and Rotermund, F. (2011). Improved efficiency in GaAs solar cells by 1D and 2D nanopatterns fabricated by laser interference lithography. *Optics Communications*, 284(10-11):2608–2612.

Collins, P. G. and Avouris, P. (2000). Nanotubes for electronics. *Scientific American*, 283(6):6269.

Defaux, M., Vidal, L., Möller, M., Gearba, R. I., DiMasi, E., and Ivanov, D. A. (2009). Thin films of a Main-Chain columnar liquid crystal: Studies of structure, phase transitions, and alignment. *Macromolecules*, 42(10):3500–3509.

Dissanayake, N. M. and Zhong, Z. (2011). Unexpected hole transfer leads to high efficiency Single-Walled carbon nanotube hybrid photovoltaic. *Nano Letters*, 11(1):286–290.

Dresselhaus, M. S., Dresselhaus, G., and Saito, R. (1995). Physics of carbon nanotubes. *Carbon*, 33(7):883–891.

Dumortier, H., Lacotte, S., Pastorin, G., Marega, R., Wu, W., Bonifazi, D., Briand, J., Prato, M., Muller, S., and Bianco, A. (2006). Functionalized carbon nanotubes are Non-Cytotoxic and preserve the functionality of primary immune cells. *Nano Letters*, 6(7):1522–1528.

Ebbesen, T. W. and Ajayan, P. M. (1992). Large-scale synthesis of carbon nanotubes. *Nature*, 358(6383):220–222.

Einstein, A. (1905). Über einen die erzeugung und verwandlung des lichtes betreffenden heuristischen gesichtspunkt. *Annalen der Physik*, 322(6):132–148.

French, D. (1998). Kyoto protocol to the united nations framework convention on climate change. *Journal of Environmental Law*, 10(1):215 –224.

Gardette, J., Rivaton, A., Thrias, S., Chambon, S., Manceau, M., and Gaume, J. (2010). Predicting the ageing and the long-term durability of organic polymer solar cells. In *Vth International Conference on Times of Polymers (TOP) and Composites*, volume 1255. AIP Conference Proceedings.

Geng, J., Kong, B., Yang, S. B., Youn, S. C., Park, S., Joo, T., and Jung, H. (2008). Effect of SWNT defects on the electron transfer properties in P3HT/SWNT hybrid materials. *Advanced Functional Materials*, 18(18):2659–2665.

Graus, W., Roglieri, M., Jaworski, P., Alberio, L., and Worrell, E. (2011). The promise of carbon capture and storage: evaluating the capture-readiness of new EU fossil fuel power plants. *Climate Policy*, 11(1):789–812.

Guo, T., Nikolaev, P., Rinzler, A. G., Tomnek, D., Colbert, D. T., and Smalley, R. E. (1995a). Self-assembly of tubular fullerenes. *The Journal of Physical Chemistry*, 99(27):1069410697.

Guo, T., Nikolaev, P., Thess, A., Colbert, D. T., and Smalley, R. E. (1995b). Catalytic growth of single-walled manotubes by laser vaporization. *Chemical Physics Letters*, 243(1-2):4954.

Haggenmueller, R., Gommans, H., Rinzler, A., Fischer, J., and Winey, K. (2000). Aligned single-wall carbon nanotubes in composites by melt processing methods. *Chemical Physics Letters*, 330(3-4):219–225.

Heise, H. M., Kuckuk, R., Ojha, A. K., Srivastava, A., Srivastava, V., and Asthana, B. P. (2009). Characterisation of carbonaceous materials using raman spectroscopy: a comparison of carbon nanotube filters, single and multiwalled nanotubes, graphitised porous carbon and graphite. *Journal of Raman Spectroscopy*, 40(3):344–353.

Helland, A., Wick, P., Koehler, A., Schmid, K., and Som, C. (2007). Reviewing the environmental and human health knowledge base of carbon nanotubes. *Environmental Health Perspectives*, 115(8):1125–1131.

Heyderman, L. J., Schift, H., David, C., Gobrecht, J., and Schweizer, T. (2000). Flow behaviour of thin polymer films used for hot embossing lithography. *Microelectronic Engineering*, 54(3-4):229–245.

Hoppe, H. and Sariciftci, N. (2008). Polymer solar cells. *Photoresponsive Polymers II*, 214:1–86.

Hoth, C. N., Schilinsky, P., Choulis, S. A., and Brabec, C. J. (2008). Printing highly efficient organic solar cells. *Nano Letters*, 8(9):2806–2813.

IEA (2010a). Key world energy statistics 2010.

IEA (2010b). World energy outlook 2010.

Iijima, S. (1991). Helical microtubules of graphitic carbon. *Nature*, 354(6348):56–58.

Iijima, S. and Ichihashi, T. (1993). Single-shell carbon nanotubes of 1-nm diameter. *Nature*, 363(6430):603–605.

Jørgensen, M., Norrman, K., and Krebs, F. C. (2008). Stability/degradation of polymer solar cells. *Solar Energy Materials and Solar Cells*, 92(7):686–714.

José-Yacamán, M., Miki-Yoshida, M., Rendon, L., and Santiesteban, J. G. (1993). Catalytic growth of carbon microtubules with fullerene structure. *Applied physics letters*, 62(2):202204.

Jozef, D. (2009). Geological and geophysical aspects of the underground CO_2 storage. *PROCEEDINGS OF THE INTERNATIONAL CONFERENCE ON MINING SCIENCE &*, 1(1):7–12.

Kaldellis, J. and Zafirakis, D. (2011). The wind energy (r)evolution: A short review of a long history. *RENEWABLE ENERGY*, 36(7):1887–1901.

Keresztury, G. (2006). Raman spectroscopy: Theory. In Chalmers, J. M., Griffiths, P. R., and Chalmers, J. M., editors, *Handbook of Vibrational Spectroscopy*. John Wiley & Sons, Ltd, Chichester, UK.

Kessides, I. N. (2010). Nuclear power and sustainable energy policy: Promises and perils. *The World Bank Research Observer*, 25(2):323 –362.

Kong, S. M., Xiao, Y., Kim, K. H., In Lee, W., and Chung, C. W. (2011). Performance improvement of dye-sensitized solar cells by surface patterning of fluorine-doped tin oxide transparent electrodes. *Thin Solid Films*, 519(10):3173–3176.

Koster, L., Smits, E., Mihailetchi, V., and Blom, P. (2005). Device model for the operation of polymer/fullerene bulk heterojunction solar cells. *Physical Review B*, 72(8).

Koster, L. J. A., Mihailetchi, V. D., and Blom, P. W. M. (2006). Ultimate efficiency of polymer/fullerene bulk heterojunction solar cells. *Applied Physics Letters*, 88(9):093511.

Kymakis, E. and Amaratunga, G. A. J. (2006). Electrical properties of single-wall carbon nanotube-polymer composite films. *Journal of Applied Physics*, 99(8):084302.

Lenzen, M. (2010). Current state of development of Electricity-Generating technologies: A literature review. *ENERGIES*, 3(3):462–591.

Leolukman, M. and Kim, S. H. (2005). Effect of Rubbing-Induced polymer chain alignment on adhesion and friction of glassy polystyrene surfaces. *Langmuir*, 21(2):682–685.

Lolli, G., Zhang, L., Balzano, L., Sakulchaicharoen, N., Tan, Y., and Resasco, D. E. (2006). Tailoring (n,m) structure of Single-Walled carbon nanotubes by modifying reaction conditions and the nature of the support of CoMo catalysts. *The Journal of Physical Chemistry B*, 110(5):2108–2115.

Lu, K. (1996). Mechanical damage of carbon nanotubes by ultrasound. *Carbon*, 34(6):814–816.

Lu, X. and Chen, Z. (2005). Curved Pi-Conjugation, aromaticity, and the related chemistry of small fullerenes. *Chemical Reviews*, 105(10):3643–3696.

Maeda, Y., Sagara, A., Hashimoto, M., Hirashima, Y., Sode, K., Hasegawa, T., Kanda, M., Ishitsuka, M. O., Tsuchiya, T., Akasaka, T., Okazaki, T., Kataura, H., Lu, J., Nagase, S., and Takeuchi, S. (2009). Tuning of electronic properties of Single-Walled carbon nanotubes under homogenous conditions. *ChemPhysChem*, 10(6):926–930.

Manceau, M., Chambon, S., Rivaton, A., Gardette, J., Guillerez, S., and Lematre, N. (2010). Effects of long-term UVvisible light irradiation in the absence of oxygen on P3HT and P3HT:PCBM blend. *Solar Energy Materials and Solar Cells*, 94(10):1572–1577.

Marc A, R. (2001). Energy- and exergy-based comparison of coal-fired and nuclear steam power plants. *Exergy, An International Journal*, 1(3):180–192.

Markandya, A., Ortiz, R., Mudgal, S., and Tinetti, B. (2009). Analysis of tax incentives for energy-efficient durables in the EU. *ENERGY POLICY*, 37(12):5662–5674.

Mihailetchi, V., Koster, L., Hummelen, J., and Blom, P. (2004). Photocurrent generation in Polymer-Fullerene bulk heterojunctions. *Physical Review Letters*, 93(21):216601.

Mlecnik, E. (2010). Adoption of highly energy-efficient renovation concepts. *OPEN HOUSE INTERNATIONAL*, 35(2):39–48.

Monthioux, M. and Kuznetsov, V. L. (2006). Who should be given the credit for the discovery of carbon nanotubes? *Carbon*, 44(9):1621–1623.

Nicholson, P. G. and Castro, F. A. (2010). Organic photovoltaics: principles and techniques for nanometre scale characterization. *Nanotechnology*, 21:492001.

Noorman, S., Gallucci, F., Annaland, M., and Kuipers, J. (2011). Experimental investigation of Chemical-Looping combustion in packed beds: A parametric study. *INDUSTRIAL & ENGINEERING CHEMISTRY RESEARCH*, 50(4):1968–1980.

Patil, R., Colls, J., and Steven, M. (2010). Effects of CO_2 gas as leaks from geological storage sites on agro-ecosystems. *ENERGY*, 35(12):4587–4591.

Pensack, R. D., Banyas, K. M., and Asbury, J. B. (2010). Vibrational solvatochromism in organic photovoltaic materials: method to distinguish molecules at donor/acceptor interfaces. *Physical Chemistry Chemical Physics*, 12:14144.

Petrova-Koch, V. (2009). Milestones of solar conversion and photovoltaics. In Petrova-Koch, V., Hezel, R., and Goetzberger, A., editors, *High-Efficient Low-Cost Photovoltaics*, volume 140, pages 1–5. Springer Berlin Heidelberg, Berlin, Heidelberg.

Raman, C. V. and Krishnan, K. S. (1928). A new type of secondary radiation. *Nature*, 121(3048):501–502.

Ramana, M. (2009). Nuclear power: Economic, safety, health, and environmental issues of Near-Term technologies. *ANNUAL REVIEW OF ENVIRONMENT AND RESOURCES*, 34:127–152.

Ranney, T. A. and Parker, L. V. (1997). Comparison of fiberglass and other polymeric well casings, part i: Susceptibility to degradation by chemicals. *Ground Water Monitoring & Remediation*, 17(1):97–103.

Ratner, B. D. and Castner, D. G. (2009). *Electron Spectroscopy for Chemical Analysis*, pages 47–112. John Wiley & Sons, Ltd.

Rau, G. H. (2011). CO_2 mitigation via capture and chemical conversion in seawater. *Environmental Science & Technology*, 45(3):1088–1092.

Rieger, J. (1996). The glass transition temperature of polystyrene. *Journal of Thermal Analysis*, 46:965–972.

Rockett, A. (2007). Photovoltaics materials and devices. *AIP Conference Proceedings*, 960(1):161–202.

Saito, R. (1998). *Physical properties of carbon nanotubes*. Imperial College Press, London.

Schäffer, E., Thurn-Albrecht, T., Russell, T. P., and Steiner, U. (2000). Electrically induced structure formation and pattern transfer. *Nature*, 403:874–877.

Schäffer, E., Thurn-Albrecht, T., Russell, T. P., and Steiner, U. (2001). Electrohydrodynamic instabilities in polymer films. *Europhysics Letters (EPL)*, 53(4):518–524.

Schilinsky, P. (2004). Simulation of light intensity dependent current characteristics of polymer solar cells. *Journal of Applied Physics*, 95(5):2816.

Schilinsky, P., Waldauf, C., and Brabec, C. J. (2002). Recombination and loss analysis in polythiophene based bulk heterojunction photodetectors. *Applied Physics Letters*, 81(20):3885.

Schmid, J., Grob, B., Niessner, R., and Ivleva, N. P. (2011). Multiwavelength raman microspectroscopy for rapid prediction of soot oxidation reactivity. *Analytical Chemistry*, 83(4):1173–1179.

Siegbahn, K. (1982). Electron spectroscopy for atoms, molecules, and condensed matter. *Reviews of Modern Physics*, 54(3):709728.

Stöhr, J., Samant, M. G., Cossy-Favre, A., Diaz, J., Momoi, Y., Odahara, S., and Nagata, T. (1998). Microscopic origin of liquid crystal alignment on rubbed polymer surfaces. *Macromolecules*, 31(6):1942–1946.

Stranks, S. D., Weisspfennig, C., Parkinson, P., Johnston, M. B., Herz, L. M., and Nicholas, R. J. (2011). Ultrafast charge separation at a PolymerSingle-Walled carbon nanotube molecular junction. *Nano Letters*, 11(1):66–72.

Tan, Y. and Resasco, D. E. (2005). Dispersion of Single-Walled carbon nanotubes of narrow diameter distribution. *The Journal of Physical Chemistry B*, 109(30):14454–14460.

Tuttle, R. and Becker, D. (2000). The chernobyl accident and its consequences: Update at the millennium. *SEMINARS IN NUCLEAR MEDICINE*, 30(2):133–140.

Ural, A., Li, Y., and Dai, H. (2002). Electric-field-aligned growth of single-walled carbon nanotubes on surfaces. *Applied Physics Letters*, 81(18):3464.

Voicu, N. E., Ludwigs, S., Crossland, E. J. W., Andrew, P., and Steiner, U. (2007). Solvent-Vapor-Assisted imprint lithography. *Advanced Materials*, 19(5):757–761.

Wittmann, J. C. and Smith, P. (1991). Highly oriented thin films of poly(tetrafluoroethylene) as a substrate for oriented growth of materials. *Nature*, 352(6334):414–417.

Yianoulis, P. and Giannouli, M. (2008). Thin solid films and nanomaterials for solar energy conversion and energy saving applications. *Journal of Nano Research*, 2:49–60.

Zhao, J. (2011). Microstructuring poly(3-hexylthiophene) thin films by solvent vapor imprinting for solar cell applications. Master's thesis, Umeå University.